THE DEVELOPMENT OF A PULSE DETONATION ENGINE SIMULATOR FACILITY

S.I. Jackson and J.E. Shepherd

Graduate Aeronautical Laboratories,
California Institute of Technology, Pasadena, CA 91125

GALCIT Report FM 2002.006

This work was carried out under P.O. No. 00-592 for
Advanced Projects Research, Inc. under AF contract F04611-99-C-0017.

December 16, 2002
(Revised August 18, 2003)

Abstract

A facility has been constructed to simulate the flow in a pulse detonation engine. This report describes the design, construction, initial test results, and analyses of the basic operation of the facility. The principle of operation is that of a blow down wind tunnel with a pressurized supply reservoir of air emptying through a test section into a low pressure receiver vessel. The flow is started abruptly by rupturing a diaphragm that separates the downstream end of the test section from the receiver vessel. Following a short transient period of a wave propagation, a quasi–steady flow is set up in the rectangular test section of 100×100 mm cross section. The quasi–steady operation lasts about 0.15 s. During this time, a typical operating condition results in a test section Mach number of about 0.7 and a velocity of 200 m/s. The pressure and temperature in the test section can be adjusted by varying the conditions in the supply reservoir. The current implementation uses room temperature air at pressures up to 6 bar in the supply reservoir.

Tests were carried out to determine the performance as a function of the pressures in the supply and receiver vessel. Measurements included pressure and temperature in the two vessels and pitot and static probe measurements of the test section flow. Flow visualization with a schlieren system was also carried out. The data were analyzed by using simple one-dimensional steady and unsteady gas dynamics. Some two-dimensional unsteady numerical simulations were also carried out to examine the influence of the diaphragm location on the flow starting process. A control-volume model has been developed to predict the variation of pressure with time in the supply and receiver vessels. This model and analyses of the tests indicates that choked flow results in a constant Mach number inside the test section. The duration of the choked flow regime and the conditions within the test section can be reliably estimated with this model.

Contents

List of Figures

List of Tables

Nomenclature

A	Cross–sectional area
A^*	Minimum cross–sectional area (throat) for streamlines
$A_{physical}$	Physical or measured area of a channel
$c\,(t)$	Sound speed of mixture
$c_{4,B}$	Sound speed in driver of blowdown wind tunnel
$c_{4,S}$	Sound speed in driver of shock tube
C_d	Discharge coefficient
$\dot{m}$	Mass flow rate
$\dot{m}^*$	Mass flow rate for choked flow
M_d	Mass of fluid in driver
M_t	Total mass of fluid in system
M_r	Mass of fluid in receiver
Ma	Mach number
$Ma_3(t)$	Mach number at the static wall gauge
$P_d\,(t)$	Pressure in driver section
$P_{0,d}$	Initial pressure in driver section
$P_5\,(t)$	Pressure measured at the pitot probe
$P_3\,(t)$	Pressure measured at the static wall gauge
$P_{3,B}$	Pressure in test section during steady operation of a blowdown wind tunnel
$P_{3,S}$	Pressure behind an expansion wave in shock tube
$P_{4,B}$	Pressure in driver of blowdown wind tunnel
$P_{4,S}$	Driver pressure in shock tube
R	Gas constant
t	Time
$T_d\,(t)$	Stagnation temperature in driver
$T_{0,d}$	Initial driver stagnation temperature
T_3	Test section temperature
T_t	Total temperature of the flow
ΔT_{23}	Temperature difference at design conditions
u_3	Velocity of flow behind an expansion fan
V_d	Driver volume
V_r	Receiver volume
$V_M\,(t)$	Velocity from Mach number calculation
γ	Ratio of specific heats in mixture
$\rho_d\,(t)$	Driver density
$\rho_3\,(t)$	Density at static wall gauge
τ	Characteristic time for blowdown

1 Introduction

Pulse detonation engines are based on a periodic cycle of filling a detonation tube with a fuel-air mixture, detonating the mixture, exhausting the combustion products into the atmosphere, and purging the high-temperature products with air. This cycle is repeated from 10 to 100 times per second depending on the specifics of the construction. In some designs, a mechanical valve at the entrance to the detonation tube is used to stop the air flow and provide a surface (usually termed a "thrust wall") that prevents the detonation products from flowing upstream into the inlet of the engine. In other designs, a simple flow restriction or "aerodynamic valve" is located at the entrance to the detonation tube. Some means for injecting fuel and mixing it with the air stream must be provided as well as a detonation initiation mechanism.

Air-breathing engines will have an inlet system that compresses the incoming air and feeds a plenum just upstream of the inlet to the detonation tube. When the valve is open and/or the pressure in the plenum is sufficiently high compared to the pressure in the detonation tube, there will be flow from the plenum into the tube. The fuel will have to be injected and mixed with this flow to create a detonable mixture. At the end of the injection period, the valve will be closed and the mixture detonated.

The present study is concerned with testing those aspects of the pulse detonation engine that are associated with mixing fuel into the air and initiating combustion. The approach is to construct a facility that can produce, for a short duration, flow speeds and pressures that are comparable to those expected in a flight system. Several approaches are possible to this problem and in fact, there are existing facilities at DoD and private laboratories that provide this capability by using compressors and heaters to obtain the desired flow conditions. However, these facilities are costly to operate and would be expensive to reproduce. Our approach is to develop a low-cost and simple-to-operate facility that is based on unsteady flow to achieve the desired flow rates for a relatively short period of time compared to steady test facilities, but long compared to a typical the pulse detonation engine cycle time. As a point of comparison, a steady-flow facility operating at the peak mass flow rate of 5 kg/s and a velocity of 200 m/s would require a compressor power of about 100 kW (130 hp) while an ordinary 5 hp air compressor is adequate to quickly pressurize the supply vessel of the blowdown facility.

The facility that was developed is a variation on the classical blow down wind tunnel in which a high-pressure reservoir or supply vessel is discharged through the test section into an initially low-pressure receiver vessel. The test section is optically accessible on two sides, 10 cm x 10 cm in cross–section, and 61 cm long. The pressure in the supply vessel is currently limited to 6 bar since that is the maximum pressure of the readily available compressed air source. Velocities in the test section up to 220 m/s have been achieved with the present setup. The flow is started by mechanically rupturing a thin plastic diaphragm downstream of the test section. There is an initial transient during which a shock propagates into the receiver vessel and an expansion travels through the test section accelerating the gas in the test section and receiver. Following this transient, the pressure difference between supply and receiver vessels establishes a quasi–steady

flow with a Mach number of about 0.7 in the test section for a period of 0.15 s. The testing is carried out in the first 10–20 ms of the quasi–steady period. The pressure in the driver vessel decreases and the pressure in the receiver vessel increases until the pressures equilibrate and the flow ceases.

The facility can be used to study combustion by injecting fuel, providing some time for mixing, and then igniting the mixture. The resulting combustion event is recorded by pressure transducers in the test section and visualized by the schlieren system. Although combustion tests were carried out as part of this project, the present report only describes the basic operation of creating the quasi-steady flow.

The report is organized as follows: Section 2 describes the preliminary design studies and numerical simulations of the starting process in the valve body. Section 3 describes the facility and test operation procedure. Section 4 gives the results of the testing with and without a valve body. Section 5 describes a simple model for operation without a valve body and comparisons to the test results. Section 6 summarizes this study. The raw data from the individual tests are given in the appendices.

2 Facility Development

2.1 Design: shock tube versus blowdown wind tunnel

The design goal for the facility was to produce an airflow of 200 m/s for 10–20 ms at a pressure of at least 80 kPa in the test section. Two different facility designs were considered: (i) a shock tube design and (ii) a blowdown wind tunnel design. Important considerations in development of our design were to make maximum use of existing facilities and to design the facility to fit into the current experimental area of the Explosion Dynamics Laboratory (see Appendix A for the available space). It was decided that the blowdown wind tunnel design best met the goals and requirements. The analysis supporting this decision is presented below.

2.1.1 Shock tube design

A shock tube is a channel initially divided into two parts by a diaphragm. The pressure on one side is higher than on the other side. The convention is to call the high-pressure section the driver and the low-pressure section the driven or test section. The simplest design is to have the same cross–sectional area on both sides of the diaphragm. The pressure difference is maintained by the diaphragm until it is ruptured, either by piercing the diaphragm with a mechanically-actuated arrow or else by raising the pressure to force the diaphragm against cutting edges. When the diaphragm is ruptured, the pressure difference between the driver and test section is resolved by a system of waves, shown in Figure 1. A shock wave propagates to the right into region 1 (driven section) and an expansion wave propagates to the left into region 4 (driver). This sets up a flow in regions 2 and 3. It is the flow in region 3 that is under consideration for simulating the conditions inside a pulse detonation engine. The pressure and velocity in region 3 can be

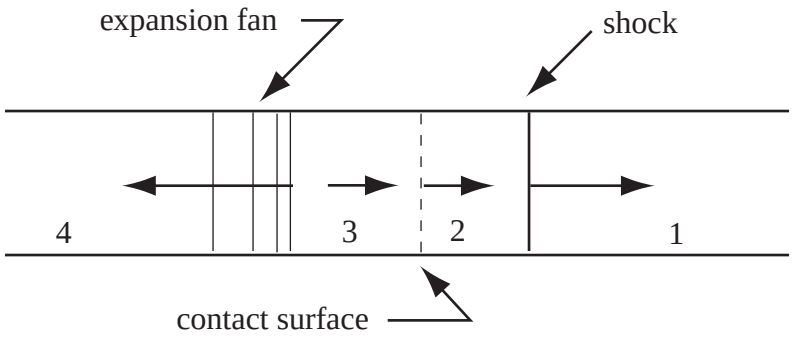

Figure 1: Wave system just after ideal diaphragm rupture in a shock tube.

determined by standard gas dynamics considerations. The driver is initially at a pressure of $P_{4,S}$ and the receiver is initially at P_1. The fluid in between the expansion fan and the contact surface will be at a pressure of P_3 and will be moving at a velocity u_3. The fluid behind the shock wave will be at a pressure of P_2 and will be moving at a velocity

u_2. A contact surface separates the fluid at states 2 and 3. Across the contact surface $u_2 = u_3$ and $P_2 = P_3$. The pressure ratio across the expansion wave P_3/P_4 is related to the velocity u_3 and can be found by considering the Riemann invariants across the expansion wave

$$\frac{2c_4}{\gamma - 1} = u_3 + \frac{2c_3}{\gamma - 1} \tag{1}$$

and the definition of sound speed

$$c = \sqrt{\gamma RT} \tag{2}$$

to obtain the temperature ratio

$$\frac{T_3}{T_4} = \left[1 - \frac{(\gamma - 1)}{2}\frac{u_3}{c_4}\right]^2 . \tag{3}$$

The pressure ratio can be found from the isentropic flow property relations

$$\frac{P_3}{P_4} = \left(\frac{T_3}{T_4}\right)^{\frac{\gamma}{\gamma-1}} \tag{4}$$

$$\frac{P_3}{P_4} = \left[1 - \frac{(\gamma - 1)}{2}\frac{u_3}{c_4}\right]^{\frac{2\gamma}{\gamma-1}} . \tag{5}$$

The conditions in state 2 are determined by the shock wave relationships. The pressure P_2 behind the shock is related to the velocity u_2 by

$$\frac{P_2}{P_1} = 1 + \frac{\gamma(\gamma+1)}{4}\left(\frac{u_2}{c_1}\right)^2 \left[1 + \sqrt{1 + \left(\frac{4}{\gamma+1}\frac{c_1}{u_2}\right)^2}\right] \tag{6}$$

This equation has to be solved together with Eq. 5 to determine the states 2 and 3 as a function of the pressure ratio P_4/P_1, γ, and the sound speeds c_4 and c_1. Solutions and implications for the facility design are presented below.

2.1.2 Blowdown design

A blowdown wind tunnel design, shown in Figure 2, consists of two large reservoirs connected by a smaller test section. The driver reservoir is initially at a pressure of $P_{4,B}$ and the receiver is initially at a pressure of P_1 where $P_{4,B} > P_1$. Again, the pressure ratio is initially supported by a diaphragm. Removal of the diaphragm results in a shock propagating into the receiver and an expansion fan propagating toward the driver reservoir. The expansion wave accelerates the gas in the driver reservoir through converging nozzle into the test section. Once the wave transients have settled down, steady flow will result as the high-pressure gas from the driver is accelerated into the test section and exhausted

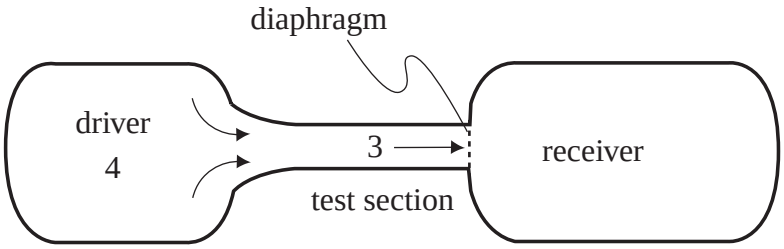

Figure 2: Schematic diagram of the test facility based on blowdown of a pressurized supply (driver) vessel into a receiver vessel.

into the receiver vessel. The flow can be considered to be approximately steady as long as the stagnation conditions of the driver are changing slowly relative to the time scale of interest, the test duration. This is found to be the case in the present facility although the influence of the finite size of the driver must be taken into account, resulting in a quasi-steady flow condition as the driver pressure changes during the test.

The flow from the driver to the test section can be modeled as adiabatic and the stagnation enthalpy is constant

$$h_4 = h_3 + \frac{u_3^2}{2} \tag{7}$$

so that the temperature ratio is

$$\frac{T_3}{T_4} = 1 - \frac{(\gamma - 1)}{2}\frac{u_3^2}{c_4^2} \, . \tag{8}$$

Assuming care has been taken to smoothly accelerate the flow from the driver into the test section, the flow in the transition from the driver to the test section can be modeled as an isentropic expansion. The pressure ratio can then be computed as

$$\frac{P_3}{P_4} = \left(\frac{T_3}{T_4}\right)^{\frac{\gamma}{\gamma-1}} \tag{9}$$

$$\frac{P_3}{P_4} = \left(1 - \frac{(\gamma - 1)}{2}\frac{u_3^2}{c_4^2}\right)^{\frac{\gamma}{\gamma-1}} \, . \tag{10}$$

Initially, the flow in the test section will be created by the unsteady wave processes associated with breaking the diaphragm. Later on, once a steady flow is set up, the flow in the test section will be determined by the steady-flow Mach number area relationship

$$\frac{A}{A^*} = \frac{1}{Ma}\left(\frac{2}{\gamma+1} + \frac{\gamma-1}{\gamma+1}Ma^2\right)^{\frac{\gamma+1}{2(\gamma-1)}} \tag{11}$$

if the flow is subsonic from the driver up to the end of the test section. The location of a possible sonic condition (*) in the flow will depend on the geometry and the pressure

ratio between the driver and the receiver. For sufficiently large pressure ratios

$$\frac{P_4}{P_1} \geq \left(\frac{\gamma+1}{2}\right)^{\frac{\gamma}{\gamma-1}} \tag{12}$$

the flow will either be sonic at the exit of the test section (inside the receiver) or if there is a minimum area point (throat) in the test section, it will be sonic (choked) there.

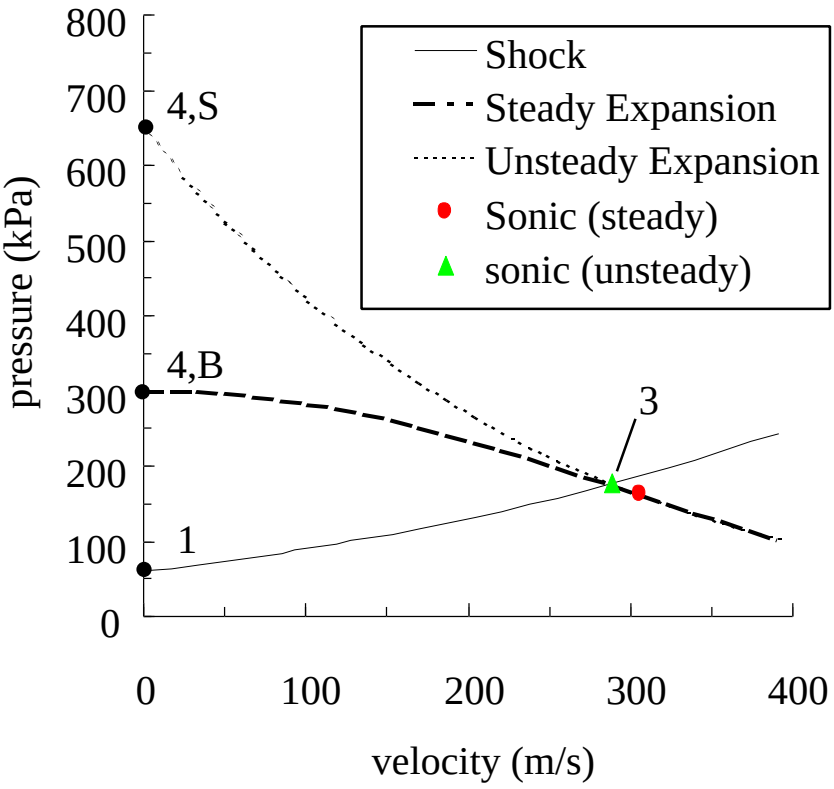

Figure 3: Comparison of steady and unsteady expansion processes on a pressure-velocity diagram. Design state (3) is identical for both the shock tube and blowdown design. The corresponding value of initial pressure, P_4, is solved from equations 5 and 10. $P_{4,S}$ = 650 kPa, $P_{4,B}$ = 300 kPa, $P_3 = P_2$ = 175 kPa, $u_3 = u_2$ = 293 m/s, P_1 = 60 kPa. The temperature of the fluid in states 4 and 1 is 300 K and $\gamma = 1.4$. The sonic states indicate a Mach number of unity for the state (3) at that pressure in the test section.

2.1.3 Test Section and Supply Vessel Temperatures

Note that to achieve identical test section states (u_3, P_3), the shock tube design must start at a much higher pressure $P_{4,S}$ than the starting pressure of the blowdown design $P_{4,B}$. This is illustrated for a specific test case in Figure 3 and in general for Figure 4. In other words, over the velocity regime of interest, the blowdown design requires less flow expansion to achieve the same test section velocity as the shock tube design. Thus

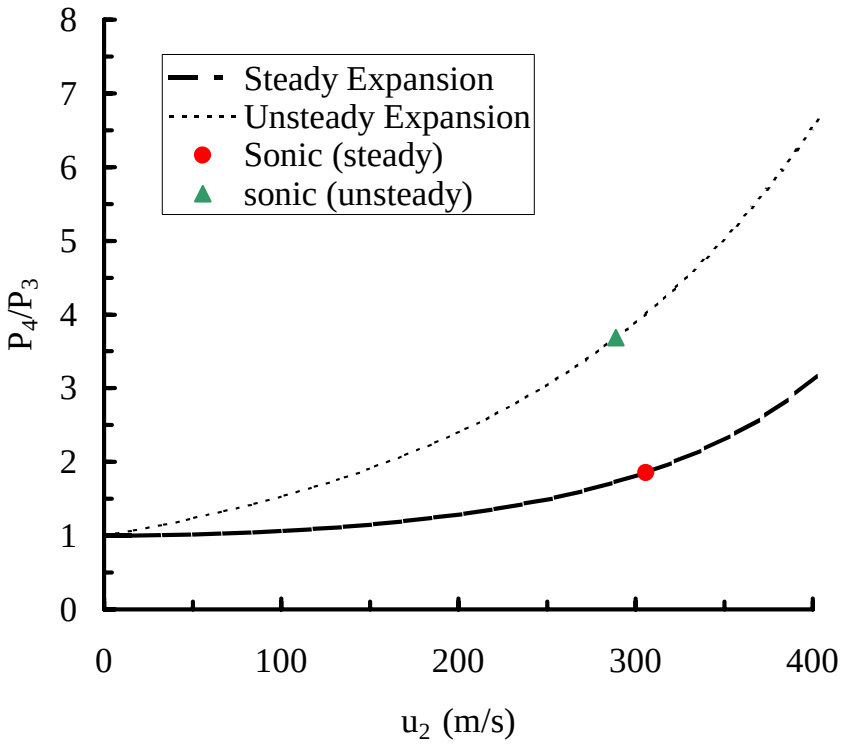

Figure 4: Pressure ratio required to obtain a given test section velocity. Comparison of steady and unsteady expansion processes. The temperature of the fluid at stagnation conditions is 300 K and $\gamma = 1.4$.

the blowdown flow at state (3) has a higher temperature than the shock tube flow at (3). This temperature difference ΔT_3 is illustrated in Figure 5.

Note that in practice, the flow in the steady expansion case may be choked due to friction or the presence of an area minimum (throat) in the flow path. If the throat is downstream of the test section, velocities in the test section will be be less then the sonic value. In Figure 3, this corresponds to all states to the left of the sonic state. For geometries with a minimum area upstream of the test section, it is possible for the flow to be either supersonic or subsonic in the test section.

The higher temperature flow of the blowdown design is more appealing because it allows the possibility of working with low vapor pressure fuels. Also, the blowdown design greatly increases the test time available for a given length of the facility. The useful test time of the unsteady facility will be approximately $2L/c_\circ$ where L is the length of the tube and $c_\circ$ is the initial sound speed. For a 3 m long tube, this is approximately 18 ms. The useful test time of a blowdown facility is determined by the volume of the tanks used for the receiver and driver, and the mass flow rate between them. In the facility that we constructed, the driver tank was about 1 m long and 1 m in diameter (400 L volume) and the useful test time was 130 ms with a 100 $\times$ 100 mm test section area.

In order to match precisely the temperature and pressure conditions of an air–

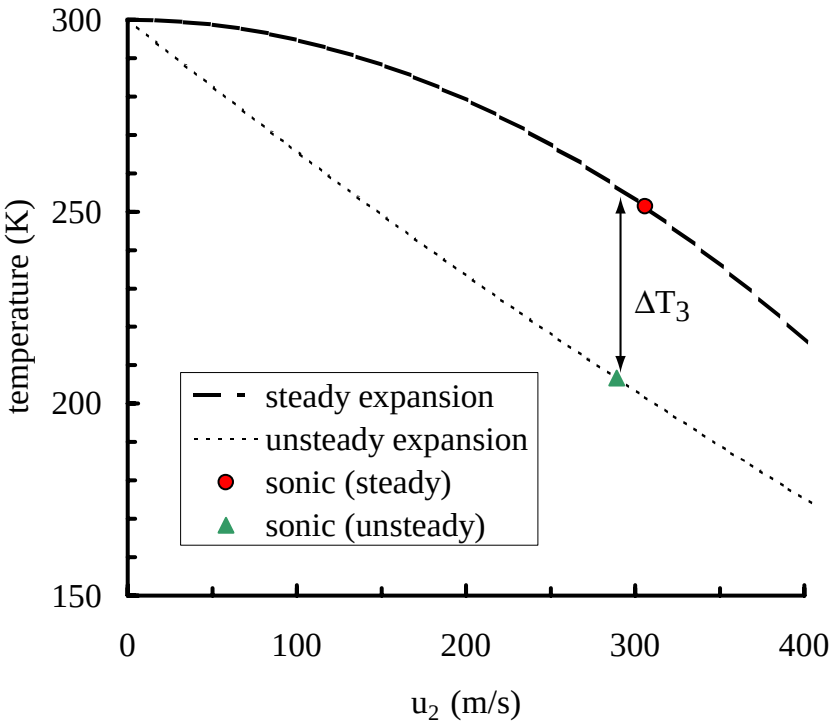

Figure 5: The temperature difference for the steady and unsteady expansion processes shown in Figure 3. Initial temperature at zero velocity is 300 K for both processes. The temperature difference at the design conditions ($P_3 = 175$ kPa, $u_3 = 293$ m/s) in Figure 3, labeled by ΔT_3.

breathing engine in flight, it would be necessary to heat the air in the driver vessel. The necessary temperature increase required to obtain a given temperature T_3 in the test section can be determined by rewriting the temperature relations for unsteady flow as

$$T_4 = T_3 \left(1 + \frac{\gamma - 1}{2} \frac{u_3}{c_3} \right)^2 \tag{13}$$

and for steady flow as

$$T_4 = T_3 \left[1 + \frac{\gamma - 1}{2} \left(\frac{u_3}{c_3} \right)^2 \right] \tag{14}$$

Since the sound speed c_3 is fixed once the temperature T_3 is specified, these relationships can be used to determine the reservoir temperature T_4 as a function of the flow velocity u_3 in the test section. The result is shown in Figure 6 for a test section temperature of 330 K, which is the temperature that would be required in order to obtain a stoichiometric mixture of JP-10 vapor in air at 100 kPa pressure in the test section at the threshold for condensation of the JP-10.

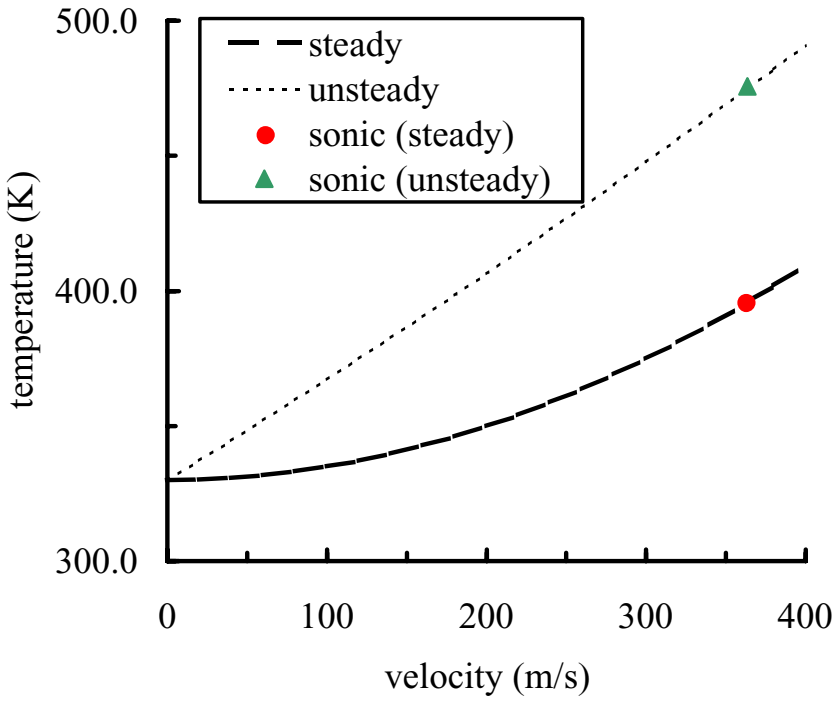

Figure 6: Comparison of driver temperature for steady and unsteady expansion processes with a fixed value of temperature in the test section. The temperature in the test section is 330 K and $\gamma = 1.4$.

Note that all of the computations carried out in this section on the steady or blowdown concept assume that the reservoir or driver is infinitely large. For realistic reservoir sizes, the mass flow out of the reservoir will result in expansion of the gas and a decrease in reservoir pressure and enthalpy. This effect must be accounted for in any realistic model of a facility. This is carried out in Section 5 and used to predict the variation of the reservoir properties as a function of time during the test. The model that we adopt is one of *quasi-steady behavior* with a time-dependent reservoir condition but assuming steady flow relationships through the inlet and test section at any given time. The test section property values obtained from the purely steady model are only valid at sufficiently early times that the reservoir conditions have not been affected by the blow-down process.

2.2 Numerical Simulations

Numerical simulations were used in the preliminary design process to examine several key issues. These simulations were carried out by Hornung[1] using the adaptive mesh refinement software Amrita [1]. The simulations solve the Euler equations of unsteady, inviscid, compressible flow of an ideal gas with constant specific heats. The solutions were carried out as initial value problems starting with the rupture of the diaphragm and continuing until an apparently steady flow was set up in the test section. The test section was modeled as a two-dimensional channel and the major features of the valve body geometry (open position) were modeled to scale.

Issues that were examined included:

1. Diaphragm location
2. Shock tube vs. blowdown operation
3. Effect of pressure ratio
4. Effect of valve body on startup and steady-state operation.

A list of the simulations and the relevant parameters is given in Appendix F. The valve body was modeled by 4 vanes in the flow with an additional step at the top wall. The bottom vane was flush with the bottom wall. The minimum area within the valve body was 70% that of the channel downstream of the valve body. The gas dynamics of the system were modeled for initial driver–receiver pressure ratios of 5 and 10. The effect of placing the diaphragm upstream or downstream of the valve body was also studied.

The first series of simulations (1–6) was performed with the shock tube model in order to study the flow near the valve body immediately after the diaphragm was removed. It was found that placing the diaphragm downstream of the valve body minimized the wave reflections off the valve body leading to shorter startup time, less losses, and a smoother test section flow. Placing the diaphragm upstream of the valve body made the flow difficult to start and caused large losses in the valve body due to the interaction of the initial shock with the vanes. In both cases, transient regions of supersonic flow were present in the valve body due to the high blockage ratio.

An example of a simulation with the diaphragm in the downstream location is shown in Figure 7. This is a case of a shock tube simulation with an initial pressure ratio of 10 and the diaphragm located downstream of the valve vanes. A close up view of the flow around the valve vanes, showing the contraction at the inlet and the wakes, is shown in Figure 8.

In carrying out the first set of simulations, two effects detrimental to the valve design were identified.

[1]Hans Hornung is the Kelly Johnson Professor of Aeronautics and the Director of the Graduate Aeronautical Laboratories at the California Institute of Technology in Pasadena, CA. He set up and carried out the simulations described in this section.

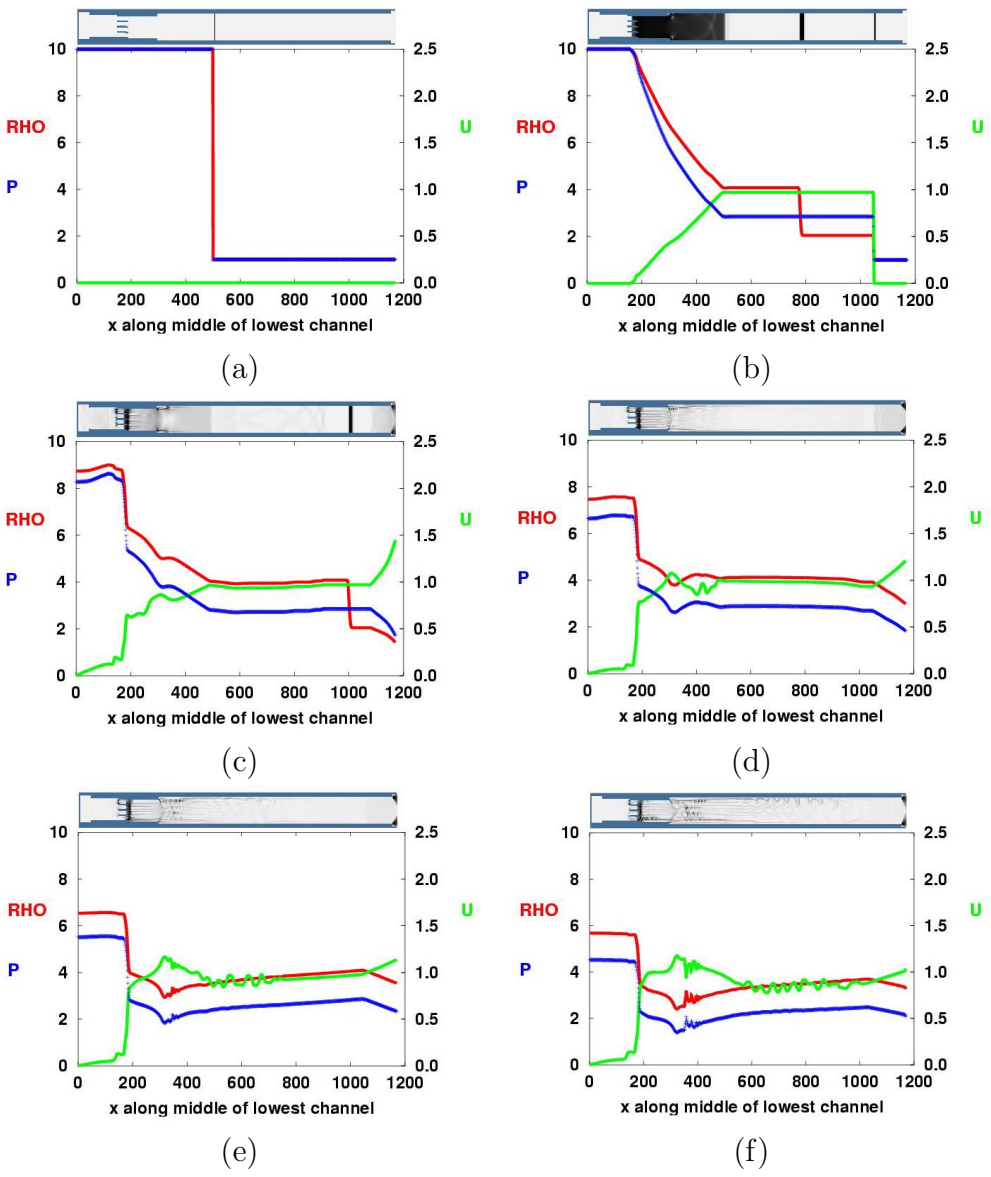

Figure 7: Schlieren images and spatial profiles at six times during a shock tube simulation of flow starting through a model valve body. The flow is from left to right and the initial pressure ratio is 10.

First, the separation across the blunt leading edge of the injector vanes results in poor flow quality within the valve body. It was decided that the injector vanes would not be modified for the current experiment but that this issue would be explored in future generations of injector designs.

Second, the large temperature drop across the expansion fan (previously discussed in Section 2.1) was identified as a problem in the shock tube design. The resulting low temperature flow entering the test section would cause condensation of most common

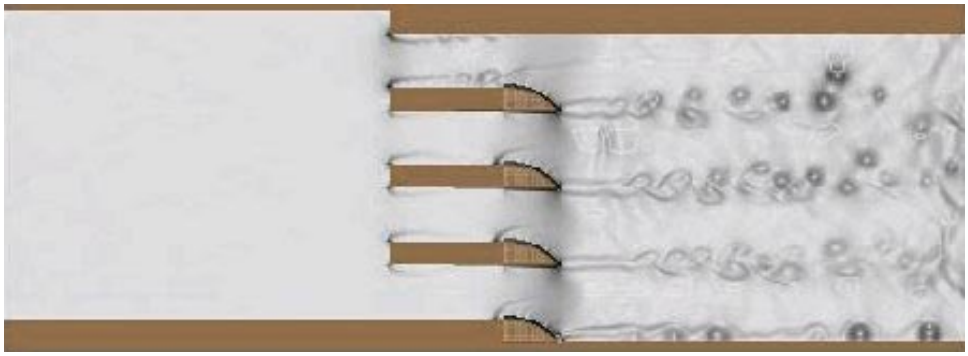

Figure 8: Schlieren image of flow through valve body vanes. The flow is from left to right and the initial pressure ratio is 10.

hydrocarbon fuels, see Table 1, leading to two-phase flow and poor mixing of the fuel with the air.

Table 1: Minimum temperature of hydrocarbon fuels for vapor phase at stoichiometric composition at 1 bar initial pressure.

fuel	formula	X_{st}	T_σ
pentane	C_5H_{12}	0.0256	-40°C
hexane	C_6H_{14}	0.0216	-17°C
octane	C_8H_{18}	0.0165	+24°C
JP-10	$C_{10}H_{16}$	0.0148	+60°C

In an effort to minimize the temperature drop in the flow, the blowdown design was adopted. The flow is started by an unsteady expansion fan but then a quasi-steady flow is set up in the converging nozzle between the reservoir vessel and the test section. Once the start-up transient is over, the temperature and pressure in the test section are determined by steady flow relationships.

A second set of simulations (simulations 8-11) examined the blowdown design compared to the shock tube design. These simulations verified that with an initial pressure ratio of 3 it was possible to achieve a similar velocity in the test section for the blowdown design as with an initial pressure ratio of 5 for the shock tube design. Results from a simulation of the blowdown design are shown in Figures 9 to 20. Spatial distributions of pressure, velocity, and temperature (all normalized) are shown along two directions in the flow. The lower plot is for a line along the x-direction through the center of the lower channel. The upper right plot is for a line in the y-direction just downstream of the valve body (x=275).

The initial configuration with the diaphragm downstream of the valve body is shown in

Figure 9. After the diaphragm is ruptured, a shock travels to the right and an expansion wave to the left, Figure 10. The expansion wave propagates through the valve body in Figures 12-13 and emerges on the other side (Figure 14), setting up a quasi-steady inflow after it has propagated into the reservoir located at the left-hand boundary (Figure 15). There is a sharp drop in pressure and increase in velocity at the entrance to the valve body and a series of vortices can be observed in the wake of the vanes making up the valve body. The flow within the vanes of the valve body appears to be separated and there is a jet-like region of central high-speed flow that is narrower than the actual channel dimensions. It is not clear how realistic some of these features are since this is an inviscid computation. Obviously, an inviscid code cannot correctly model separation of a boundary layer and the details of vortex formation in the wake region are also suspect.

The simulation predicts that the flow downstream of the valve is unsteady and the velocity increases as supersonic flow regions develop between the wakes of the vanes, Figures 16-19. The transverse velocity profile indicates complete separation just downstream of the vanes but relatively modest pressure fluctuations. The velocity profile along the center of the bottom channel shows large amplitude fluctuations as the jet emerging from the center of the channel flaps back and forth, creating a vortical flow. The temperature fluctuations are modest in all cases.

At the last frame of the simulation, Figure 20, large-amplitude pressure changes can be observed in the region downstream of the valve, indicating possible shock or compression waves. Some of these pressure changes are correlated with velocity changes but the magnitude of the changes in pressure and velocity are not consistent with one-dimensional shock jump conditions. The possible significance of the wakes and the shock waves to the performance of the facility is discussed further in Section 4.

The exact configuration of the supersonic flow regions and separation shown in the simulations may not be realized in the actual test facility. There are at least two reasons for differences. The simulations were performed with a two-dimensional approximate geometry that idealized and approximated the actual three-dimensional device that was tested. The test article had a smooth transition from the wall to the upper and lower valve passages. This would reduce the intense separation at the upper and lower valve passages that is evident in the simulations. The simulation is inviscid and does not correctly model the physics of the boundary layer, the separation process or the small scales of turbulent motion. For these reasons, the separated and supersonic flow regions are not quantitatively predicted but the simulations only give an indication for the potential of separation and supersonic flow.

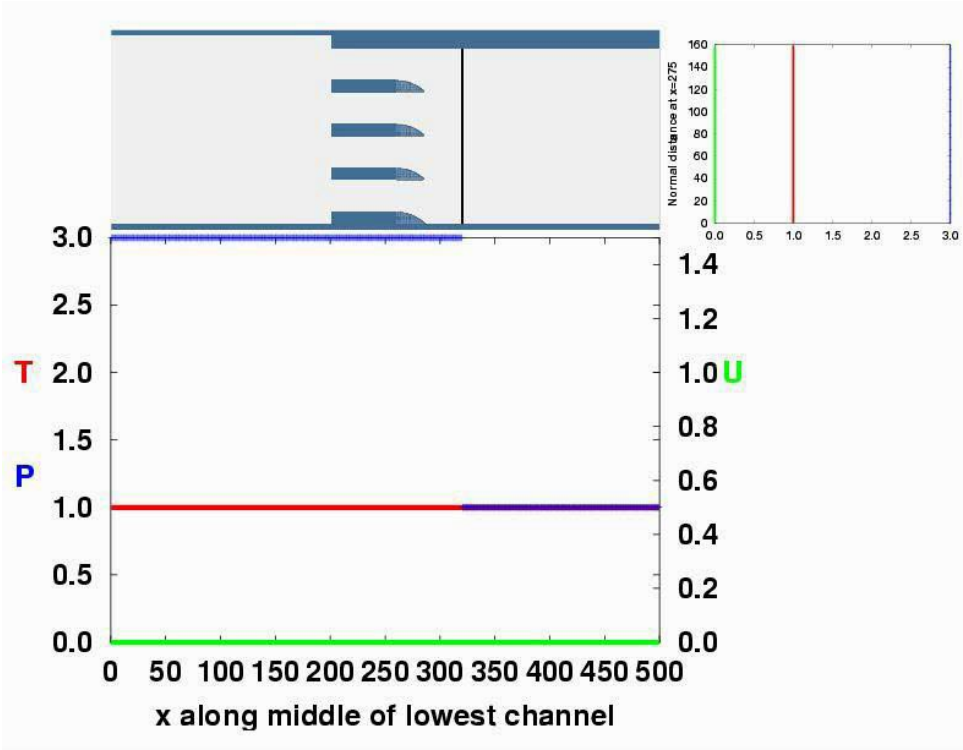

Figure 9: Numerical schlieren of simulation for reservoir blow down with shock tube start up. The flow is from left to right and the initial pressure ratio is 3. Frame 000 of simulation pr3xd320.

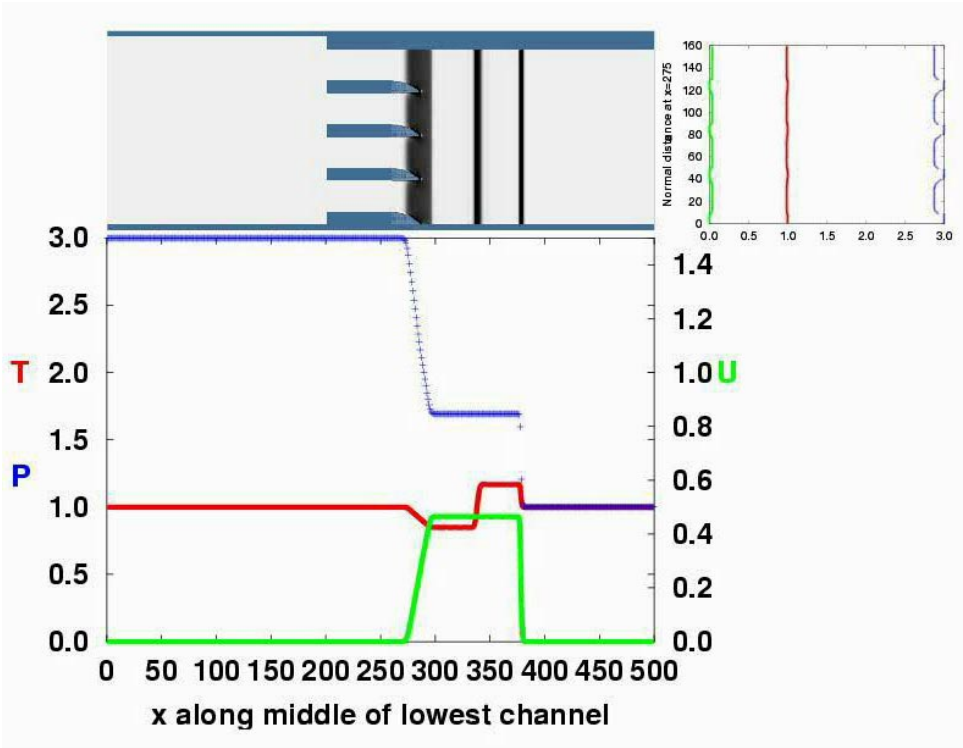

Figure 10: Numerical schlieren of simulation for reservoir blow down with shock tube start up. The flow is from left to right and the initial pressure ratio is 3. Frame 015 of simulation pr3xd320.

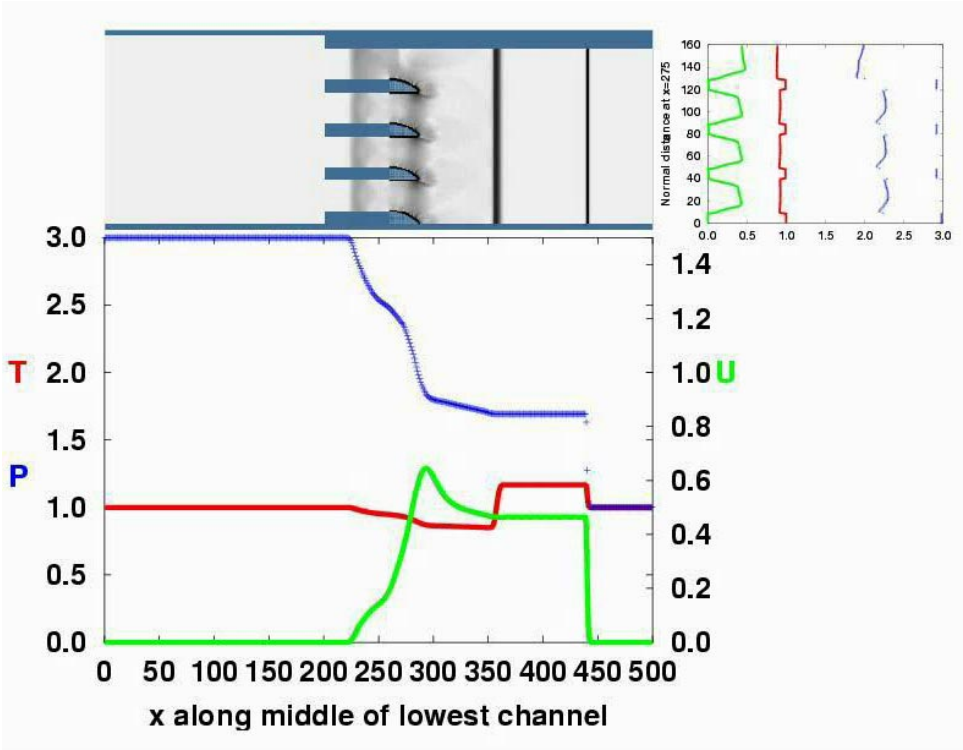

Figure 11: Numerical schlieren of simulation for reservoir blow down with shock tube start up. The flow is from left to right and the initial pressure ratio is 3. Frame 030 of simulation pr3xd320.

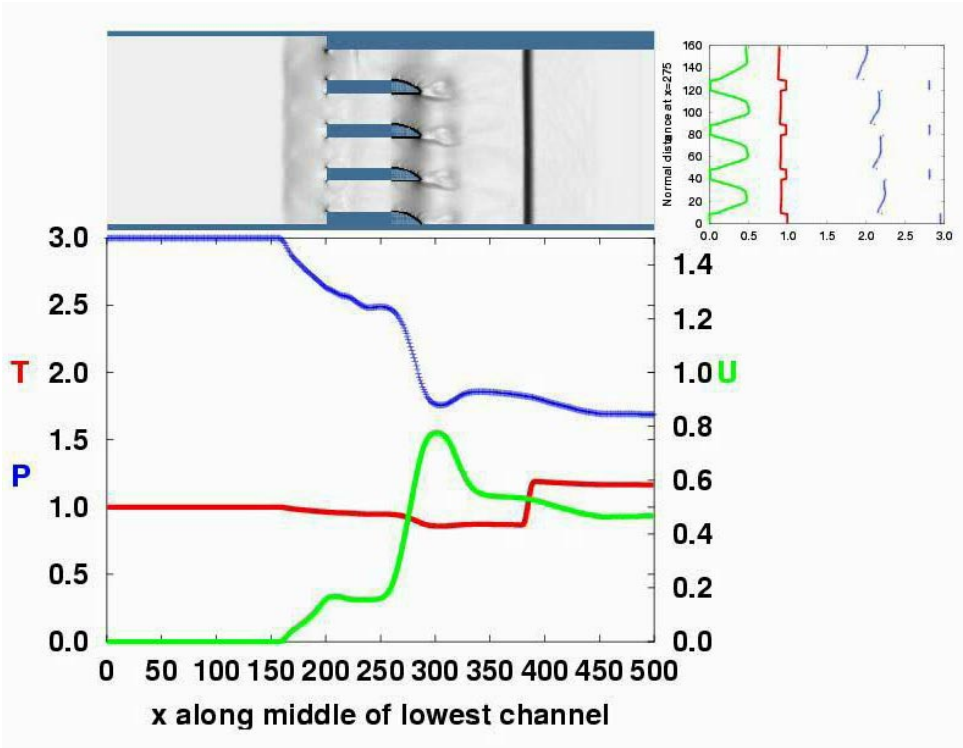

Figure 12: Numerical schlieren of simulation for reservoir blow down with shock tube start up. The flow is from left to right and the initial pressure ratio is 3. Frame 050 of simulation pr3xd320.

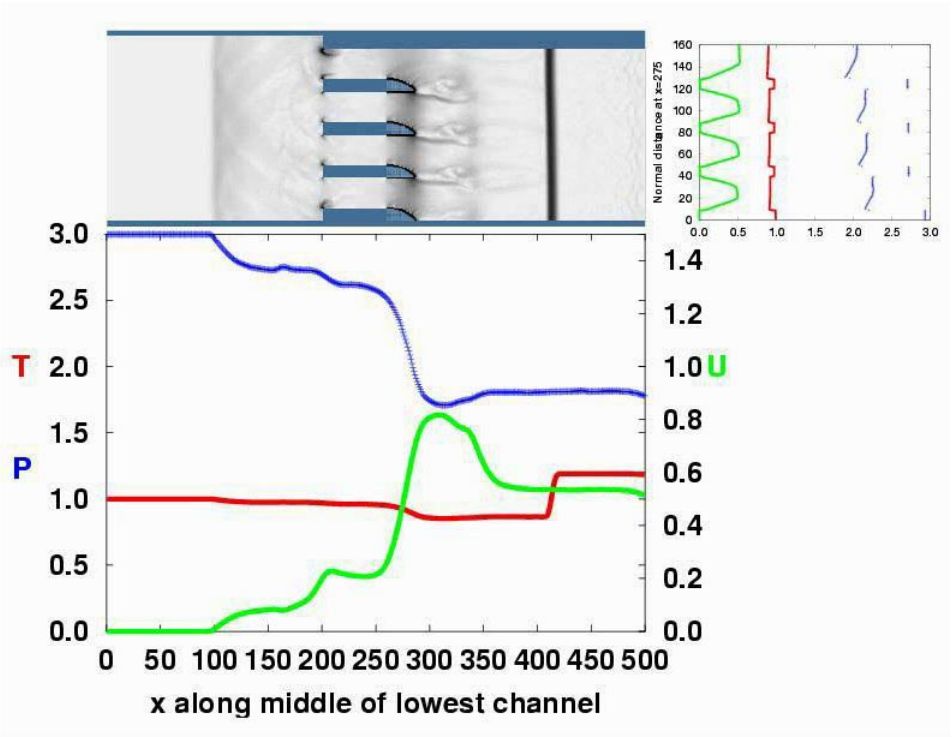

Figure 13: Numerical schlieren of simulation for reservoir blow down with shock tube start up. The flow is from left to right and the initial pressure ratio is 3. Frame 070 of simulation pr3xd320.

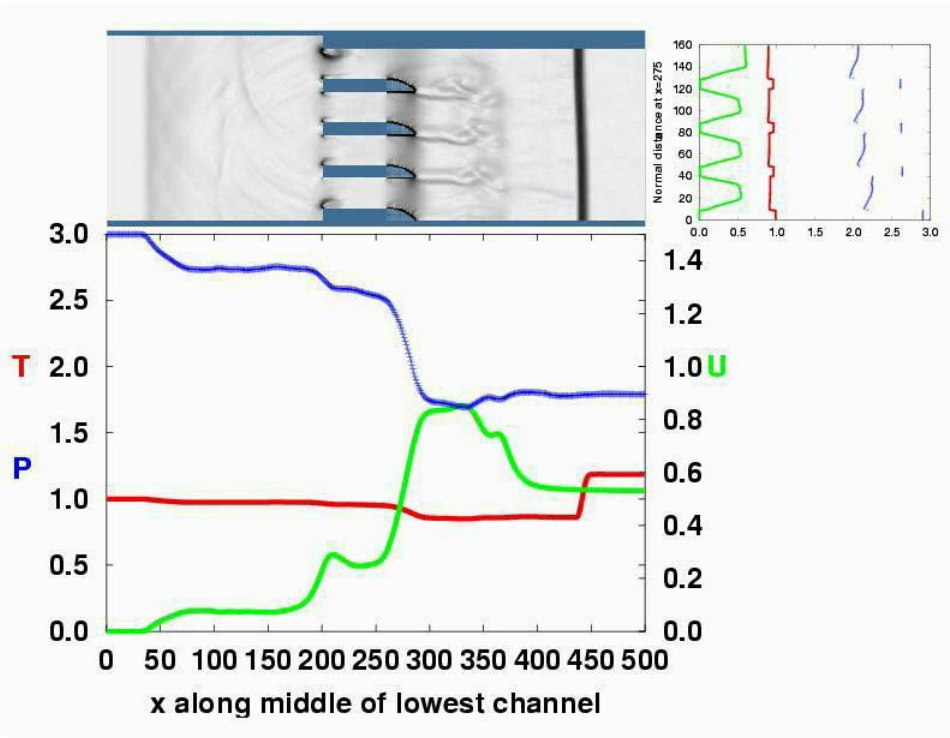

Figure 14: Numerical schlieren of simulation for reservoir blow down with shock tube start up. The flow is from left to right and the initial pressure ratio is 3. Frame 090 of simulation pr3xd320.

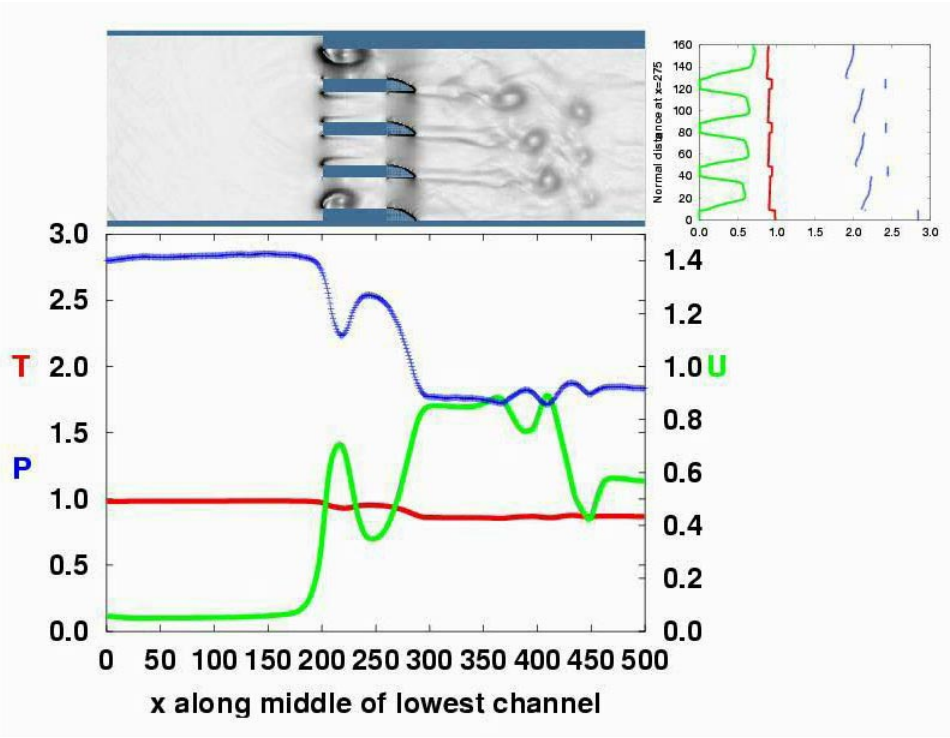

Figure 15: Numerical schlieren of simulation for reservoir blow down with shock tube start up. The flow is from left to right and the initial pressure ratio is 3. Frame 150 of simulation pr3xd320.

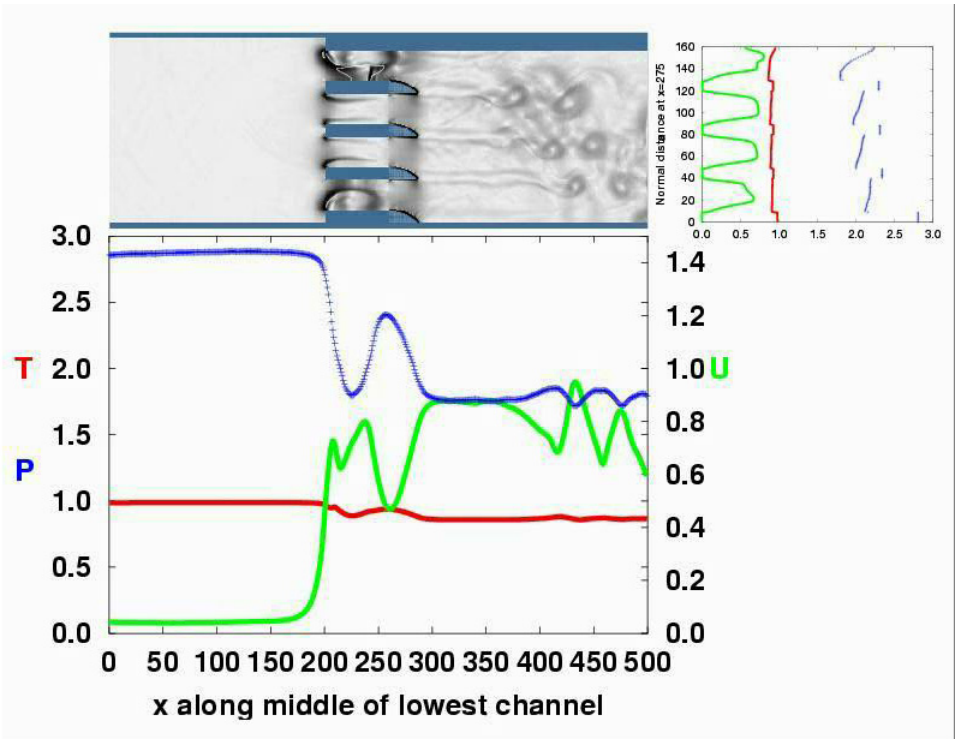

Figure 16: Numerical schlieren of simulation for reservoir blow down with shock tube start up. The flow is from left to right and the initial pressure ratio is 3. Frame 200 of simulation pr3xd320.

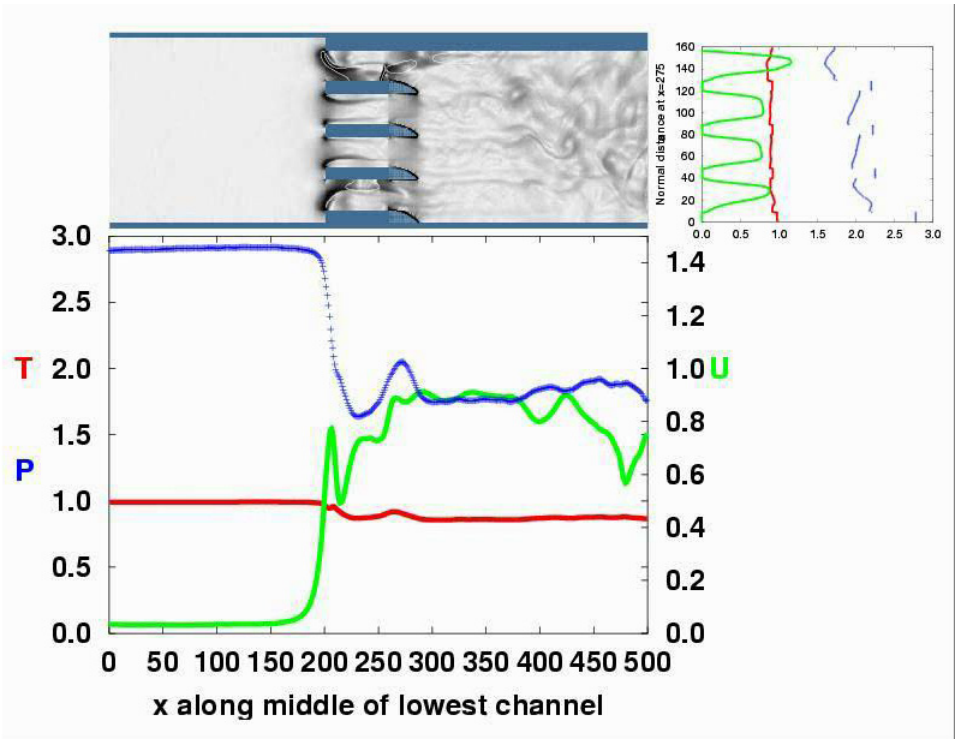

Figure 17: Numerical schlieren of simulation for reservoir blow down with shock tube start up. The flow is from left to right and the initial pressure ratio is 3. Frame 250 of simulation pr3xd320.

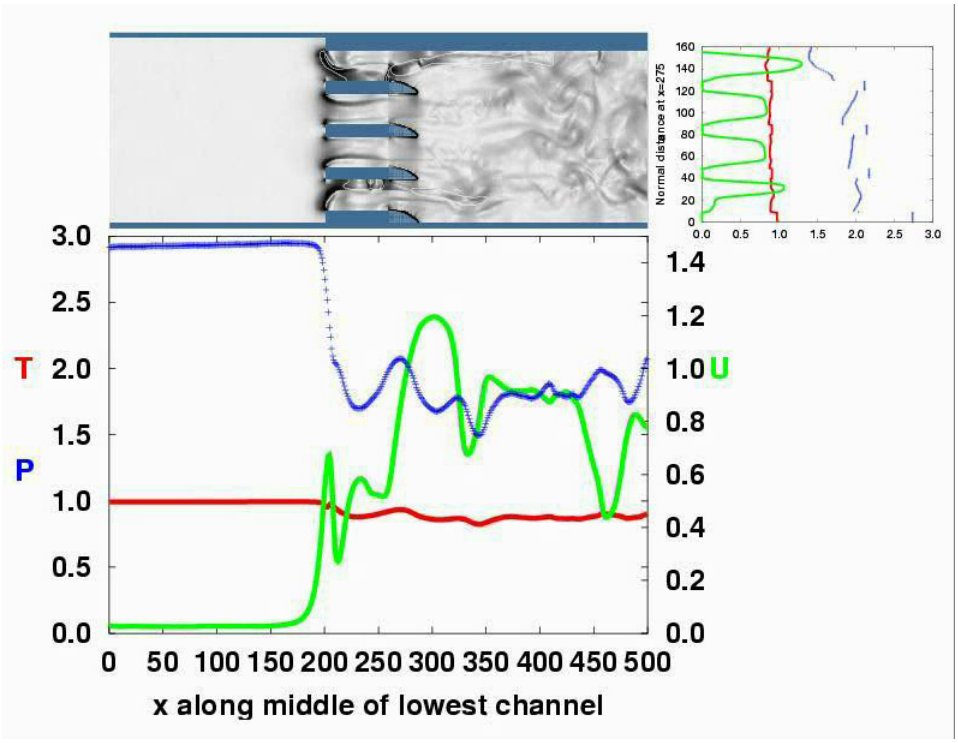

Figure 18: Numerical schlieren of simulation for reservoir blow down with shock tube start up. The flow is from left to right and the initial pressure ratio is 3. Frame 300 of simulation pr3xd320.

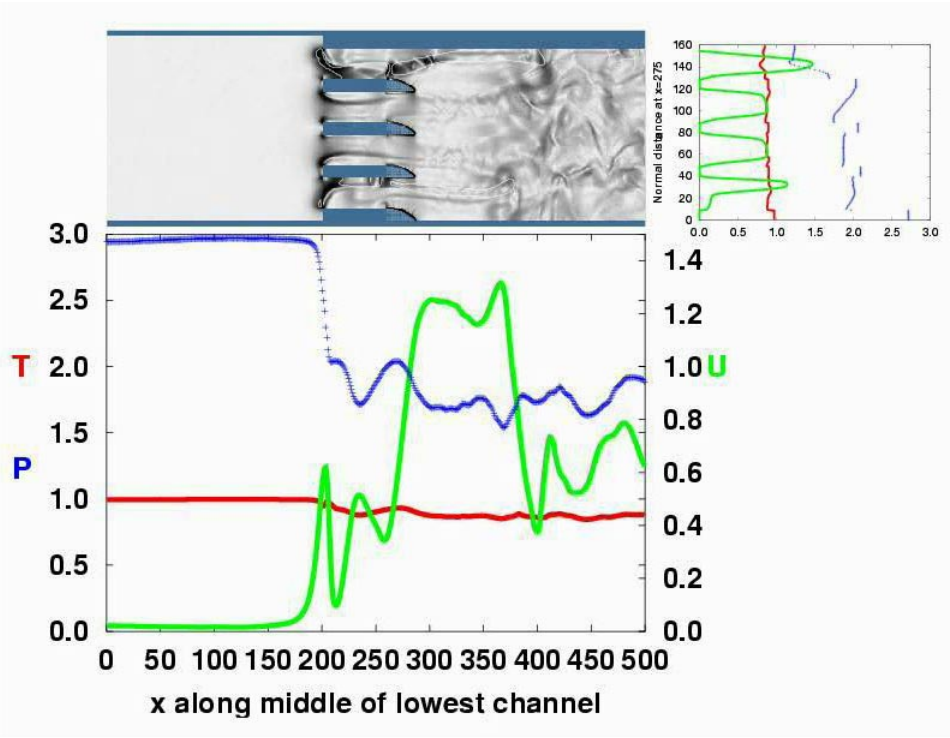

Figure 19: Numerical schlieren of simulation for reservoir blow down with shock tube start up. The flow is from left to right and the initial pressure ratio is 3. Frame 350 of simulation pr3xd320.

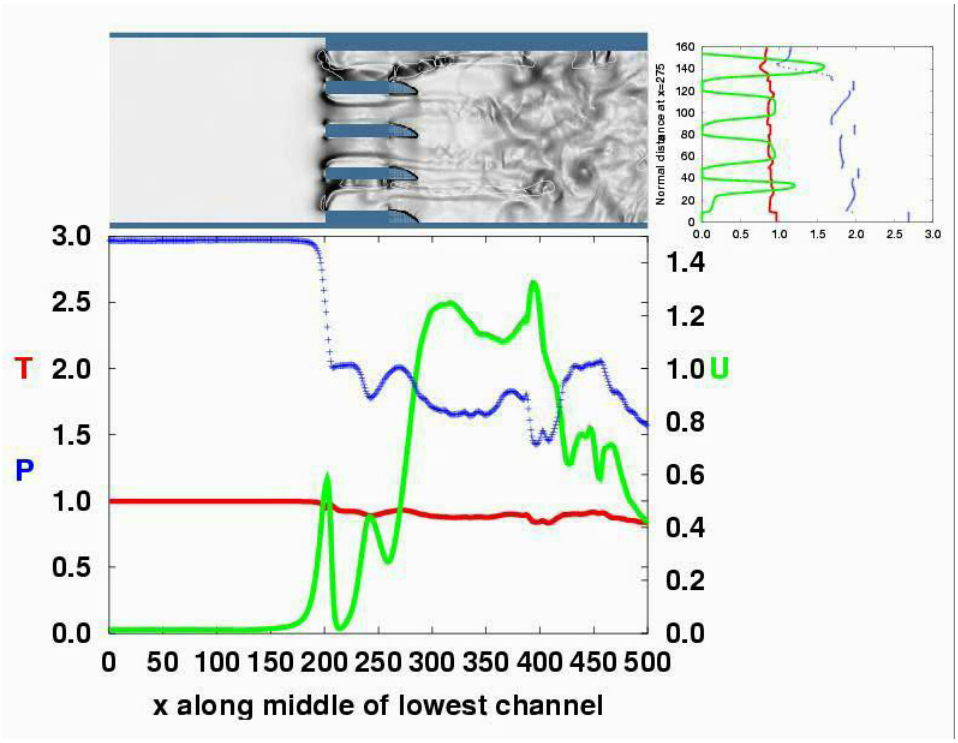

Figure 20: Numerical schlieren of simulation for reservoir blow down with shock tube start up. The flow is from left to right and the initial pressure ratio is 3. Frame 399 of simulation pr3xd320.

3 Facility Description and Operation

The facility consists of five main components: a supply tank or driver, a valve-injector system, a test section, a diaphragm holder and piercing system, and a receiver tank. The following section describes the relevant features of each component. Schematic diagrams of the facility are shown in Figures 21 and 22.

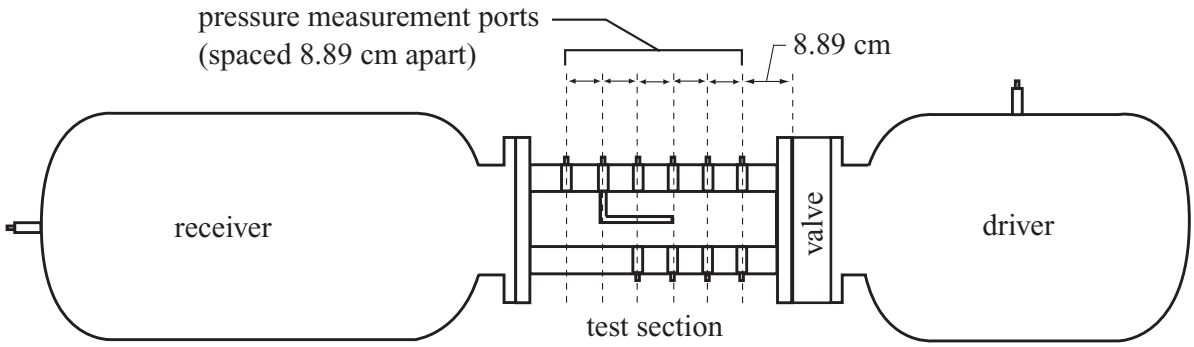

Figure 21: Schematic of the facility showing the major components. The diaphragm is located between the test section and the receiver vessel.

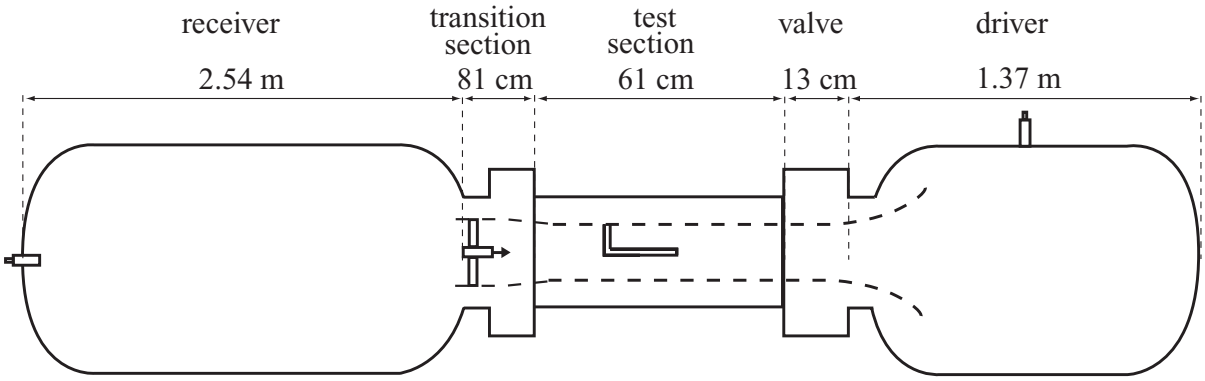

Figure 22: Key facility dimensions. Not to scale.

3.1 Basic Components

The driver or supply vessel, shown in Figure 23, is a 407 liter vessel with a maximum pressure rating of 42 bar. The vessel is connected to the valve and test section through a nozzle (Figure 24). The nozzle is intended to smoothly accelerate the flow and minimize the stagnation pressure loss so that the flow approximates quasi-steady, isentropic motion. The driver section is equipped with a thermocouple for static temperature measurements, a static pressure gauge for filling, and a piezoresistive pressure transducer for transient

pressure measurements during facility operation. Remotely-operated valves attach the vessel to the vacuum pump, exhaust vent, and building air supply line. The building compressed air supply is filtered and dried before it enters the vessel.

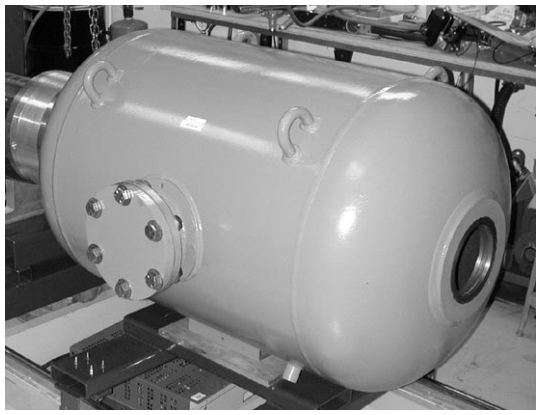

Figure 23: The 407 liter supply or driver vessel.

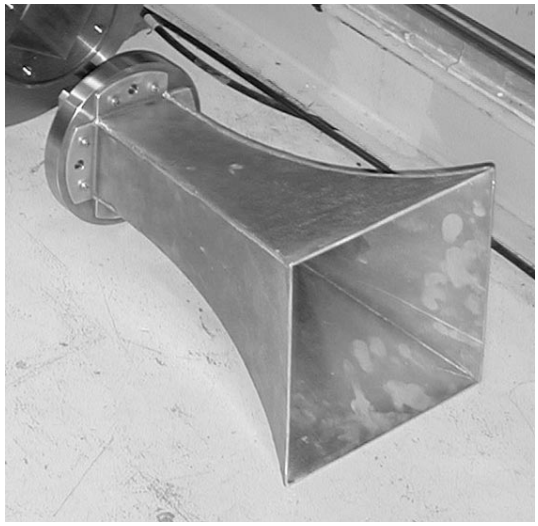

Figure 24: The nozzle used to accelerate the flow from the supply vessel into the test section. When installed, the nozzle is located inside the supply vessel.

The valve–injector unit is located between the test section and the supply vessel. This unit is used to inject fuel into the air flowing into the test section and is also be used to stop the flow when simulating pulse detonation engine operation. Fuel is injected from a 2 liter fuel reservoir located close to the valve–injector body to maintain constant fuel flow rate during injection. The valve closure speed is controlled by a pneumatic actuation system. When open, the cross–sectional flow area of the valve–injector is 58% that of the cross–sectional flow area of the test section. For initial testing, the valve–injector unit was replaced by a rectangular duct of the same length, termed the "valve body blank".

The test section, shown in Figures 25 and 26, has a square cross section that is 10 cm $\times$ 10 cm and is 61 cm in length; it is located between the valve–injector system and the transition section. There are two polycarbonate windows with a viewing area of 10 cm x 51 cm. A schlieren system, described in Krok [2] enables flow visualization in the test section. The test section is also equipped with 10 instrument ports that can be filled with pressure transducers or spark plugs. Both piezoresistive and piezoelectric pressure transducers are used in the test section. Piezoresistive transducers were used for tests without combustion. Piezoelectric gauges were used to record data from tests with combustion. Automotive long reach spark plugs were used for ignitors in some tests.

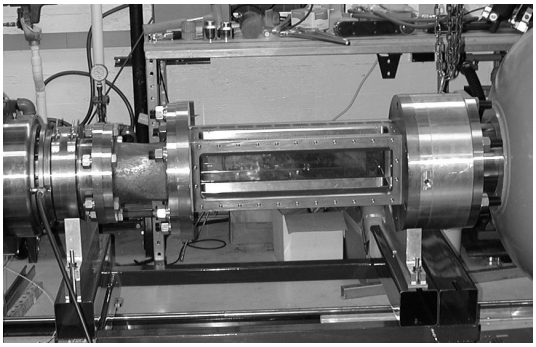

Figure 25: Test section installed in the facility with valve body blank on right and transition section to left. The instrument plates and windows are not installed.

Figure 26: View of installed test section with valve-injector unit on right and transition section to the left. Instrument plates are installed on the top and bottom of the test section. Plastic windows are mounted on both sides of the test section. Four spark plug arms are visible protruding from the bottom test section wall.

The receiver tank (Figure 27) is a 1200 liter vessel with a maximum operating pressure of 51 bar. The receiver tank is equipped with a piezoresistive pressure transducer for static

and dynamic pressure measurements. A hydraulic diaphragm clamp [2] and diaphragm piercing mechanism (Figure 28) are situated between the test section and the receiver vessel. The piercing mechanism is a arrowhead mounted on a pneumatically-actuated rod. The receiver tank can be pressurized or evacuated as desired from the control panel at the operators console.

The diaphragm maintains a pressure difference between the driver and receiver during filling. Both aluminum and mylar were used as diaphragm materials in the present tests. A transition section separates the test section and the diaphragm clamp. This section is a casting that gradually changes the flow area from the square cross–section in the test section to a 12.7 cm diameter circular cross section at the diaphragm clamp. The receiver also contains vacuum and fill line ports. Data is collected via two National Instruments

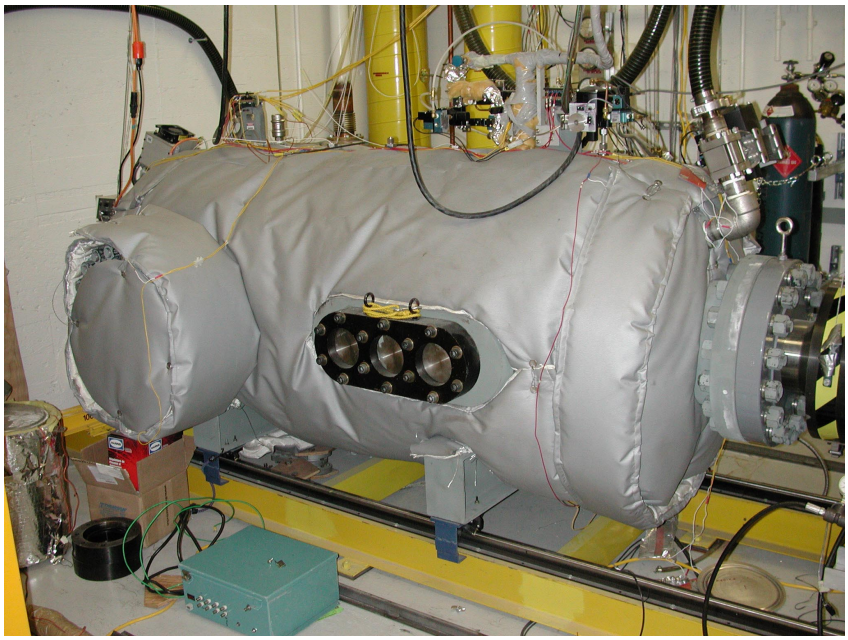

Figure 27: Receiver vessel mounted on linear bearings and attached to diaphragm clamp at right.

PCI-6110E data acquisition (DAQ) cards operating in master-slave configuration. The data acquisition is managed by Labview software. The Labview program used for data collection. During an experiment, the DAQ cards are triggered from the same TTL pulse that triggers the diaphragm breaker circuit. The data acquisition system is capable of recording 8 simultaneous channels of data at frequencies of up to 5 Mhz.

The assembled facility is shown in Figure 29. The test section, the receiver vessel, and the supply vessel are supported by linear bearings on a common track. When the diaphragm clamp is in the open position, the receiver and supply vessels can be moved apart to insert a new diaphragm. The operation of opening the system, inserting a diaphragm, and resealing the system takes less than 5 minutes.

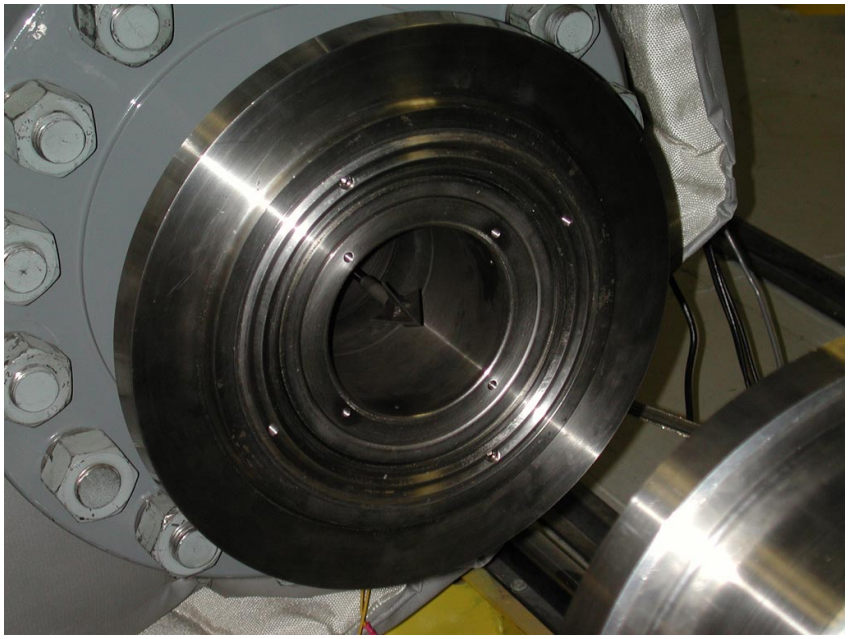

Figure 28: Diaphragm cutter and clamp. Receiver vessel is to the left.

Figure 29: View of completed facility with diaphragm clamp engaged. The red boxes visible to front and back of the test section contain the schlieren optics.

3.2 Configurations Tested and Operation

The facility has undergone five separate stages of testing in order to characterize its operation. First, blowdown tests were conducted without the valve-injector unit installed.

A second series of tests were run with the valve-injector unit installed and left open to examine losses introduced by flow through the vanes in the flow path. Valve actuation and fuel injection during blowdown were then tested. Finally, spark plugs were operated after fuel injection and valve closure to simulate a complete cycle of a pulse detonation engine. This report will focus on initial facility characterization. The results of fuel injection and combustion tests will not be discussed here. The non–combusting tests carried out at Caltech are summarized in Table 2 of Appendix B. These can be broken down into three sets.

3.2.1 No valve installed

For initial blowdown tests (Shots 001–012), the valve-injector unit was removed from the facility and replaced with the open channel (valve body blank). A series of tests was run to characterize the blowdown operation of the facility at different pressure ratios. In a typical run, a diaphragm was inserted into the diaphragm clamp. The supply vessel was filled with air and the receiver vessel evacuated to the desired pressures. The diaphragm was then ruptured and pressures in the driver, test section and receiver were recorded during blowdown. A pitot probe and a static gauge were present in the test section to facilitate velocity measurements.

3.2.2 Valve installed

The valve-injector unit was then installed and tests (Shots 013-18) were run with no fuel injection, the valve open, and not actuated for the duration of each test. The experimental procedure was the same as without the valve installed. This allowed characterization of the effect of the valve unit on the flow as compared to cases where the valve was not installed.

3.2.3 Valve installed and actuated

In a third series of runs (Shots 019–34), valve actuation during blowdown was tested. The experimental procedure was similar to the previous series of tests, however, during the blowdown process the valve was closed, stopping the flow from the driver to the test section. The goal was to test the ability and timing of the valve to gas dynamically shut off the flow from the driver. Some refinement of initial pressures and valve supply gas pressure was necessary to achieve as crisp a flow shut off as possible.

4 Results

The raw data from each test discussed by this report are given in Appendices C, D, and E. The primary data sources are the four piezoresistive pressure transducers and four piezoelectric pressure transducers in the test section. A schematic of the pressure transducer locations is shown in Figure 30. The driver and receiver also each contained

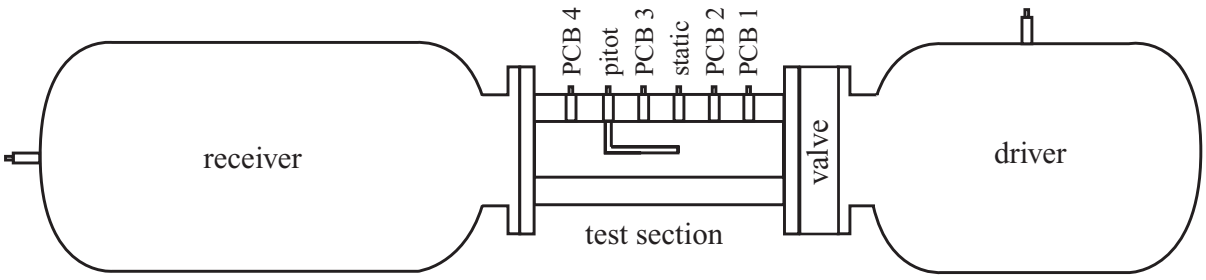

Figure 30: Schematic of the facility showing the locations of the pressure transducers in the tests with no valve.

one piezoresistive transducer. The test section contained two piezoresistive transducers in a pitot-static probe arrangement to infer velocity data. Four piezoelectric transducers were located along the test section top wall. During combustion testing, the pitot probe and static gauge were removed and replaced with piezoelectric transducers mounted flush with the wall.

In this section, we discuss typical results and use simple gas dynamics to analyze the pressure data to determine the flow conditions in the test section.

4.1 Typical results without valve

The results of each type of test are similar but the simplest tests to understand are those without the valve installed. These tests are all qualitatively similar and one case will be used to illustrate the key features of the results. The main data obtained are the pressure histories in the two vessels and the static and pitot pressure in the test section. A typical set of pressure data is shown in Figure 31. This is for Shot 005 with an initial pressure of 300 kPa in the driver and 60 kPa in the receiver and test section. Zero time is when the signal was transmitted to the piercing mechanism; the delay of about 0.13 s until the first pressure disturbance is due to the actuation time of the pneumatic system used to translate the arrowhead into the diaphragm. The flow begins at about 0.136 s when the diaphragm is ruptured and the expansion wave travels through the test section and is detected as a sharp drop at 0.141 s on the pitot and static gauges in the test section. The pressure in the driver vessel begins to drop and the pressure in the reliever vessel begins to increase after 0.142 s as the gas flows from the driver into the receiver. The pressures measured by the pitot and static probe quickly recover and then begin to slowly fall after 0.154 s. As the flow develops in the test section, the pitot pressure quickly reaches the

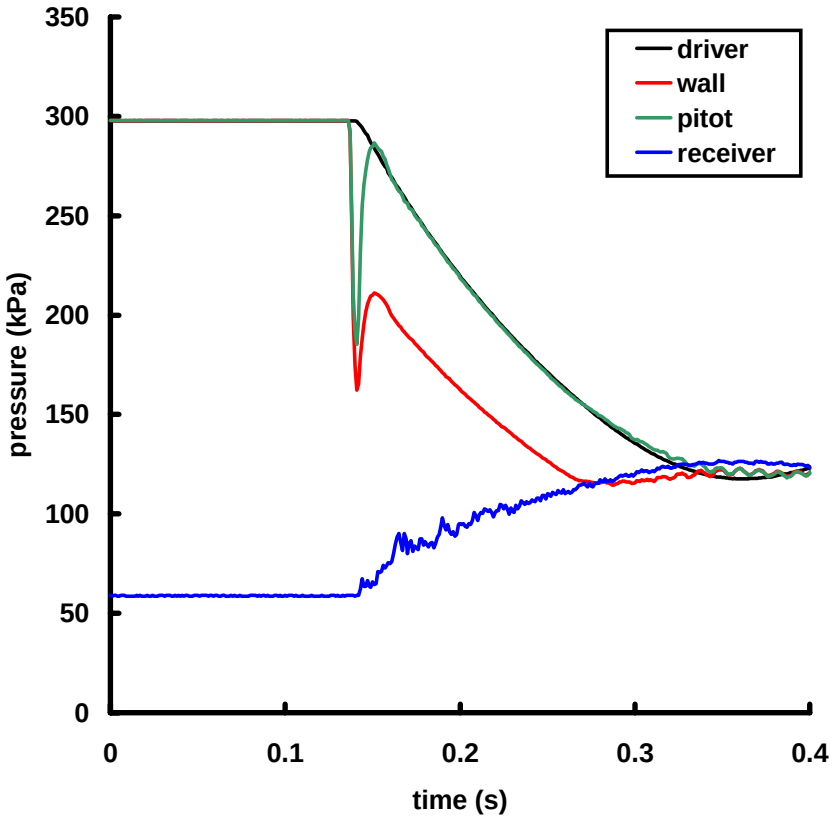

Figure 31: Measured pressures in Shot 005.

same value as the driver vessel static pressure, indicating minimal stagnation pressure loss through the nozzle and test section up to the pitot probe.

The period from 0.154 s to 0.270 s is characterized by the test section pressure being substantially greater than the receiver vessel pressure. This period, as we will see below, corresponds to the quasi-steady flow period that is useful for testing. During this time, the flow is choked at some point downstream of the pitot probe, resulting in a constant Mach number in the test section for this duration. Once the flow becomes unchoked after about 0.27 s, the flow is subsonic and the pressure within the test section is approximately constant at 115-120 kPa and comparable to the receiver pressure. Once the pressure in the driver falls to a level comparable to that in the receiver at about 0.357 s, measurable flow ceases. By 0.4 s, the driver and receiver are at a common pressure.

4.2 Analysis of data without the valve installed

The pitot probe and static pressure measurements in the test section can be used to infer other flow properties such as Mach number, temperature and density. First, the Mach number of flow in the test section is calculated using the isentropic Mach number-pressure

relation and the measured pitot and static pressures

$$Ma_3(t) = \sqrt{\frac{2}{\gamma-1}\left(\frac{P_5(t)}{P_3(t)}\right)^{\frac{\gamma-1}{\gamma}} - 1} \tag{15}$$

where P_3 is the static pressure and P_5 is the stagnation pressure in the test section. This equation is valid for subsonic flow in the test section. Supersonic flow requires considering the effect of a shock wave in front of the pitot probe; this was never found to be necessary in the tests carried out so far.

Due the the low flow velocity in the driver vessel, it is reasonable to assume that the static temperature in the driver is the total temperature of the flow. We also assume that the gas in the driver expands adiabatically and reversibly, i.e., isentropically, during the blowdown process. The driver static temperature probe time response was too slow to be useful for measuring the driver gas temperature directly so this was estimated from the driver static pressure history. With these assumptions, driver temperature can be computed from the measured pressure as

$$T_d(t) = T_d(0)\left(\frac{P_d(t)}{P_d(0)}\right)^{\frac{(\gamma-1)}{\gamma}} \tag{16}$$

where $P_d(0)$ and $T_d(0)$ are the initial pressure and temperature in the vessel at the start of the test.

In order to analyze the pitot and static pressure data, we assume that the flow from inside the driver vessel up to the location of the pitot probe is adiabatic and steady. The total temperature in the test section will be same as in the driver vessel so that the Mach number in the test section can be used to find the static temperature in the test section.

$$T_3(t) = \frac{T_d(t)}{1 + \frac{(\gamma-1)}{2}(Ma_3(t))^2} \tag{17}$$

The density at the pitot probe and in the driver vessel are then computed using the perfect gas law

$$\rho_3(t) = \frac{P_3(t)}{RT_3(t)}, \tag{18}$$

$$\rho_d(t) = \frac{P_d(t)}{RT_d(t)}. \tag{19}$$

The velocity u_3 at the pitot probe can then be calculated from the definition of Mach number and the inferred static temperature

$$u_3(t) = Ma_3(t)\, c(t) \tag{20}$$

where the sound speed in the test section is

$$c(t) = \sqrt{\gamma R T_3(t)}. \tag{21}$$

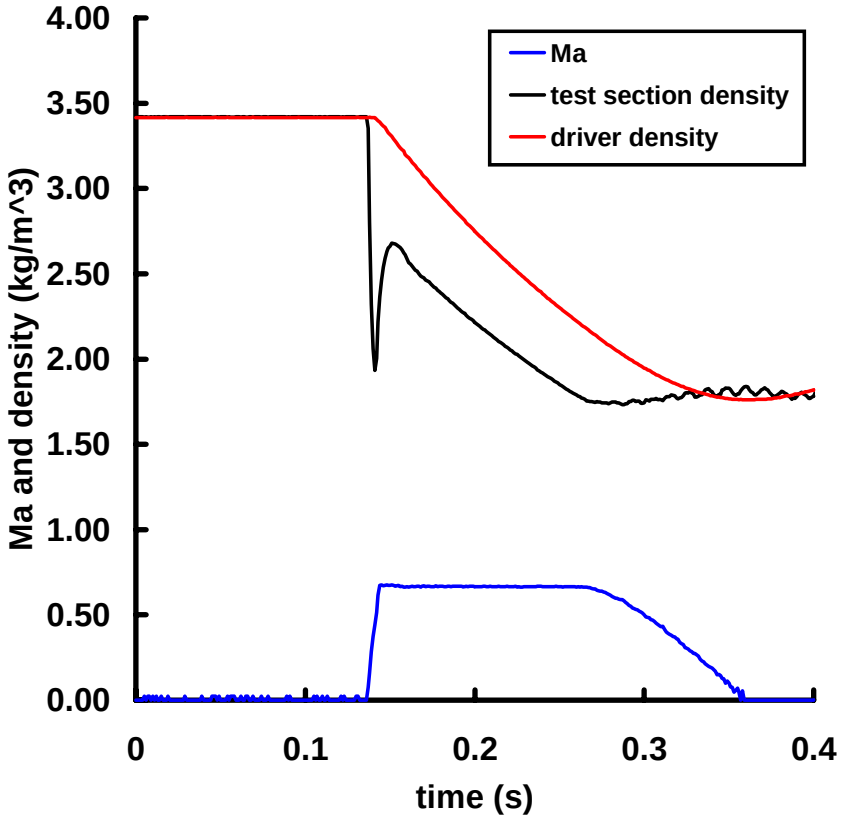

Figure 32: Mach number and density in the test section and the density in driver vessel. Analyses of data in Shot 005.

The results of analyzing the data of Figure 31 are shown in Figures 32, 33, and 34.

After the initial expansion wave sets up the flow, the Mach number remains constant for a total duration of about 0.12 s, indicating that the flow has choked. During this time the velocity, temperature and density steadily decrease with decreasing P_d and T_d. Once choking stops, the Mach number and velocity of the flow drops off rapidly. The full data set for testing without the valve (Shots 001-012) is shown in Appendix C.

During testing without the valve, initial driver pressures of 200 to 400 kPa were tested with driver-to-receiver pressure ratios between 3 and 10. For a given driver pressure, increasing the pressure ratio extended the quasi–steady operation time. At higher pressure ratios (8-10) a longer initial transient was observed before the flow underwent transition to quasi–steady blowdown.

4.2.1 Comparison to Pressure-Velocity Models

The data from these tests can be examined in view of the simple transient models and steady models developed in Section 2. As noted previously, the simple steady model is only suitable at early times, prior to significant changes in the reservoir properties.

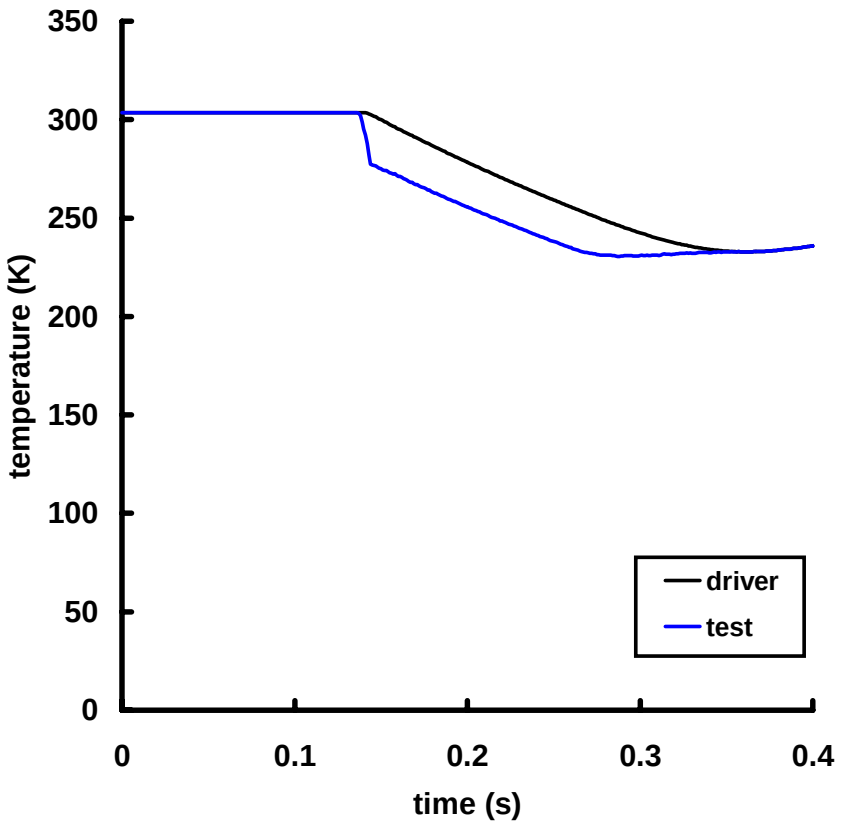

Figure 33: Static temperature in test section and driver vessel. Analyses of data in Shot 005.

A comparison of the early-time (0.136 to 0.155 s) data from shot 005 with the ideal P-u diagram is shown on Figure 35. As shown, the data initially follow the transient expansion wave solution with the decreasing pressure and increasing velocity. The ideal state obtained from the transient shock tube solution would be at the intersection of the unsteady expansion and shock curves, $u = 298$ ms/ and $P = 176$ kPa. This corresponds to a shock Mach number of 1.63. The shock wave cannot be observed in the plot since the diaphragm is located downstream of the static pressure gauge location.

The reflected waves generated by the interaction with the expansion with nozzle reach the static pressure gauge station after about 6 ms and the pressure begins to rise after reaching a minimum pressure of 160 kPa. The acceleration of gas within the inlet nozzle generates waves that cause the pressure and velocity at the static pressure gauge location to increase to maximum values of about 210 kPa and 224 m/s at the end of the data period shown. This corresponds to a Mach number of 0.67 and the beginning of the quasi-steady choked flow period at 0.15 s. Note that the peak (P, u) state corresponds very closely to the $Ma = 0.67$ state on the steady P-u curve.

The behavior for the entire flow transient (221 ms) is shown in Figure 36. The dense line of data points from 210 kPa down to 120 kPa with velocities between 224 and 200

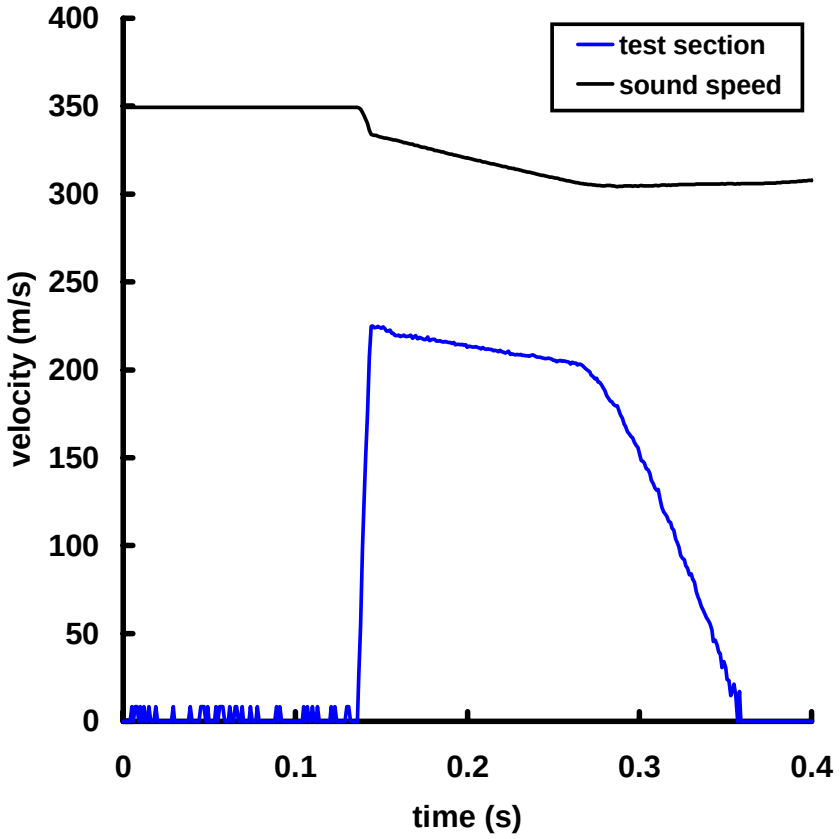

Figure 34: Sound speed and velocity in test section. Analyses of data in Shot 005.

m/s correspond to the quasi-steady choked flow period between 0.15 and 0.27 s. The horizontal line of data from 200 to 0 m/s and at 115–120 kPa pressure corresponds to the subsonic flow period between 0.27 and 0.36 s. The solid line is a model of the P-u relationship for a quasi-steady flow from a finite reservoir. This model is based on the observation that during the quasi-steady choked flow period, the Mach number Ma_3 in the test section is constant although the driver and receiver pressures are changing significantly.

If the Mach number in the test section is fixed, then Equation (17) implies that test section and driver temperatures are proportional during the quasi-steady period.

$$\frac{T_3(t)}{T_d(t)} = \frac{1}{1 + \frac{\gamma-1}{2} Ma_3^2} = \text{constant} \ . \tag{22}$$

Normalizing by the initial values $T_3(0)$ and $T_d(0)$ at the start of the quasi-steady period, we have

$$\frac{T_3(t)}{T_3(0)} = \frac{T_d(t)}{T_d(0)} \ . \tag{23}$$

Furthermore, since the flow is isentropic, a similar relationship for between the test section and driver pressure exists

$$\frac{P_3(t)}{P_d(t)} = \left(\frac{T_3(t)}{T_d(t)}\right)^{\frac{\gamma-1}{\gamma}} = \text{constant} \ , \tag{24}$$

which we can write as

$$\frac{P_3(t)}{P_3(0)} = \frac{P_d(t)}{P_d(0)} \ . \tag{25}$$

Applying the isentropic relationship between pressure and temperature inside the driver (Equation 16), we find that

$$T_3(t) = T_3(0)\left(\frac{P_3(t)}{P_3(0)}\right)^{\frac{\gamma-1}{\gamma}} \ . \tag{26}$$

Now consider computing the velocity from the known value of the Mach number and the definition of sound speed (Equation 21)

$$u = Ma_3\sqrt{\gamma R T_3(t)} = Ma_3 c_3(0)\left(\frac{P_3(t)}{P_3(0)}\right)^{\frac{\gamma-1}{2\gamma}} \ . \tag{27}$$

This is the result that is shown in Figure 36 and labeled as "Quasi-Steady Model". The only parameter needed is the Mach number which was obtained from the pitot-static analysis and is 0.67. The initial sound speed was computed from the measured temperature and the initial pressure was measured. The excellent agreement between the model and the measurements during the choked flow regime indicates that this notion can be used as the basis for a complete model, which we describe in Section 5.

4.2.2 Mass flow rate analysis

It is possible to calculate the mass flow rate from the rate-of-change of the driver pressure. Comparing this value to the mass flow rate expected from assuming ideal choked flow in the test section enables judging the duration of the choked flow regime and the computation of an effective flow area or orifice coefficient for an assumed flow area.

To determine the mass flow rate from the driver pressure history requires considering the conservation of mass and energy of the driver gas. This is developed in detail in the subsequent Section 5 on modeling. The conservation of mass in the driver reservoir can be expressed as

$$\frac{dM_d}{dt} = -\dot{m} \quad \text{where} \quad M_d = \rho_d V_d \tag{28}$$

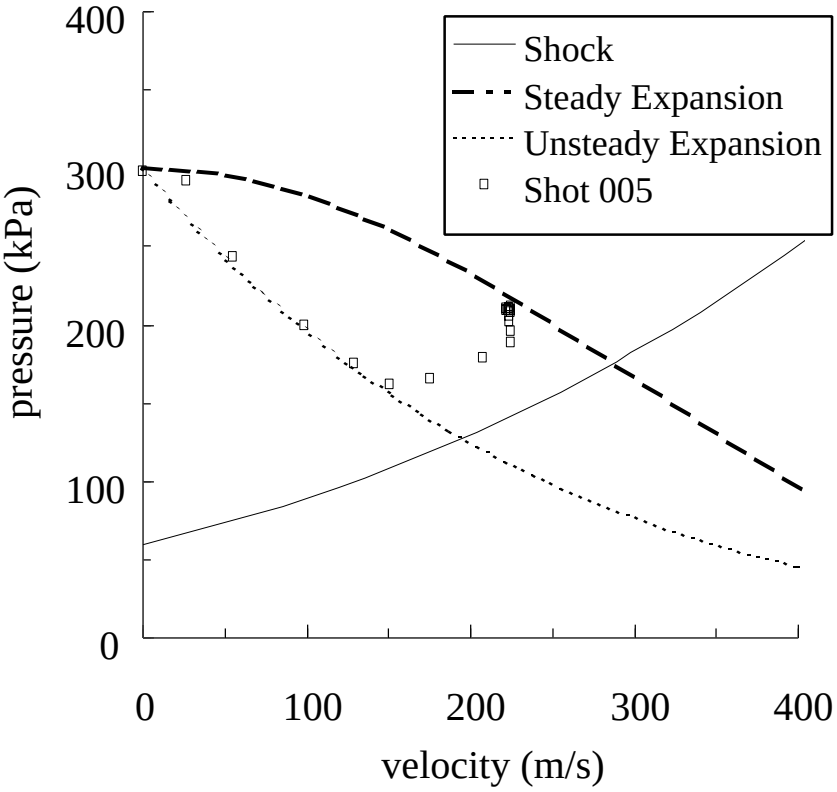

Figure 35: Comparison of Shot 005 early-time (first 19 ms) behavior with ideal P-u plot. Data illustrates transition from initial transient expansion wave to quasi-steady flow.

and $\dot{m}$ is the mass flow rate through the test section. The energy equation (53) for an adiabatic flow of a perfect gas can be expressed as

$$\frac{dP_d}{dt} = -\gamma \frac{\dot{m}}{M_d} P_d \, . \tag{29}$$

Combining the mass and energy equations to eliminate $\dot{m}$,

$$\frac{dM_d}{dt} = \frac{M_d}{\gamma} \frac{1}{P_d} \frac{dP_d}{dt} \, . \tag{30}$$

The mass of fluid in the driver can be related to the initial mass by integrating the above expression and solving for the constant of integration using the initial conditions $P_d(0)$ and $M_d(0)$. The result is

$$M_d\,(t) = M_d\,(0) \left(\frac{P_d\,(t)}{P_d\,(0)} \right)^{\frac{1}{\gamma}} \, . \tag{31}$$

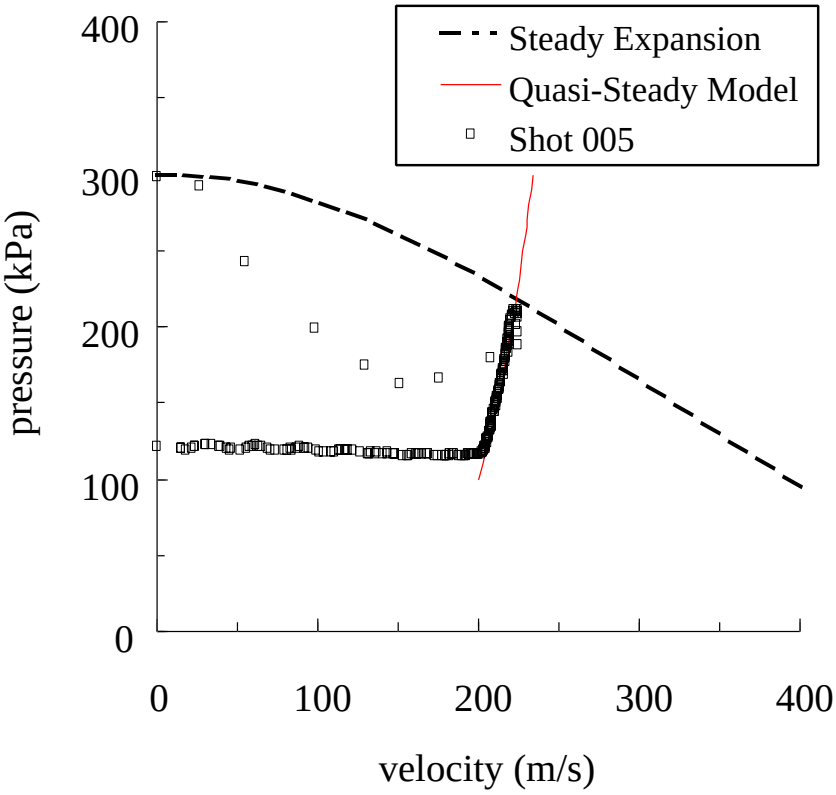

Figure 36: Comparison of Shot 005 long-time (221 ms) behavior with ideal P-u plot and simple quasi-steady model.

Thus, the mass flow rate out of the driver can be computed as

$$\dot{m} = -\frac{dM_d}{dt} = -\frac{M_d(0)}{\gamma}\left(\frac{P_d(t)}{P_d(0)}\right)^{\frac{1}{\gamma}}\frac{1}{P_d}\frac{dP_d}{dt} \tag{32}$$

Equation 32 enables the computation of the mass flow rate out of the driver vessel from experimentally measured properties such as the initial gas pressure and temperature, the volume of the vessel, and the time rate of change of the pressure in the driver vessel. The only difficulty is in the numerical differentiation of the measured pressure. Although the signals look smooth to the eye, attempting to use simple first differences to approximate the derivative results in an extremely noisy and unusable estimate. This is not unexpected since previous experience has shown that residual 60 Hz noise and digital quantization errors often make it difficult to directly differentiate raw data of this type. After filtering the data with a 5-point running average (trapezoidal weighting function), acceptable derivative estimates were obtained.

The Mach number plateau observed in the data analysis suggests that the flow is choked. To confirm this, we can compare the mass flow rate deduced from analyzing the driver pressure history to that predicted by assuming quasi-steady choked flow a perfect gas. The total property conditions are the supply reservoir conditions at a given point

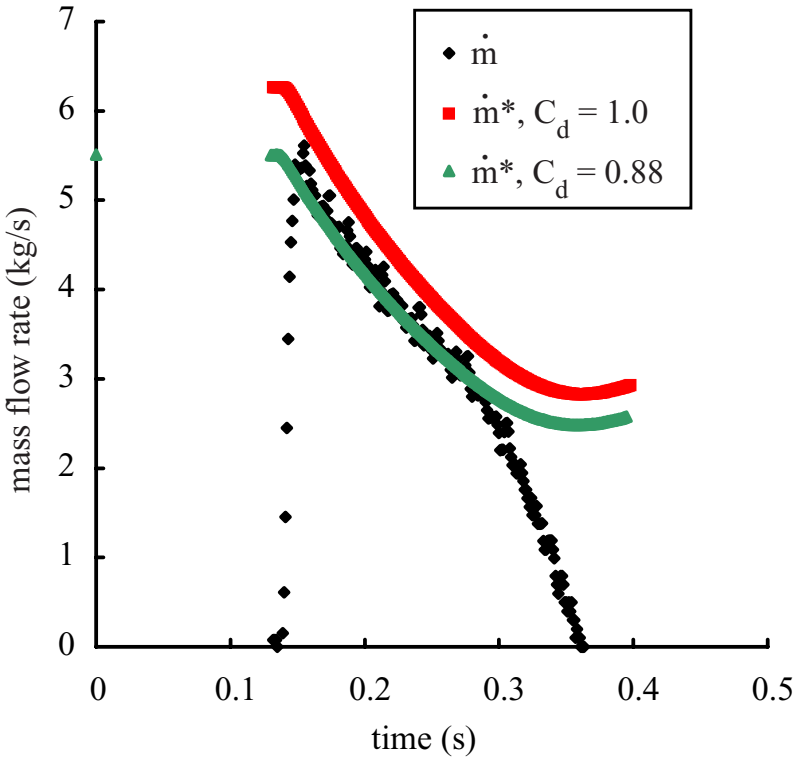

Figure 37: Mass flow rate inferred from analysis of pressure data for Shot 005 (no valve). The equivalent sonic flow area $A^* = 0.007923$ m^2 from the choked flow estimate. The actual minimum area at the pitot probe support was measured to be 0.00901 m^2, which leads to an orifice coefficient $C_d = 0.88$.

in time. This leads to

$$\dot{m}^* = \left(\frac{2}{\gamma+1}\right)^{\frac{1+\gamma}{2(\gamma-1)}} \rho_d(0)\, c_d(0)\, A^* \left(\frac{P_d}{P_d(0)}\right)^{\frac{\gamma+1}{2\gamma}} . \tag{33}$$

Note that equation 33 relates the mass flow for choked flow to initial conditions and experimentally measured quantities. The only unknown parameter is the area A^* which is the effective minimum area (throat) and can be related to the physical area of the test section by a discharge coefficient such that $A^* = C_d A_{physical}$. The discharge coefficient can be then be found from experimental data. Figure 37 compares $\dot{m}$ and $\dot{m}^*$ for different values of C_d using data from Shot 005.

When the flow is choked, $\dot{m}$ agrees with $\dot{m}^*$ as was assumed in the above analysis. When choking ceases, $\dot{m}$ and $\dot{m}^*$ are no longer comparable. It can be seen from Figure 37 that the choking period corresponds to the Mach number plateau in the test section (Figure 59). For a given initial driver pressure, decreasing the receiver pressure will extend the period of choked flow as is shown in Figure 38.

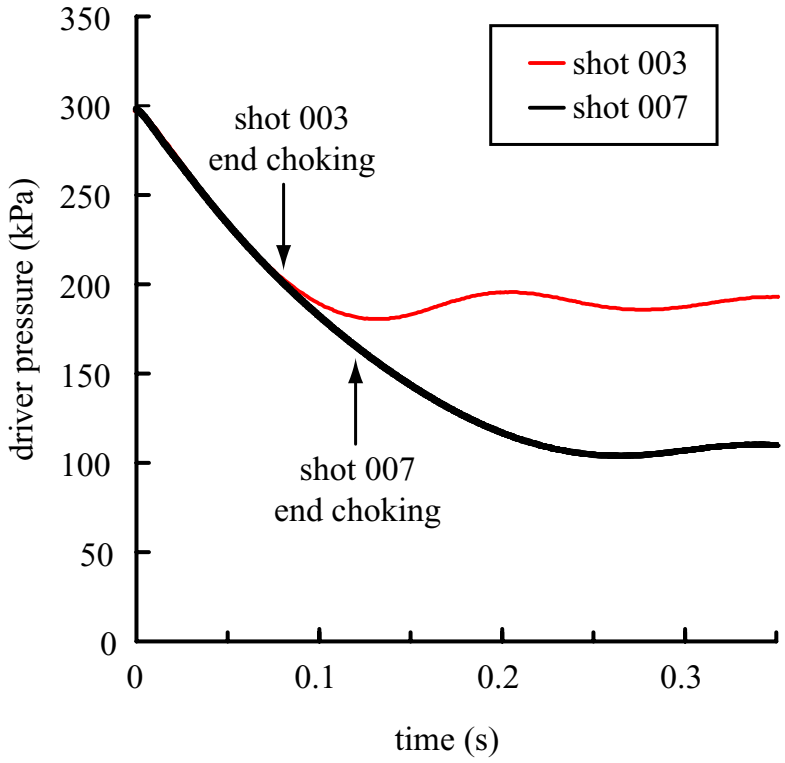

Figure 38: Driver pressure data from tests with identical initial driver pressures and different receiver pressures. This demonstrates how lower receiver pressures result in a longer duration of choked flow. For shot 003, $P_r(0) = 150$ kPa. For shot 007, $P_r(0) = 37$ kPa. For both, $P_d(0)$ was 300 kPa. Arrows indicate where choking ceases.

4.3 Valve Installed

For testing with the valve–injector unit installed, the pressure transducer arrangement was identical to Figure 30. A typical set of pressure traces and corresponding velocity, density and temperature are shown in Figure 67. The basic features of the pressure traces are qualitatively similar to those of the cases without a valve body. There is an initial transient lasting a few ms that is associated with starting the flow. This is followed by a constant Mach number regime of about 0.15 s during which the flow is apparently choked at the valve body. The flow at the pitot probe location is subsonic for the entire duration of the test. Following the end of the constant Mach number regime, the flow velocity decreases to zero over a period of about 0.2 s as the driver and receiver pressures equilibrate. Despite the similarities, the quantitative details are different due to stagnation pressure losses associated with the flow through the valve.

The presence of the valve upstream of the flow results in a significant decrease in stagnation pressure between the driver and the test section as compared to tests with no valve installed. In a typical test, the stagnation pressure in the test section during the

choked flow period is about 75% of the stagnation pressure in the driver. All data from tests with the valve body installed is shown in Appendix D.

The valve body lowers the mass flow rate and changes the history of the test section density compared to tests without the valve body installed. Where there was no valve body blockage, the test section density (Figure 63 of Appendix D) decreased steadily as a function of the driver pressure. With the valve body restricting the flow and lowering the stagnation pressure, the test section density no longer decreases steadily with driver pressure, instead decreasing to a minimum value during the quasi–steady flow and then increasing as the flow slows down. The velocities remain similar resulting in a slower mass flow rate but longer blowdown time for tests with the valve body installed. The velocity profile is also not as smooth for tests with the valve body installed due to disturbances generated by flow through the valve.

4.3.1 Stagnation pressure losses

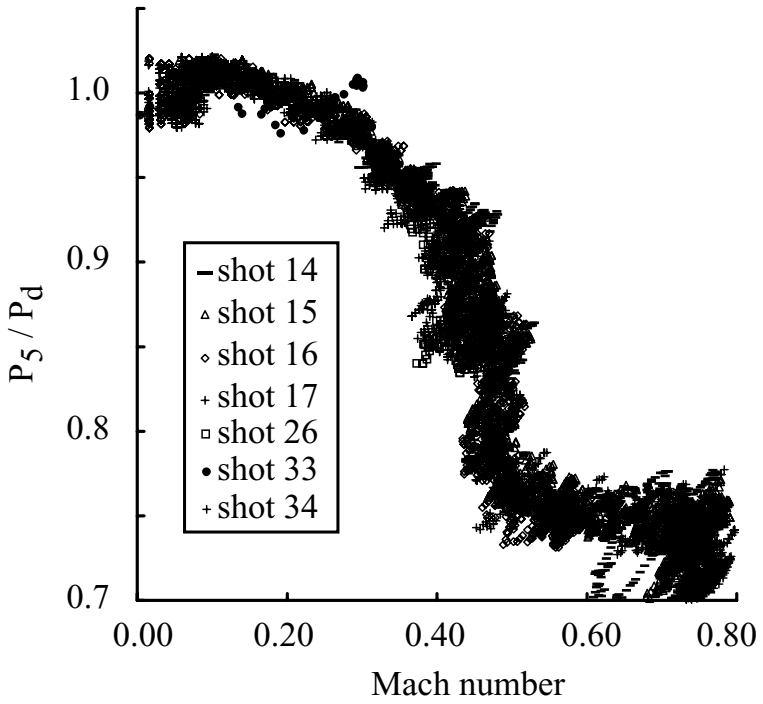

Figure 39: The ratio of test section pitot pressure to driver pressure versus test section Mach number is shown for some tests with the valve body installed.

Figure 39 shows the ratio of the stagnation pressure measured in the test section to the stagnation pressure measured in the driver as a function of test section Mach number. The test section Mach number is computed from equation 15 using the measured static and pitot pressures. For tests without the valve, stagnation pressure losses between the driver and test section pitot probe were minimal. This is shown in Figure 40 for Shot 005.

As shown, the stagnation pressure differences between driver and pitot probe location are less 5%. Interestingly, the stagnation pressure in the driver appears to be slightly lower (1-4%) than in the test section for the unchoked portion of the flow. At this time, it is not clear what the explanation is for this effect. Therefore, the losses shown in figure 39

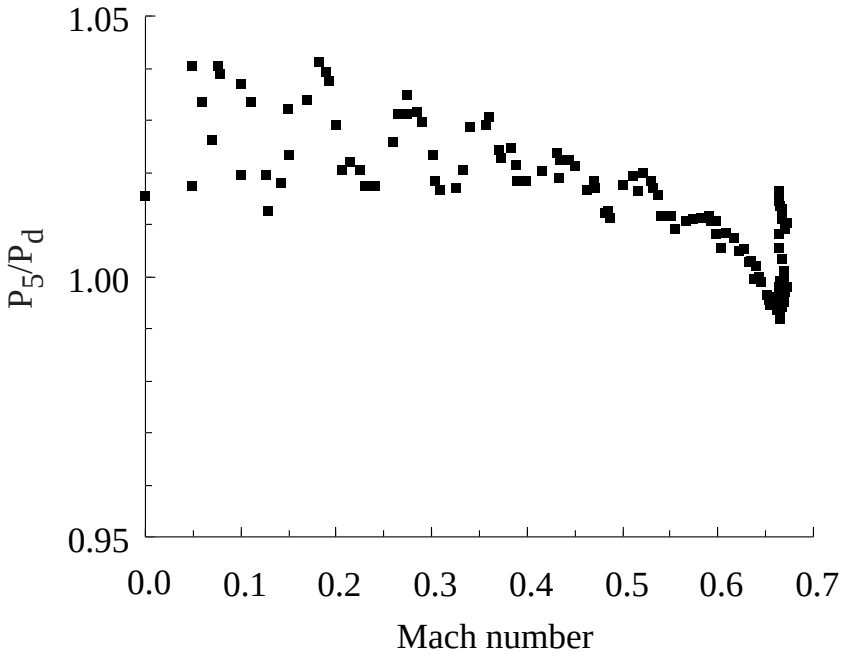

Figure 40: The ratio of test section pitot pressure to driver pressure versus test section Mach number is shown for one test (Shot 005) without a valve body installed. Note the difference in vertical scale as compared with Figure 39.

are due to flow separation, shock waves, and other loss mechanisms created by the flow through the valve.

The plot identifies two regimes of pressure loss in the experiment. The first occurs over test section Mach numbers 0–0.4 and is evidenced by a gradual decrease in stagnation pressure loss with increasing test section Mach number. The losses in this regime are attributed to separated flow associated with the valve. The second regime is from 0.4–0.8, where the pressure losses rapidly increase at Mach number 0.4 and then remain relatively constant at a value of 0.75 as Mach number increases. We speculate that losses in this regime are due to both separated flow and possibly, shock waves. The sudden drop in test section stagnation pressure at Mach number 0.4 suggests a change in mechanism of losses which may be associated with the onset of supersonic flow due to the area change in the valve.

With the valve body installed, location of the minimum cross–sectional area in the experiment is inside the valve. At this location, the cross–sectional area is 58% that of the cross-sectional area of the test section. Thus, for sufficiently high driver pressures, the flow chokes inside the valve. As is discussed in Section 5.1, the area A^* at the sonic point has a definite relationship to the cross-sectional area and Mach number at any other

location location (Equation 11). This relationship predicts that isentropically expanding the flow from a sonic state to a test section Mach number of 0.4 requires an area at the sonic point that is 62% of the test section area. This is within 6% of the actual physical area ratio, which is reasonable given that the actual flow is far from one-dimensional or steady. We conclude that the flow is choked within the valve for test section Mach numbers greater than 0.4. This is confirmed by comparison of inferred mass flow rates with choked flow in Figure 43.

Downstream of the valve throat, the cross-sectional area increases rapidly to the test section area. The potential exists for the flow to over-expand, becoming supersonic and at a lower pressure than the mean flow downstream. In this case, flow will have to be compressed through a system of shock waves downstream of the valve body. The actual flow field is quite complex (see Figure 42) and unsteady but an indication of the magnitude of the total pressure loss can be obtained by considering the effect of a single steady, normal shock wave. The ratio of stagnation pressure upstream and downstream of a normal shock is given by

$$\frac{P_{t,2}}{P_{t,2}} = \left[\frac{(\gamma+1)\,M_s^2}{2+(\gamma-1)\,M_s^2}\right]^{\gamma/(\gamma-1)} \left[\frac{\gamma+1}{2\gamma M_s^2-(\gamma-1)}\right]^{1/(\gamma-1)} \tag{34}$$

where $P_{t,1}$ is the stagnation pressure upstream of the shock, $P_{t,2}$ is the downstream stagnation pressure and M_s is the Mach number of the incoming flow in a shock–fixed coordinate system. The ratio of stagnation pressures across a shock is shown in Figure 41 for a range of values of M_s. For a shock with incoming flow at Mach number of 1.93, stagnation losses $(P_{t,1}-P_{t,2})/P_{t,1} = 24.7\%$ are predicted, which is close to what is observed for test section Mach numbers greater than 0.5 in Figure 39. It should also be noted that expanding sonic flow to a Mach number of 1.93 requires an area ratio $A^*/A = 0.63$, comparable to the physical area ratio of 0.58 for the valve body. Inspection of the shock wave tables reveals that for a Mach 1.93 shock velocity, an average downstream Mach number of about 0.59 is expected in the test section. Observed test section Mach numbers in the choking regime range from 0.55–0.78 for testing with the valve installed, with the majority of values close to 0.75 which corresponds to a shock Mach number of 1.4.

Flow separation and total pressure loss associated with shock waves were anticipated from the design study. Numerical simulations (Figure 42) predicted the presence of supersonic flow near the exit of the the valve and also show separated flow. As discussed in the modeling section, the simulation is inviscid and extent and location of the separated flow regions may not be accurately predicted.

4.3.2 Mass flow rate

Assuming choking occurs at the valve upstream of the test section, it is possible to repeat the mass flow rate analysis described in Section 4.2 for the experimental configuration with the valve body installed. Figure 43 illustrates the choking regime. Note that the initial pressures in Figures 37 and 43 are similar, however the throat A^* in tests with the valve installed is 68% of the throat in tests with no valve installed. Thus it is expected

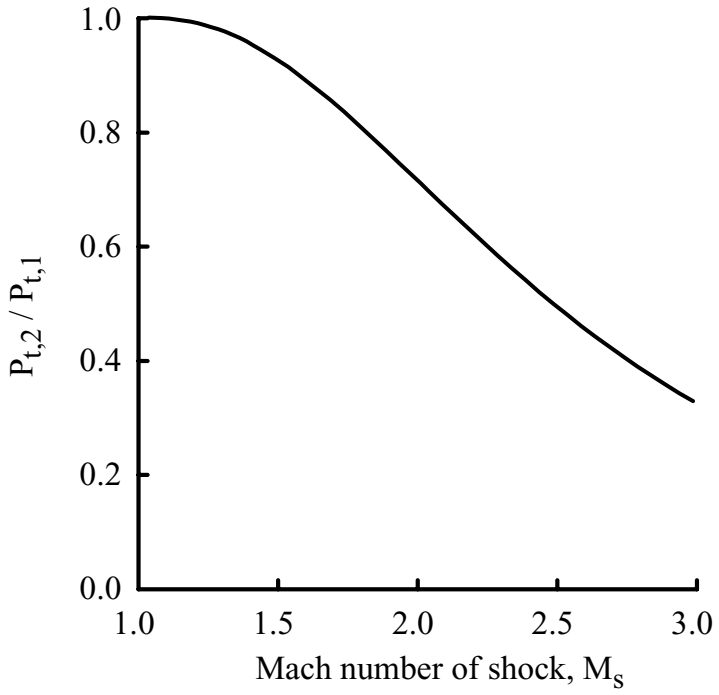

Figure 41: Stagnation pressure ratio, $P_{t,2}/P_{t,1}$, across a shock versus shock Mach number for $\gamma = 1.4$.

Figure 42: Close–up of the numerical schlieren for frame 399, simulation pr3xd320. Thin white lines are contours of sonic surfaces. Both shock waves and the mixing of high and low-speed fluid in the wakes will lead to stagnation pressure losses. Flow is from the left to the right and initial pressure ratio is 3.

that the mass flow rate will be lower for tests with the valve body installed, which should lead to longer choking times compared to tests without the valve. This is not the case. While the lower cross–section of the valve does indeed decrease the mass flow rate, the pressure losses result in lower test section pressures. As previously discussed,

choking is observed to end when the pressure at the sonic throat is equal to the receiver pressure. This occurs at a higher driver to receiver pressure ratio P_d/P_r in the tests with the valve body than the tests without the valve body due to the pressure losses previously discussed. Thus, the choking period in both experiment configurations is of similar duration.

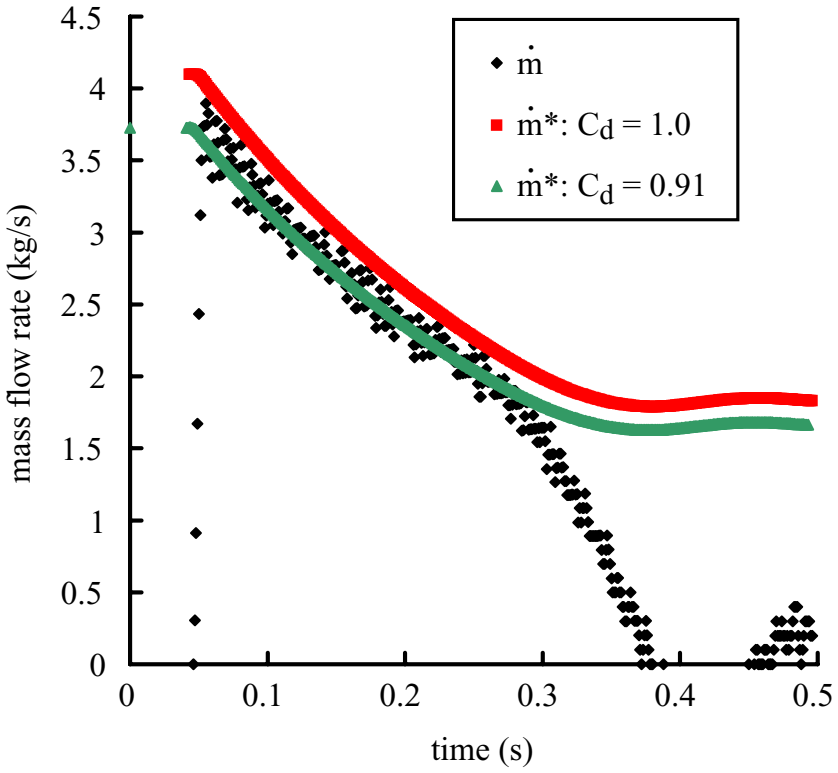

Figure 43: Comparison of $\dot{m}$ and $\dot{m}^*$ for different values of C_d for Shot 015 (valve installed, 300 kPa initial driver pressure, 50 kPa initial receiver pressure). An area of $A^* = 0.005362$ m^2 was inferred from the data. $A_{physical}$ was measured to be 0.005893 m^2.

4.4 Valve Actuation During Testing

The pressure transducer arrangement shown in Figure 30 was used to measure flow velocity during tests with valve actuation. A typical set of pressure traces and corresponding velocity, density and temperature are shown in Figure 88 of Appendix E.

Before valve closure, the data is the same as cases without valve closure. When the valve closes at 135 ms, an expansion wave propagates though the test section bringing the flow to a halt. Note that the pressure of the driver is higher than the pressure of the test section, as is expected.

Depending on the flow velocity and pressure, the valve may not abruptly close and remain closed. Under higher pressures or flow velocities, a stronger expansion wave was

generated upon valve closure. The valve was observed to "bounce" open and closed several times before remaining closed as is shown the data in Figure 80 of Appendix E.

The amount of bounce observed was dependent on the pressure ratio across the valve body, the initial driver pressure, the valve body piston pressure and the valve body venting speed. During valve body actuation testing, these parameters were varied to achieve the most crisp valve closure possible and minimize the valve body bounce while maintaining suitable test section conditions. The optimum test conditions (Figure 88 of Appendix E) were found with a driver pressure of 120 kPa and a receiver pressure of 70 kPa. Under these conditions, it was possible to completely stop the flow in the test section over a period of 5 ms.

5 Model for tests without the valve

A simple analytical model based on control volume ideas was developed to predict the duration and magnitude of the constant Mach number plateau observed in tests without the valve installed. The model assumes that the flow is sonic at the minimum area in the flow path and treats the experiment as a quasi–steady blowdown process. The gases within the driver and receiver are treated as uniformly mixed with a single temperature and pressure. The flow is considered to be adiabatic and losses due to flow separation in the inlet are not treated. The only adjustable parameter in the model is an orifice coefficient, which has a fixed value for any given experiment.

Relevant areas in the flow path are shown in Figure 44. The minimum area for this configuration is at the pitot gauge support. The area A^* at this location is appears to be the minimum area in the flow and the point at which choked flow will occur.

5.1 Mach number at the pitot pressure gauge

Assuming that the flow between the pitot probe and the driver reservoir can be approximated as an isentropic process of a perfect gas, the continuity equation can be represented as a Mach number–area relationship shown in Equation 11. The Mach number of the flow at the head of the pitot gauge can be predicted to be 0.66 by using this relation with $\gamma = 1.4$, $A = 0.01016$ m^2, and $A^* = 0.00901$. The experimental values of the Mach number at the pitot probe in the test section range from 0.65–0.68 as shown in the plots in Appendix C.

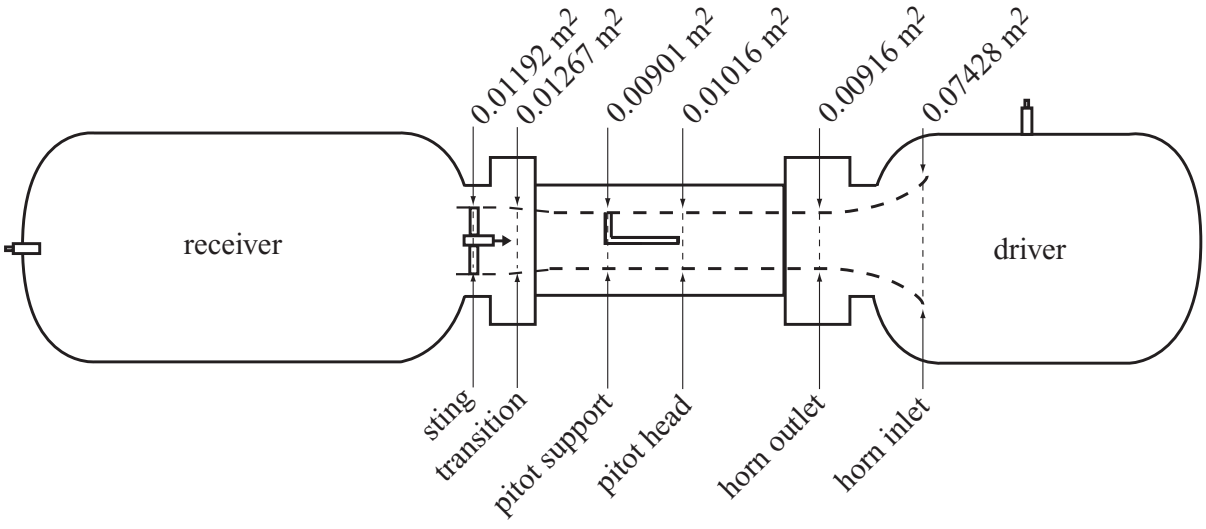

Figure 44: Cross–sectional flow areas in the experiment during testing with no valve blockage.

5.2 Blowdown analysis

Driver conditions

The driver blowdown process can be approximated as isentropic blowdown of a perfect gas through a sonic orifice. If the time required for fluid to move from the interior of the driver vessel to the test section is small compared to the duration of the test, the process can be assumed to be quasi–steady. With this assumption and the condition that the flow is adiabatic, the control volume versions of mass and energy conservation can be used to predict the conditions in the driver during choked flow in the test section. The

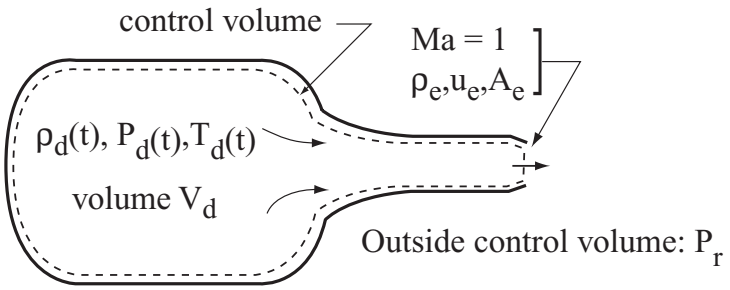

Figure 45: The control volume used for analyzing the driver blow down.

generic mass conservation equation is

$$\frac{d}{dt}\int_V \rho\, dV + \int_{\partial V} \rho\,(\mathbf{u}\cdot\mathbf{n})\, dA = 0\ . \tag{35}$$

Applying this to the control volume shown in Figure 45, we obtain

$$\frac{d}{dt}\left(\rho_d V_d\right) = -\rho_e u_e A_e = -\dot{m}_e \tag{36}$$

where ρ_e, u_e, and A_e are the density, velocity and orifice area at the exit respectively. It is assumed that the properties of the fluid inside the driver are spatially homogeneous, as are the fluid properties at the orifice. The rate of mass flow out of the orifice is $\dot{m}_e$. The flow at the orifice will be choked while

$$\frac{P_d}{P_r} \geq \left(\frac{\gamma+1}{2}\right)^{\frac{\gamma}{\gamma-1}} \tag{37}$$

where P_r is the receiver pressure. When this is satisfied, the mass flow will be given by

$$\dot{m}_e = \dot{m}_e^* = \rho^*\, c^*\, A^*\ . \tag{38}$$

where the $(\ )^*$ state indicates the conditions for sonic ($M = 1$) flow.

While the orifice is choked, the mass flow out of the driver is purely dependent on the driver density and temperature. For quasi-steady, adiabatic flow from the interior of the vessel to the orifice, we have

$$h_d(t) = h_e(t) + \frac{u_e^2(t)}{2} \; . \tag{39}$$

where $h_d(t)$ is the enthalpy of the driver fluid and $h_e(t)$ is the enthalpy of the fluid at the orifice. For a perfect gas (constant specific heat), the enthalpy is $h = C_p T$ and this can be written

$$\frac{T_d}{T_e} = \left(1 + \frac{u_e^2}{2\, C_p T_e}\right) = \left(1 + \frac{\gamma - 1)}{2} M_e^2\right) \tag{40}$$

using

$$C_p = \frac{\gamma R}{\gamma - 1} \; . \tag{41}$$

For choked flow $M_e = 1$ and $T_e = T^*$ so that

$$T^* = T_d \left(\frac{2}{\gamma + 1}\right) \; . \tag{42}$$

For isentropic flow

$$\frac{\rho^*}{\rho_d} = \left(\frac{T^*}{T_d}\right)^{\frac{1}{\gamma - 1}} = \left(\frac{2}{\gamma + 1}\right)^{\frac{\gamma}{\gamma - 1}} \; . \tag{43}$$

The speed of sound at the throat is

$$c^* = \sqrt{\gamma R T^*} \; . \tag{44}$$

Thus the mass flow rate through a choked orifice will be

$$\dot{m}^* = \sqrt{\gamma} \left(\frac{2}{\gamma + 1}\right)^{\frac{\gamma + 1}{2(\gamma - 1)}} A^* \rho_d \sqrt{R T_d} \tag{45}$$

where the driver conditions are a function of time. The time rate of change of driver density can be determined by equation 36, noting that the volume of the driver is constant so that we have

$$\frac{d\rho_d}{dt} = -\frac{\dot{m}^*}{V_d} \; . \tag{46}$$

In order to integrate this equation we need to determine how the driver temperature varies with time. This can be found by considering the energy balance for the control volume. The general energy balance relation is

$$\frac{d}{dt}\int_V \rho\left(e+\frac{u^2}{2}\right)dV+\int_{\partial V}\rho\left(h+\frac{u^2}{2}\right)(\mathbf{u}\cdot\mathbf{n})\,dA=\dot{Q}+\dot{W} \tag{47}$$

where e is the internal energy, h is the enthalpy, $\dot{Q}$ is the heat addition, and $\dot{W}$ is the external work done on the system. Applying the energy equation to the control volume in Figure 45 assuming there is no heat addition (adiabatic) or external work yields

$$\dot{Q}=\dot{W}=0\,. \tag{48}$$

Further assuming that the velocity of gas inside the driver can be approximated as zero and the driver is spatially homogeneous reduces the energy equation to

$$\frac{d}{dt}\int_V \rho\, e\, dV=-\int_{\partial V}\rho\left(h+\frac{u^2}{2}\right)(\mathbf{u}\cdot\mathbf{n})\,dA\,. \tag{49}$$

Assuming uniform conditions at the exit,

$$\frac{d}{dt}\left(\rho_d\, e_d\, V_d\right)+\rho_e\left(h_e+\frac{u_e^2}{2}\right)u_e\, A_e=0 \tag{50}$$

For adiabatic, quasi-static flow between the driver and the orifice, the total enthalpy is constant

$$h_d=h_e+u_e^2/2 \tag{51}$$

and assuming perfect gas behavior, the energy balance equation reduces to

$$\frac{d}{dt}\left(\rho_d\, T_d\right)=-\gamma\frac{\dot{m}\, T_d}{V_d} \tag{52}$$

Where $\gamma=C_p/C_v$. For choked flow, we can further simplify this as

$$\frac{d}{dt}\left(\rho_d\, T_d\right)=-\frac{\gamma\, T_d\,\dot{m}^*}{V_d}\,. \tag{53}$$

The mass (46) and energy (53) equations form two coupled first-order ordinary differential equations for the variables ρ_d and T_d. The driver density ρ_d can be eliminated from equation 53. First, the chain rule is used to separate ρ_d and T_d in the first term of equation 53

$$\frac{d\rho_d}{dt}\,T_d+\rho_d\,\frac{dT_d}{dt}=-\frac{\gamma\, T_d\,\dot{m}^*}{V_d}\,. \tag{54}$$

Equation 46 can then be used to eliminate $d\rho_d/dt$

$$\left(\frac{-\dot{m}^*}{V_d}\right) T_d + \rho_d \frac{dT_d}{dt} = -\frac{\gamma\, T_d\, \dot{m}^*}{V_d} \ . \tag{55}$$

Simplifying and using equation 45, we get a single differential equation for driver temperature

$$\frac{dT_d}{dt} = -C_1 T_d^{\frac{3}{2}} \tag{56}$$

where

$$C_1 = \sqrt{\gamma}\left(\frac{2}{\gamma+1}\right)^{\frac{\gamma+1}{2(\gamma-1)}} \frac{A^*}{V_d}\sqrt{R}\,(\gamma-1) \ . \tag{57}$$

Integration yields

$$T_d = T_d(0)\left[1 + \frac{t}{2\tau}\right]^{-2} \tag{58}$$

where τ is the characteristic time for blowdown

$$\tau = \frac{1}{C_1\sqrt{T_d(0)}} \tag{59}$$

and can be interpreted as the transit time through a cylinder of length $L = V/A^*$ at the initial sound speed $c_0(0)$. Numerical values of τ range from 0.64 s (for the configuration with no valve installed) to 0.94 s (for the configuration with the valve installed).

The driver pressure P_d can then be found using the isentropic relation

$$P_d\,(t) = P_d\,(0)\left(\frac{T_d\,(t)}{T_d\,(0)}\right)^{\frac{\gamma}{\gamma-1}} \tag{60}$$

Equations 58 and 60 predict the driver conditions as a function of time. It is important to note that in practice the physical cross–sectional area at the throat, $A_{physical}$, must be multiplied by an discharge coefficient, C_d, which is dependent on the channel geometry and flow conditions. This coefficient transforms the physical area into the effective area that the flow perceives. Thus,

$$A^* = C_d\, A_{physical} \ . \tag{61}$$

The predicted pressure and temperature of the driver are plotted with the experimental values for Shot 005 in Figures 46 and 47. The model agrees well with the data up until the receiver pressure equals the test section static pressure which corresponds to the time that choking ceases in the test section.

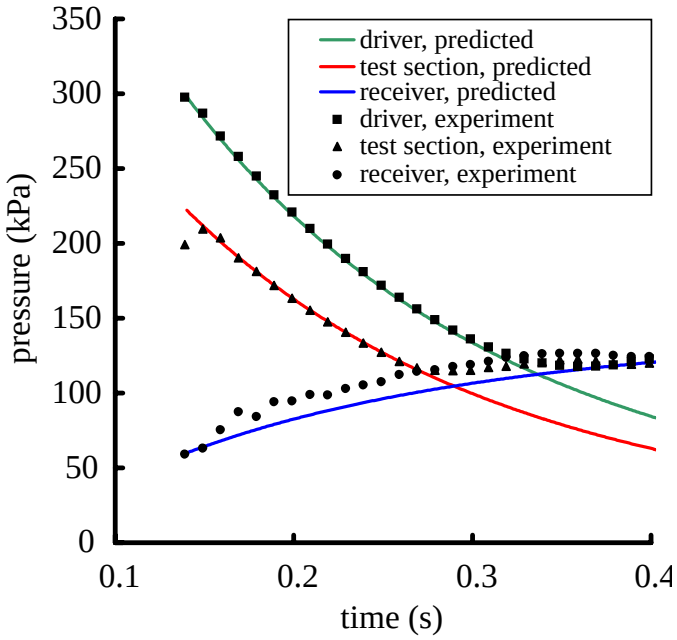

Figure 46: Predicted pressure versus experimental pressure data for Shot 005. $P_d(0) = 300$ kPa, $P_r(0) = 60$ kPa, $T_d = 304$ K, $T_r = 300$ K, $C_d = 0.75$.

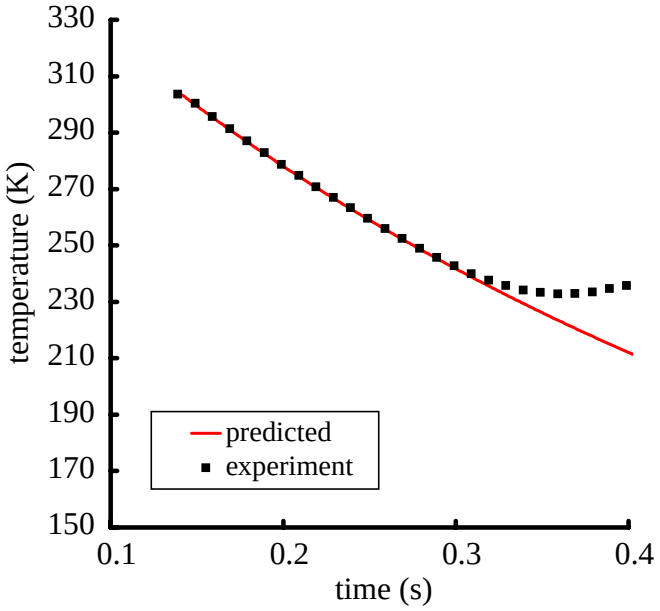

Figure 47: Predicted temperature versus temperature inferred from the experimental data for Shot 005. $P_d(0) = 300$ kPa, $P_r(0) = 60$ kPa, $T_d = 304$ K, $T_r = 300$ K, $C_d = 0.75$.

Receiver conditions

During the experiment, fluid leaving the driver is accelerated into the test section and is brought to rest in the receiver reservoir. Using the mass and total enthalpy fluxes predicted by the driver model, it should be possible to predict the receiver conditions. In this section the mass conservation and energy equations are used to estimate the pressure of the receiver for the period that the test section is choked. The development of the equations is similar to the driver analysis performed in the previous section.

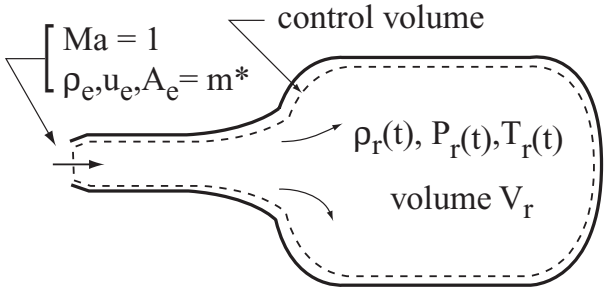

Figure 48: Control volume for the receiver.

The receiver vessel is represented as the control volume shown in Figure 48. The receiver is of constant volume V_r and is filled with a fluid with pressure P_r, temperature T_r, and density ρ_r. There is also a mass flux $\dot{m}_e = \dot{m}^*$ into the receiver which is equal to the choked flow mass flux leaving the driver. The mass flows through an orifice with effective area A_e.

Applying the mass equation (Equation 35) to the receiver control volume yields

$$\frac{d\rho_r}{dt} = \frac{\dot{m}^*}{V_r} \; . \tag{62}$$

This can be integrated, noting that $\dot{m}^*$ varies with time

$$\rho_r = \frac{1}{V_r} \int_0^t \dot{m}^* \left(t'\right) dt' \; . \tag{63}$$

For adiabatic flow, the energy equation (Equation 47) applied to the control volume is

$$\frac{d}{dt} \left(\rho_r \, e_r \, V_r\right) = \dot{m}^* \, h_d \; . \tag{64}$$

For a perfect gas this reduces to

$$\frac{d}{dt} \left(\rho_r \, T_r\right) = \gamma \frac{\dot{m}^* \, T_d}{V_r} \; . \tag{65}$$

Using the chain rule to separate ρ_r and T_r in the derivative

$$\rho_r \frac{dT_r}{dt} + \frac{d\rho_r}{dt} T_r = \gamma \frac{\dot{m}^* T_d}{V_r} \tag{66}$$

results in a first-order linear equation with time-dependent coefficients

$$\frac{dT_r(t)}{dt} + f(t)\, T_r(t) = g(t) \ . \tag{67}$$

The coefficients are

$$f(t) = \frac{1}{\rho_r} \frac{d\rho_r}{dt} \tag{68}$$

and

$$g(t) = \gamma \frac{\dot{m}^* T_d}{V_r \rho_r} \ . \tag{69}$$

The solution is

$$T_r = \frac{\int \mu(t)\, g(t)\ dt + T_r(0)}{\mu(t)} \tag{70}$$

where we have used the integrating factor

$$\mu(t) = \exp \int f(t)\ dt \tag{71}$$

With ρ_r and T_r known, the receiver pressure P_r can be found from the ideal gas law

$$P_r = \rho_r R\, T_r \tag{72}$$

where R is the gas constant.

Thus, equations 62, 63 and 68–72 can be used to predict the conditions in the receiver assuming a choked test section with adiabatic flow of a perfect gas. The predicted pressure (Equation 72) is plotted against experimental data from Shot 005 in Figure 46. Deviations between the predicted and experimental receiver pressure are on the order of 20%. Possible sources of this deviation include heat transfer and imperfect mixing within the receiver.

6 Conclusions

The facility was successfully constructed and is capable of producing a constant test section Mach number of about 0.7 for a period of about 0.15 seconds. During constant Mach number operation, the flow was found to be choked in the test section. While choked, the Mach number in the test section is purely dependent on the isentropic Mach number–area relationship. The period of choking was found to be dependent on the initial receiver pressure for a given initial driver pressure. Decreasing the receiver pressure was found to increase the period of choking. For testing without a valve upstream of the test section, a simple blowdown model was able to accurately predict the test section Mach number and period of choking.

Inclusion of the valve creates a sonic throat upstream of the test section. For test section Mach numbers in excess of 0.5, it was demonstrated that significant losses in stagnation pressure were incurred as the flow passed through the valve body. These losses are attributed to the presence of shocks at the exit of the valve body contraction.

The valve body throat has a smaller cross–sectional flow area than the test section throat. As a result, testing with the valve body resulted in lower mass flow rates during choking than were obtained in tests without the valve body. The lower mass flow rate did not result in an extended choking period due to the additional stagnation pressure losses. However, lower flow densities and higher Mach numbers were observed in the test section with the valve body due to the smaller throat. Actuation of the valve was successful in bringing the flow to a stop within the test section. The valve was able to stop the flow in the test section abruptly over a period of about 5 ms.

Acknowledgments

This work was carried out under P.O. No. 00-592 for Advanced Projects Research, Inc. under AF contract F04611-99-C-0017. Contract administration, mechanical design, and fabrication of the major components of the facility including the test section, test section and driver supports, transition section, inlet nozzle and coupling to the driver tank, were carried out by Advanced Projects Research, Inc. Key participants from APRI included Toby Rossmann, Jay Marsh, Keith Robinson, Kevin Moore, and Tom Sobota.

Toby Rossmann was the on-site representative who shouldered the primary responsibility for day-to-day interactions between our organizations and he worked together with Scott Jackson to finalize the assembly and carry out the tests.

Hans Hornung carried out the numerical simulations with Amrita that are shown in Chapter 2.2 and we thank him for his willingness to undertake this task without remuneration.

References

[1] Quirk, J., "AMRITA - A Computational Facility (for CFD Modelling)," VKI 29th CFD Lecture Series, ISSN 0377-8312, 1998.

[2] Krok, C., *Jet Initiation of Deflagration and Detonation*, Ph.D. thesis, California Institute of Technology, Aeronautics, May 1987.

A Layout of Laboratory Area

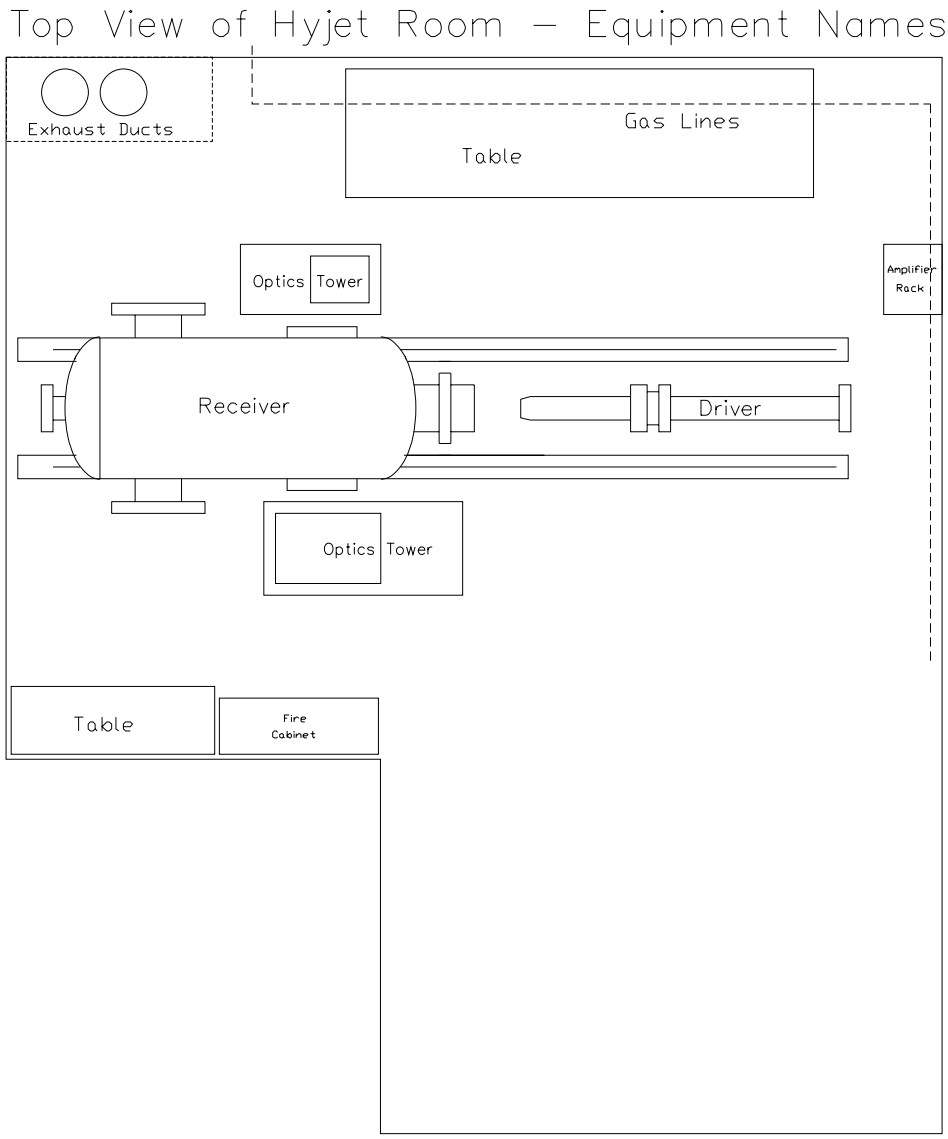

Figure 49: Component identification on plan view of layout of Explosion Dynamics Laboratory test area before modification.

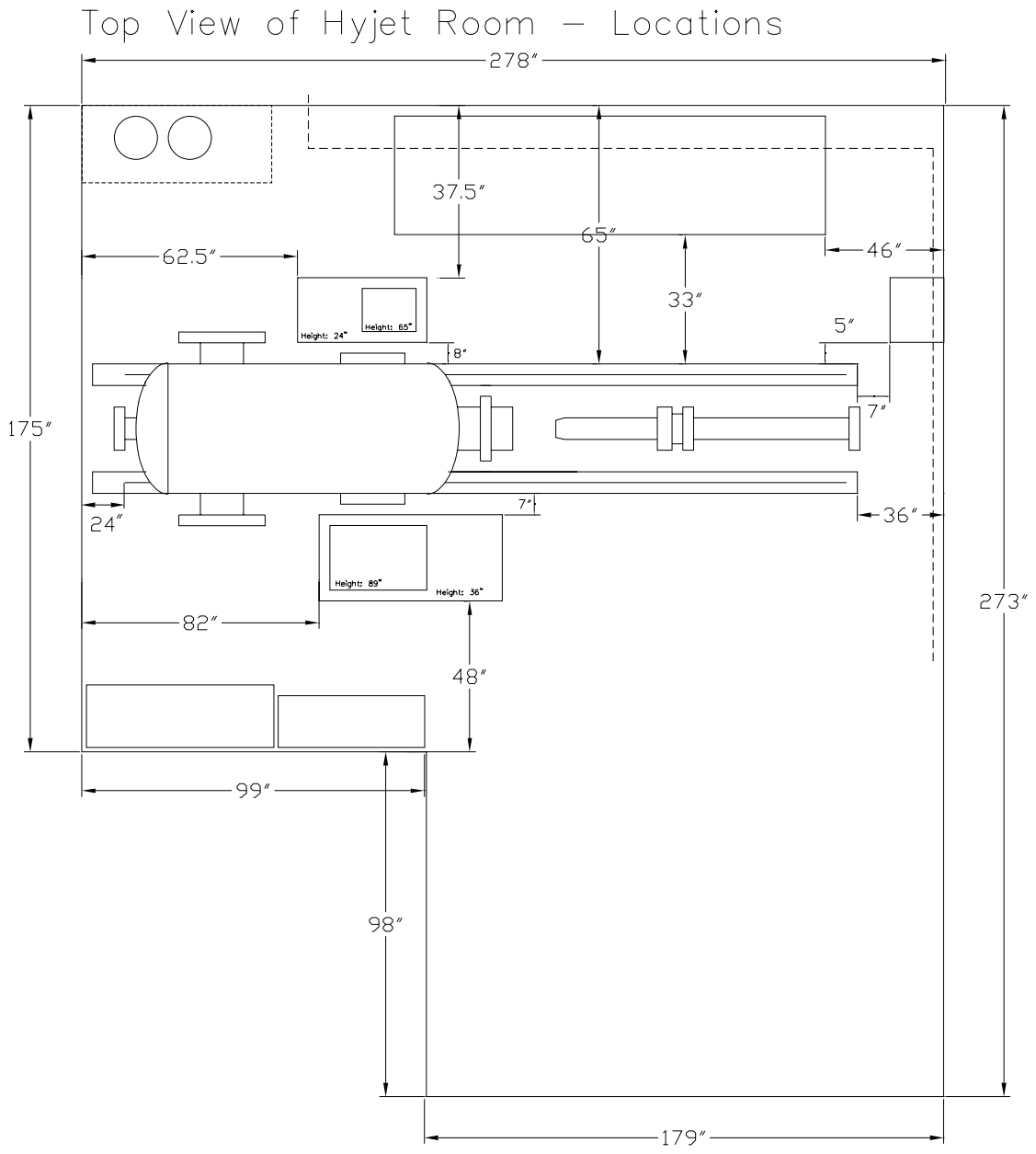

Figure 50: Dimensions on plan view of layout of Explosion Dynamics Laboratory test area before modification.

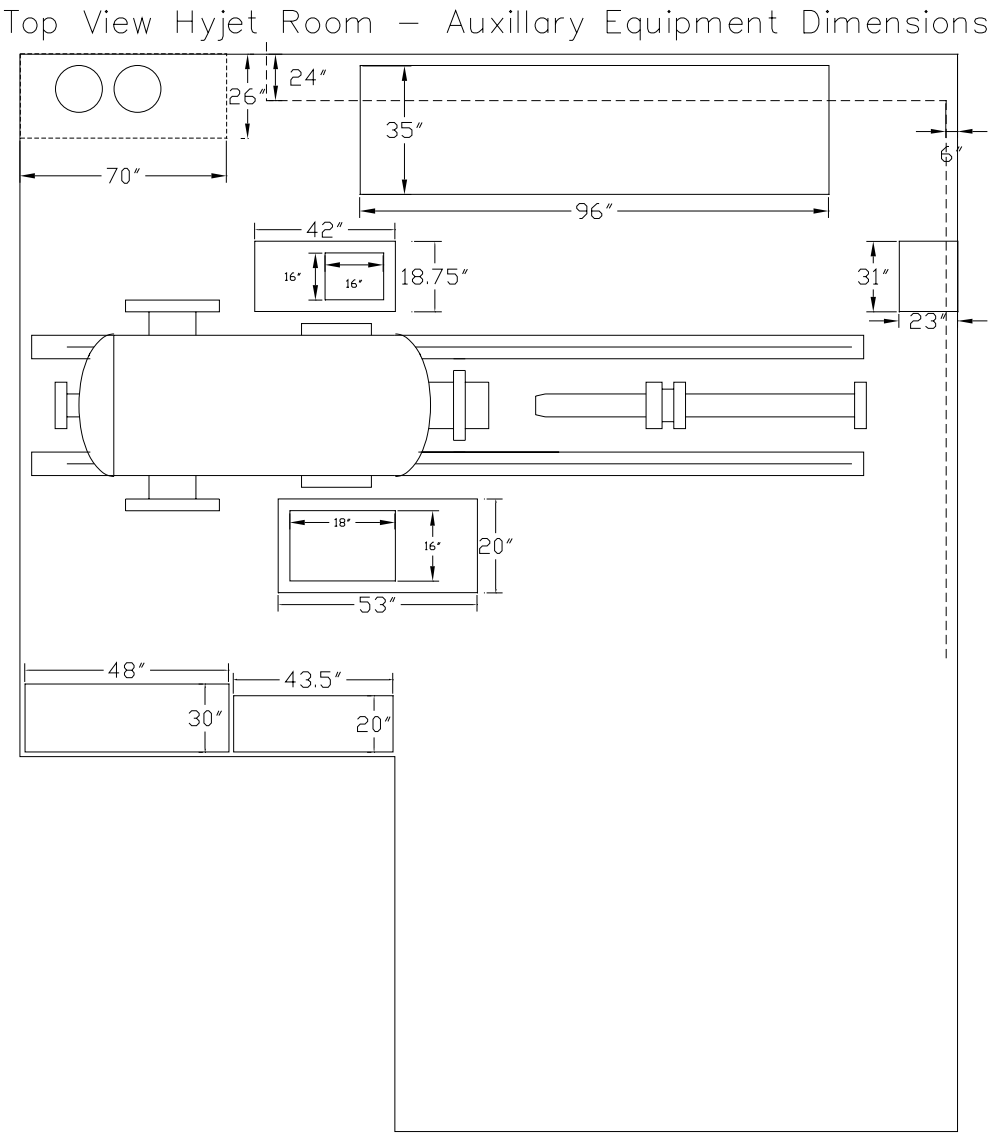

Figure 51: Sizes of components on plan view of layout of Explosion Dynamics Laboratory test area before modification.

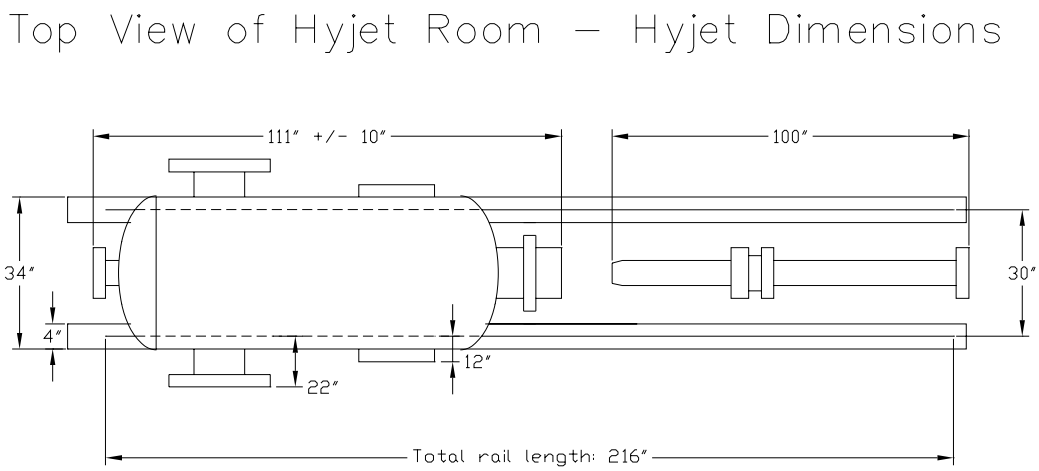

Figure 52: Dimensions of Hyjet facility (plan view) before modification.

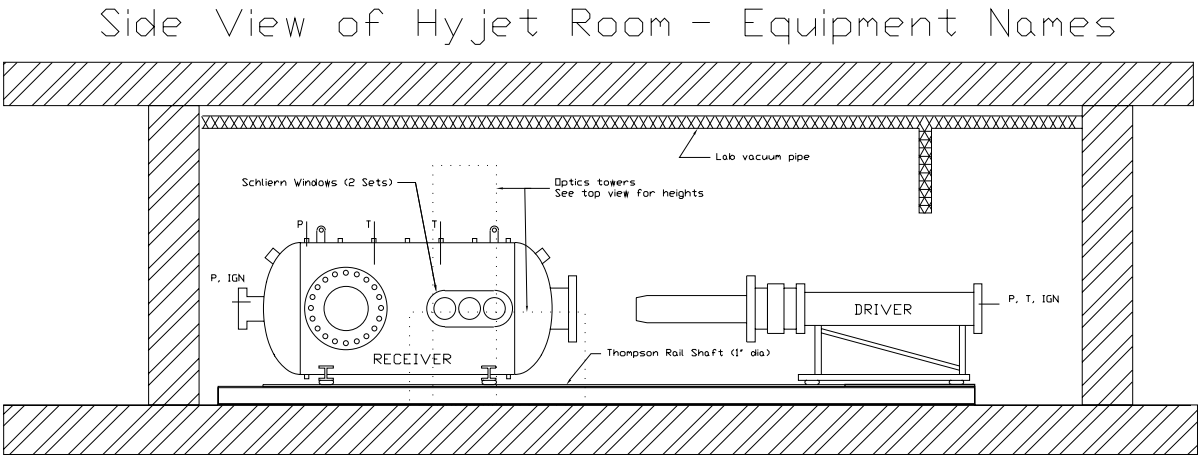

Figure 53: Component identification (side view) of Hyjet before modification.

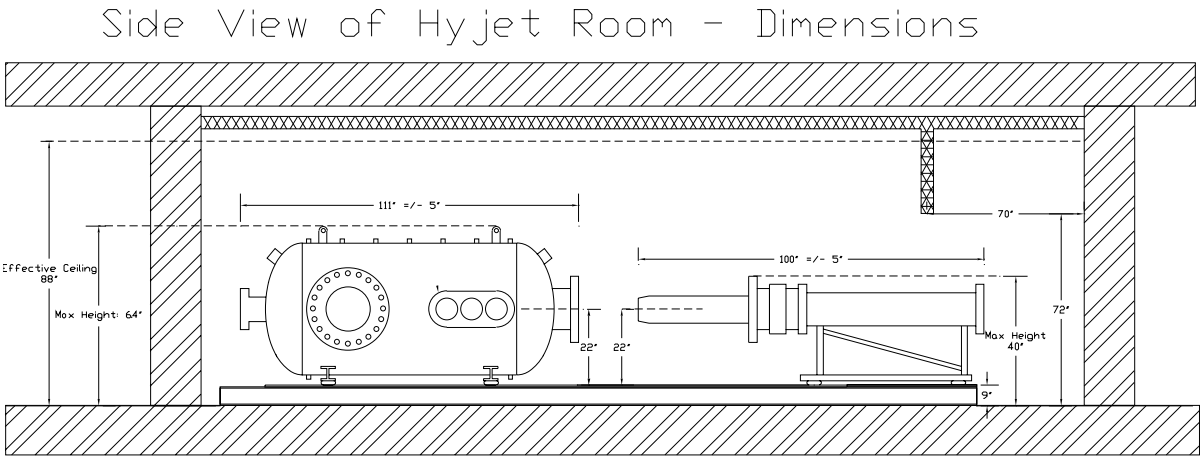

Figure 54: Component dimensions (side view) of Hyjet before modification.

B Test Matrix

Table 2: Parameters for initial series of tests.

Shot number	Driver pressure (kPa)	Receiver pressure (kPa)	Pressure ratio	Initial temperature (K)	Approximate start (s)	Approximate end (s)
1	200	0		300	0.15	0.6
2	300	100	3.0	302	0.14	0.35
3	300	150	2.0	302	0.15	0.3
4	300	75	4.0	304	0.14	0.37
5	300	60	5.0	304	0.13	0.4
6	300	37	8.1	304	0	0
7	300	37	8.1	304	0.14	0.5
8	300	30	10.0	304	0.14	0.5
9	200	50	4.0	301	0.14	0.4
10	400	50	8.0	303	0.15	0.5
11	125	25	5.0	298	0.15	0.4
12	125	24	5.2	298	0.15	0.4
13	200	50	4.0	300	0.05	0.4
14	250	50	5.0	301	0.05	0.4
15	300	50	6.0	301	0.05	0.5
16	150	50	3.0	297	0.05	0.4
17	200	50	4.0	300	0.04	0.4
18	300	30	10.0	302	0.04	0.5
19	200	50	4.0	299	0.05	0.6
20	200	50	4.0	300	0.05	0.6
21	200	50	4.0	298	0	0
22	200	50	4.0	300	0.05	0.4
23	200	50	4.0	299	0.05	0.4
24	200	50	4.0	300	0.05	0.3
25	100	50	2.0	300	0	0
26	100	50	2.0	294	0.05	0.2
27	120	60	2.0	300	0.05	0.2
28	120	70	1.7	295	0	0
29	120	70	1.7	295	0.05	0.2
30	120	70	1.7	296	0.05	0.2
31	110	70	1.6	295	0.05	0.2
32	105	70	1.5	295	0.05	0.2
33	105	75	1.4	295	0.05	0.2
34	120	70	1.7	296	0.05	0.2
35	120	67	1.8	300	0	0
36	120	70	1.7	295	0	0
37	120	70	1.7	295	0.05	0.3
38	120	70	1.7	66 296	0.05	0.3

C Data from tests without valve

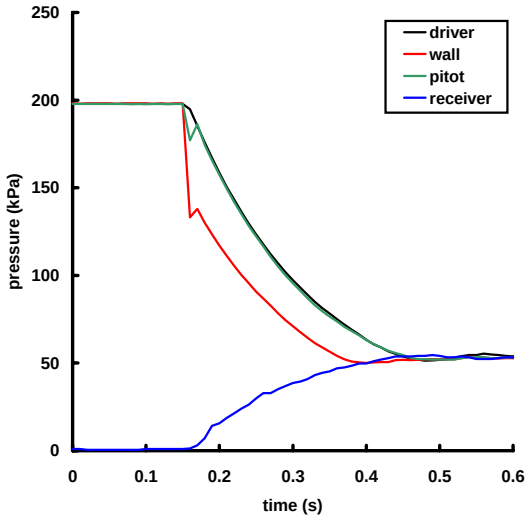

(a) Pressure

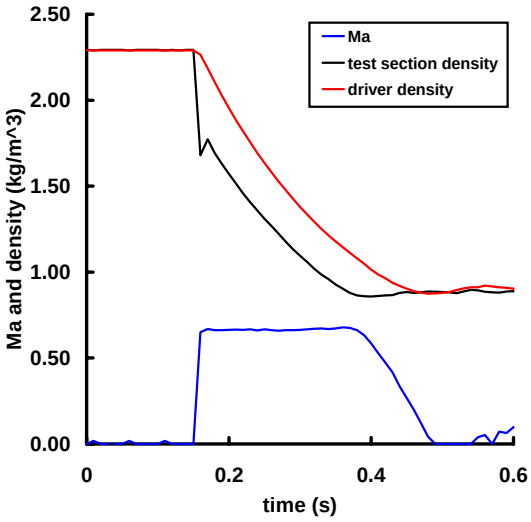

(b) Mach number and density

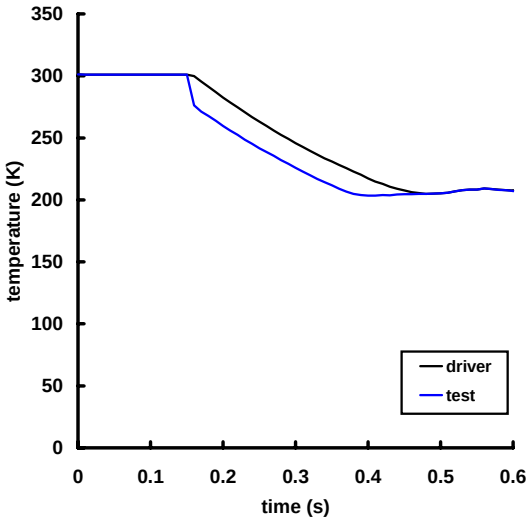

(c) Temperature

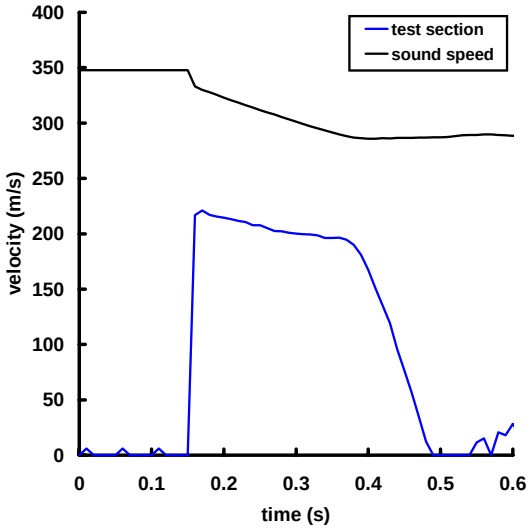

(d) Test section velocity

Figure 55: Shot 001.

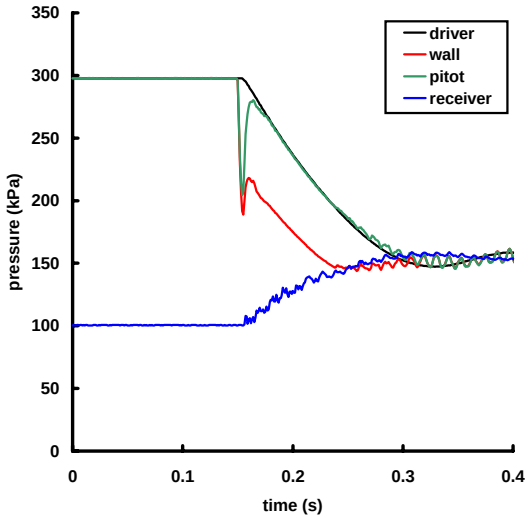

(a) Pressure

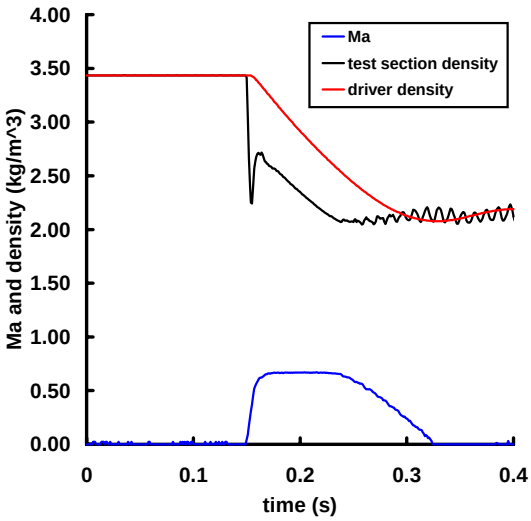

(b) Mach number and density

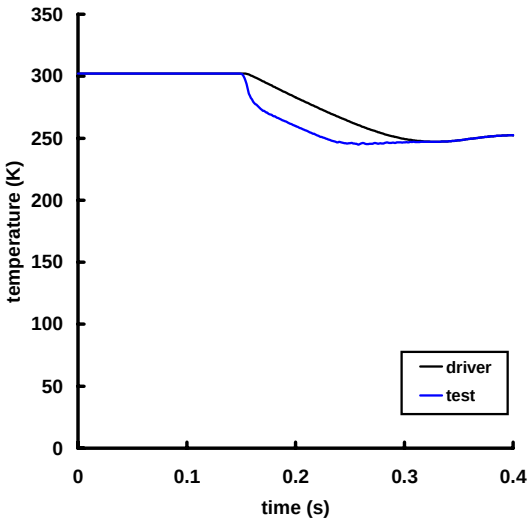

(c) Temperature

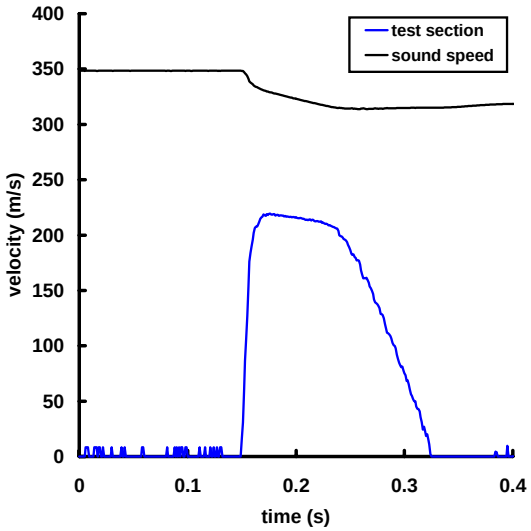

(d) Test section velocity

Figure 56: Shot 002.

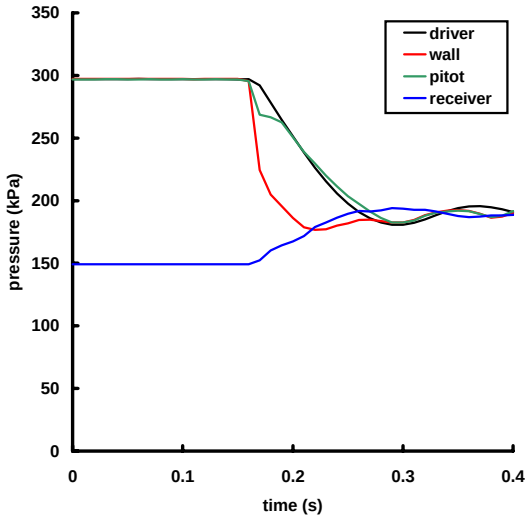

(a) Pressure

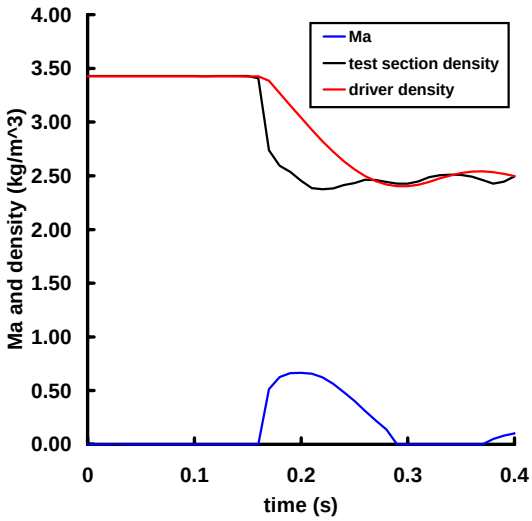

(b) Mach number and density

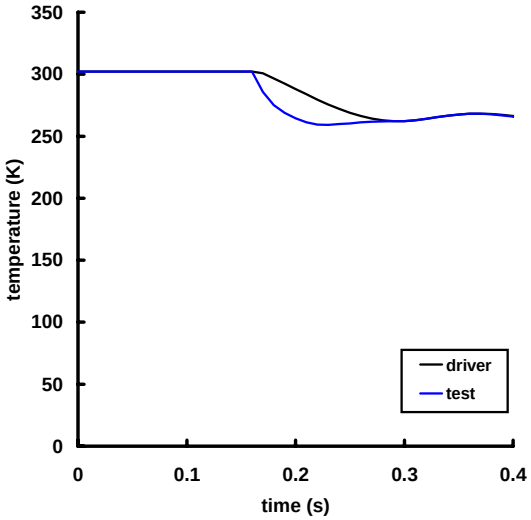

(c) Temperature

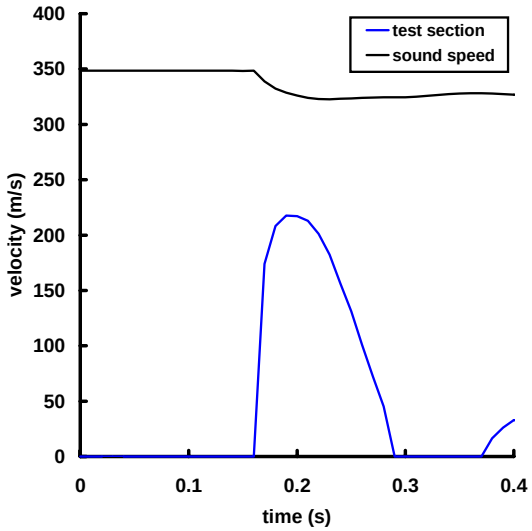

(d) Test section velocity

Figure 57: Shot 003.

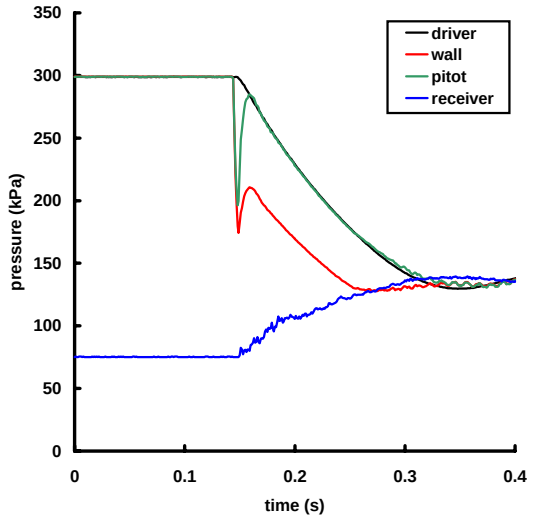

(a) Pressure

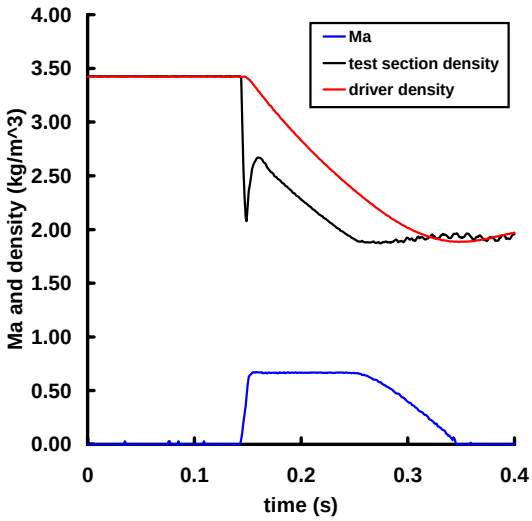

(b) Mach number and density

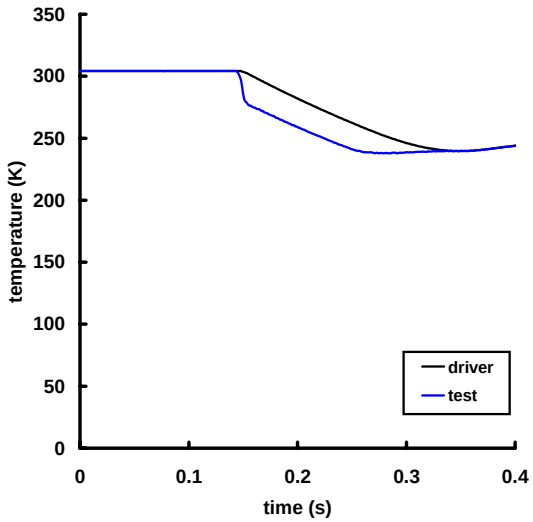

(c) Temperature

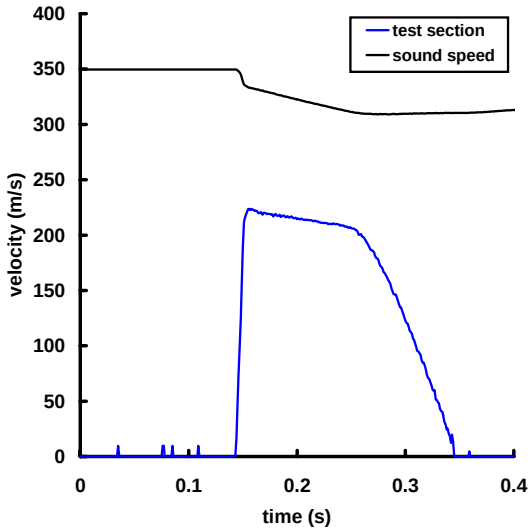

(d) Test section velocity

Figure 58: Shot 004.

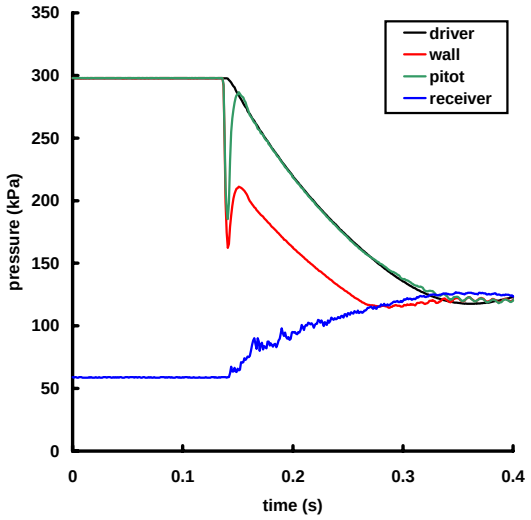

(a) Pressure

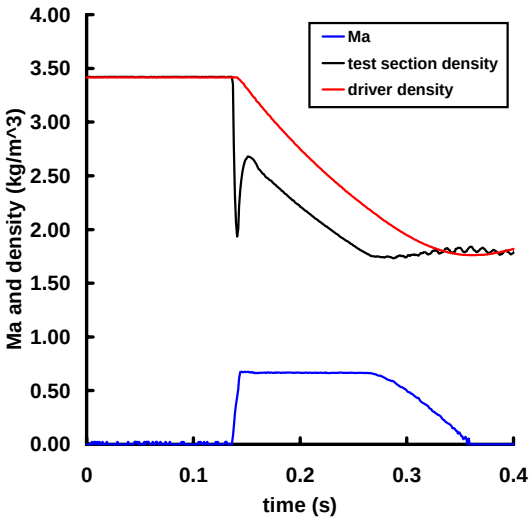

(b) Mach number and density

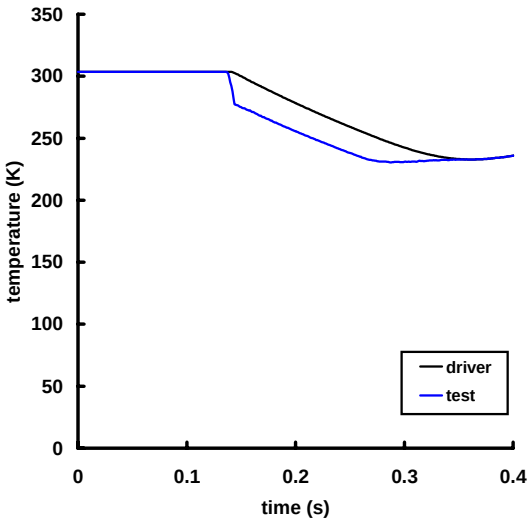

(c) Temperature

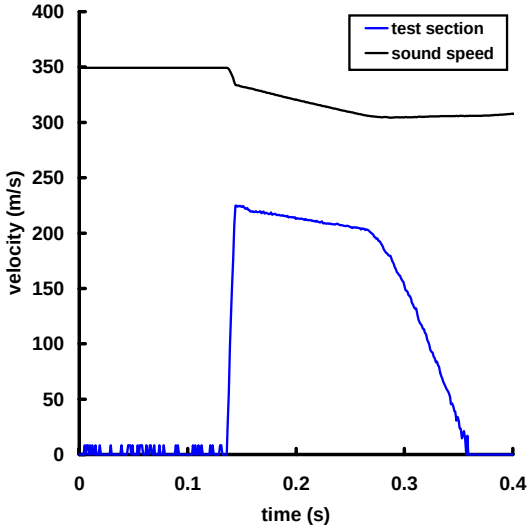

(d) Test section velocity

Figure 59: Shot 005.

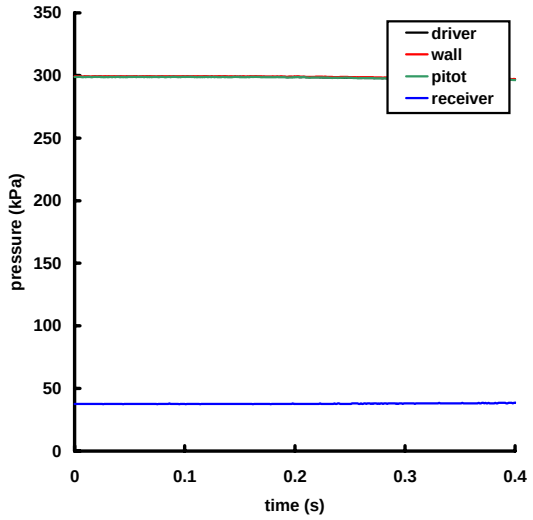

(a) Pressure

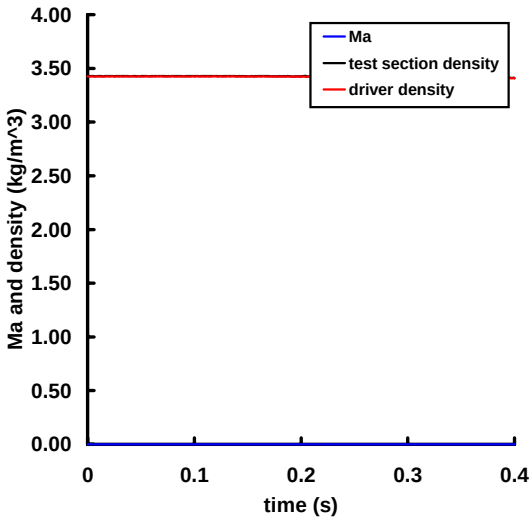

(b) Mach number and density

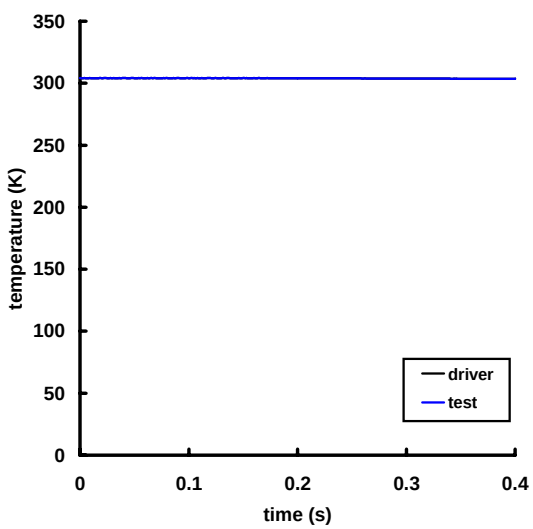

(c) Temperature

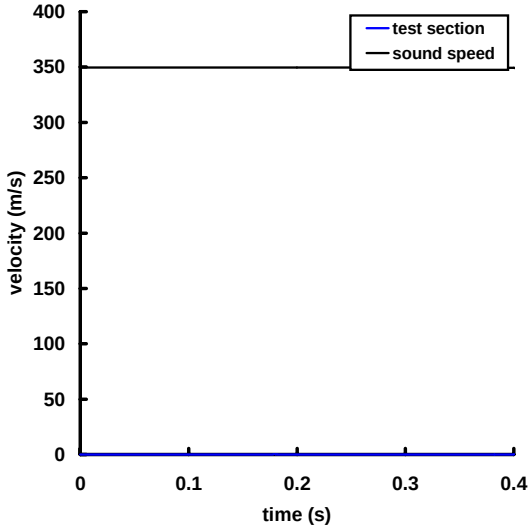

(d) Test section velocity

Figure 60: Shot 006.

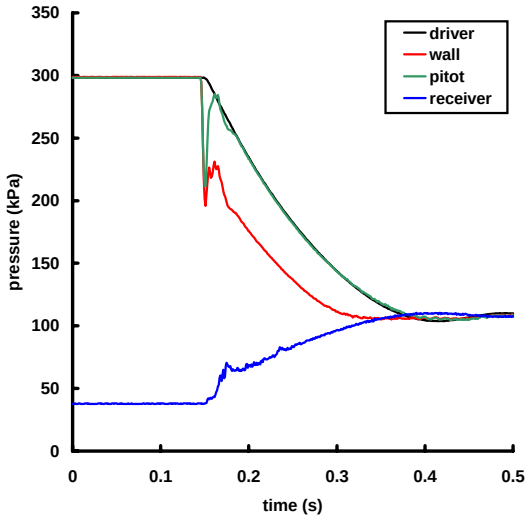

(a) Pressure

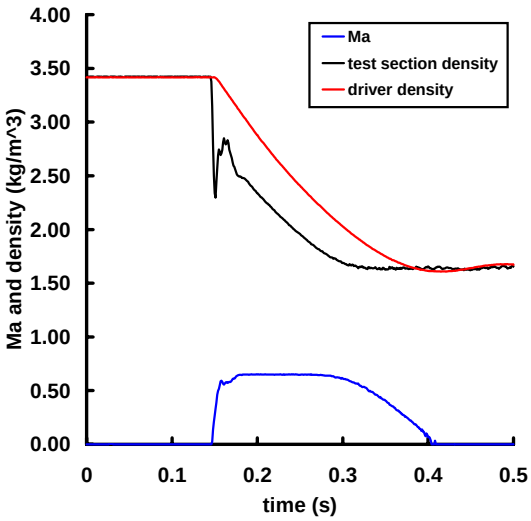

(b) Mach number and density

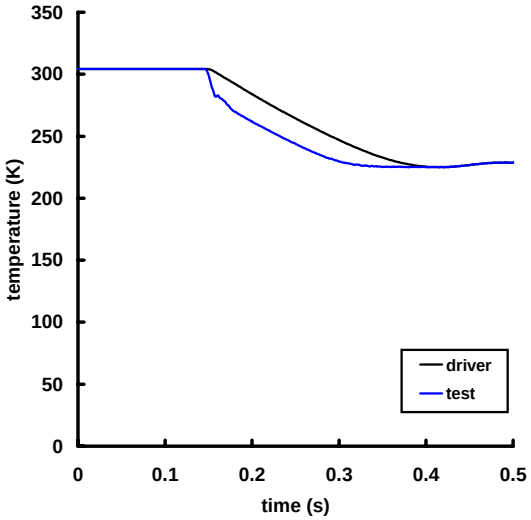

(c) Temperature

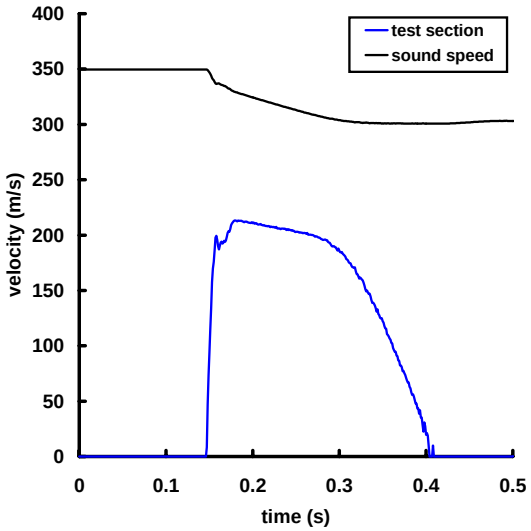

(d) Test section velocity

Figure 61: Shot 007.

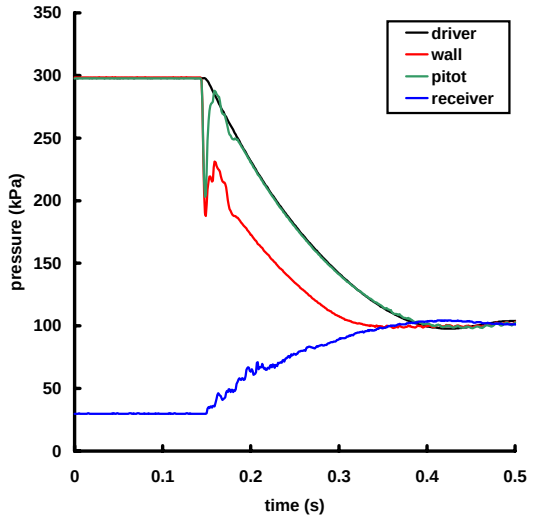

(a) Pressure

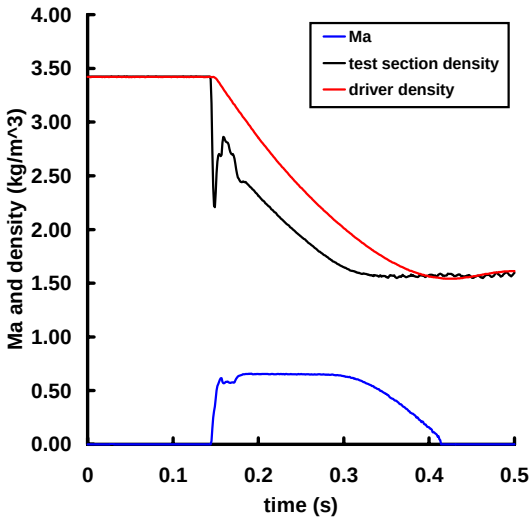

(b) Mach number and density

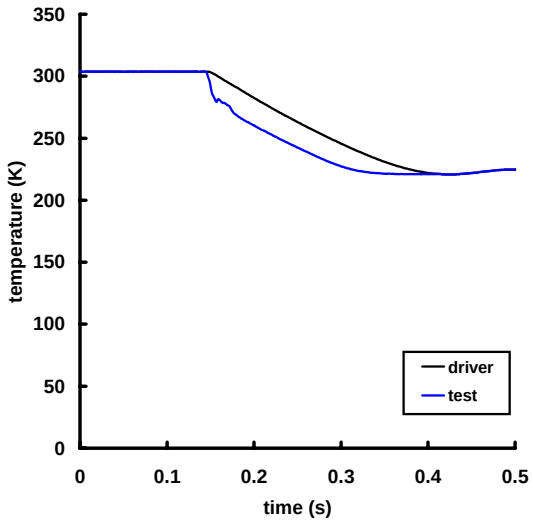

(c) Temperature

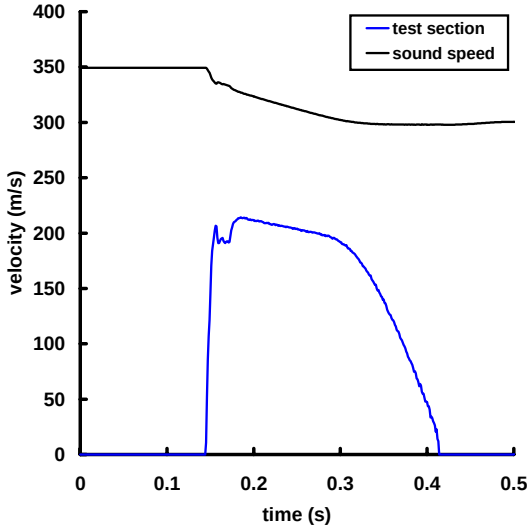

(d) Test section velocity

Figure 62: Shot 008.

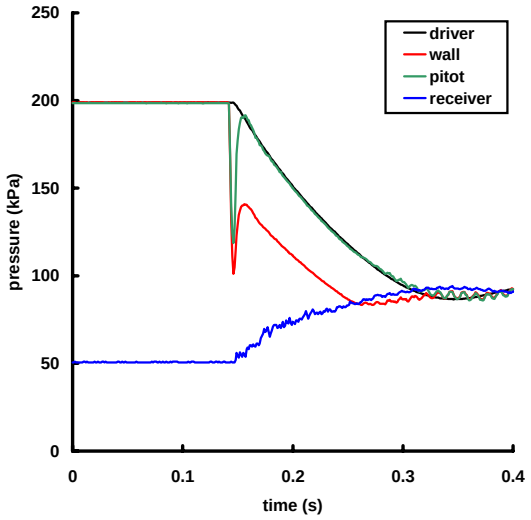

(a) Pressure

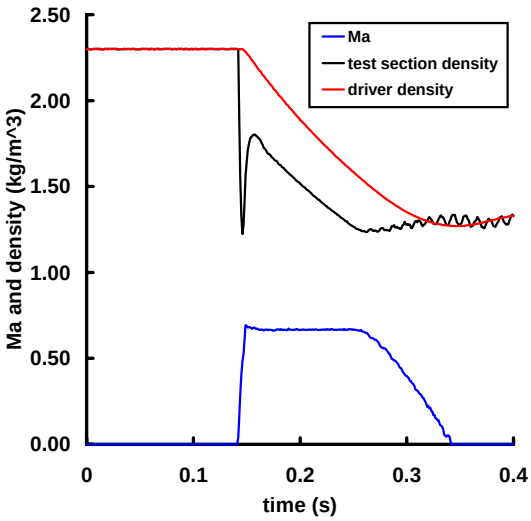

(b) Mach number and density

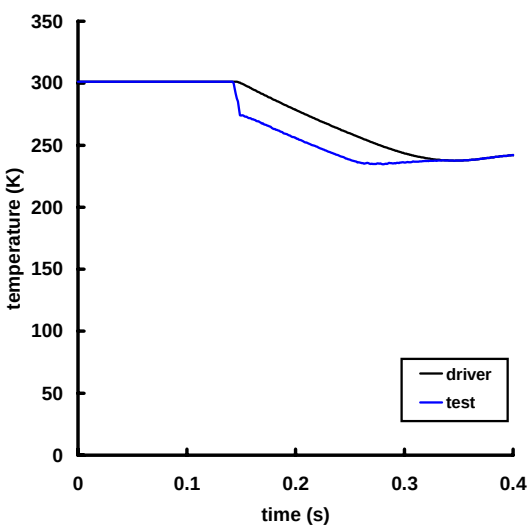

(c) Temperature

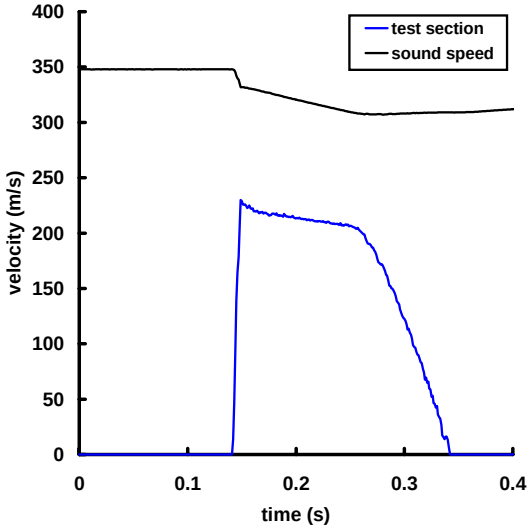

(d) Test section velocity

Figure 63: Shot 009.

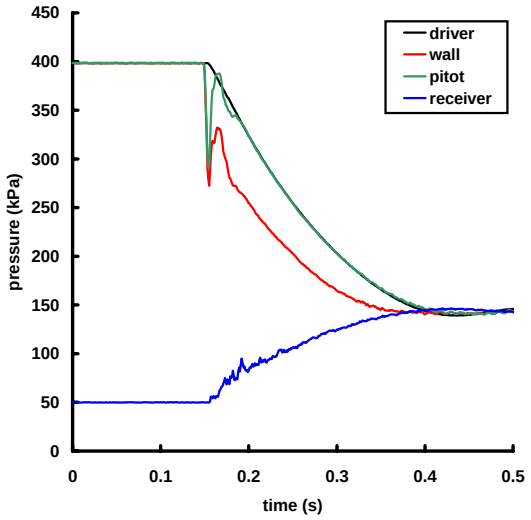

(a) Pressure

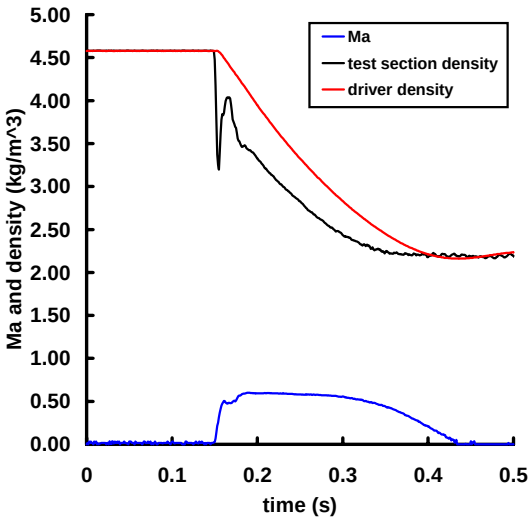

(b) Mach number and density

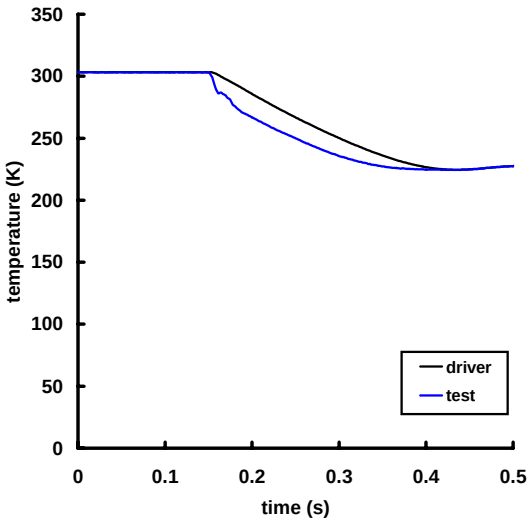

(c) Temperature

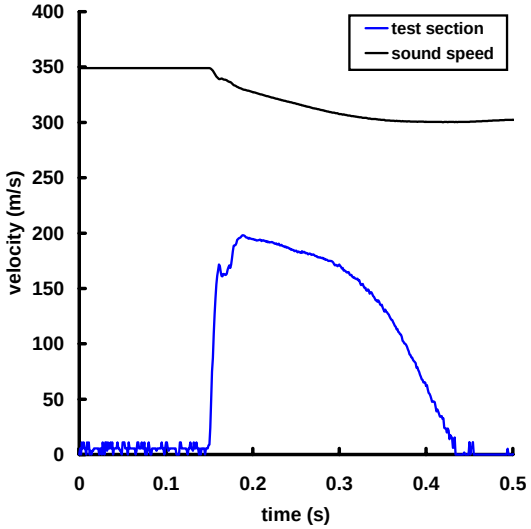

(d) Test section velocity

Figure 64: Shot 010.

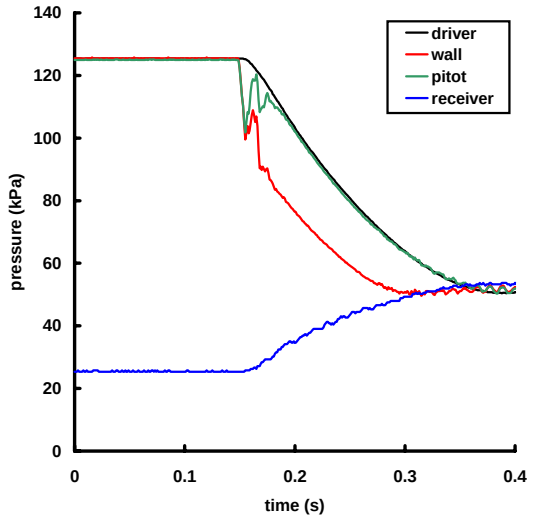

(a) Pressure

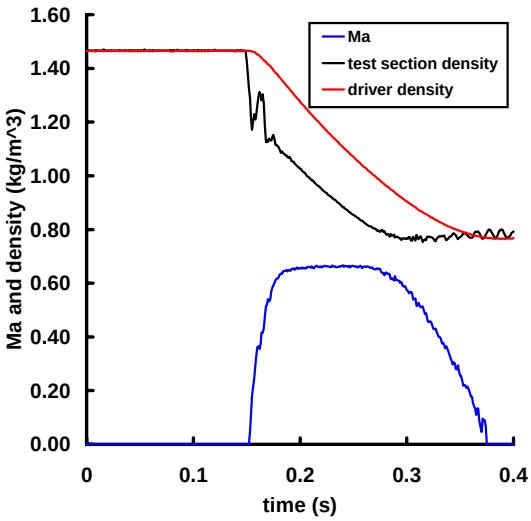

(b) Mach number and density

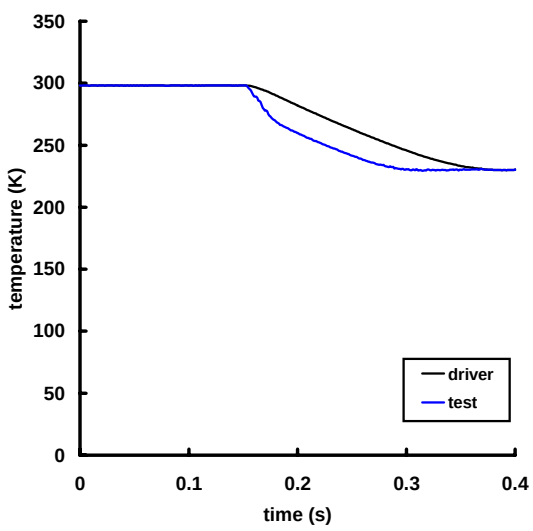

(c) Temperature

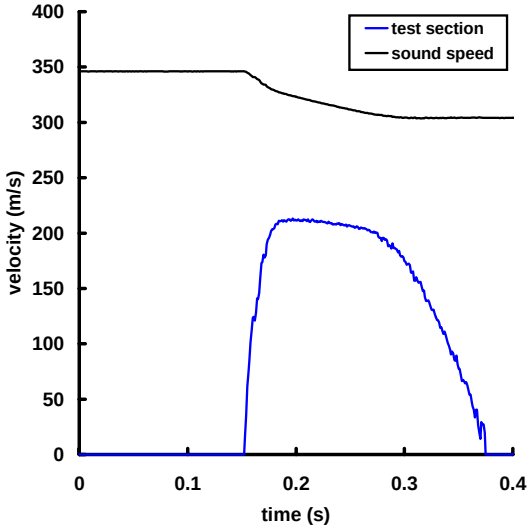

(d) Test section velocity

Figure 65: Shot 011.

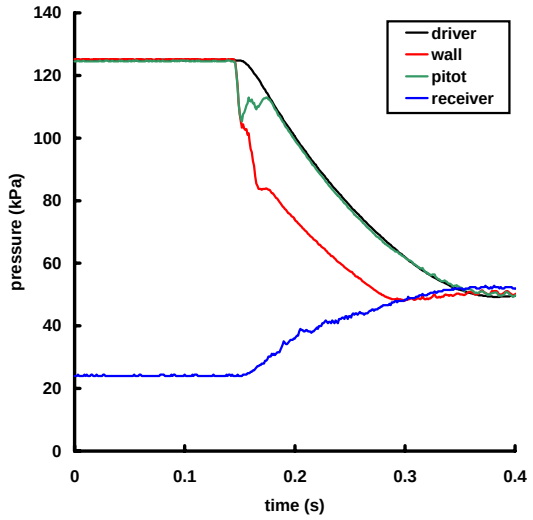

(a) Pressure

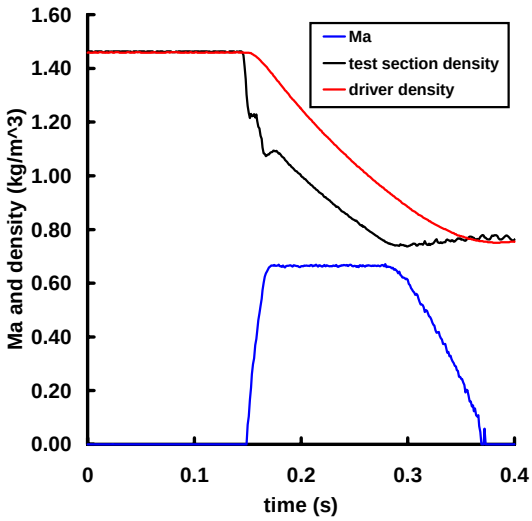

(b) Mach number and density

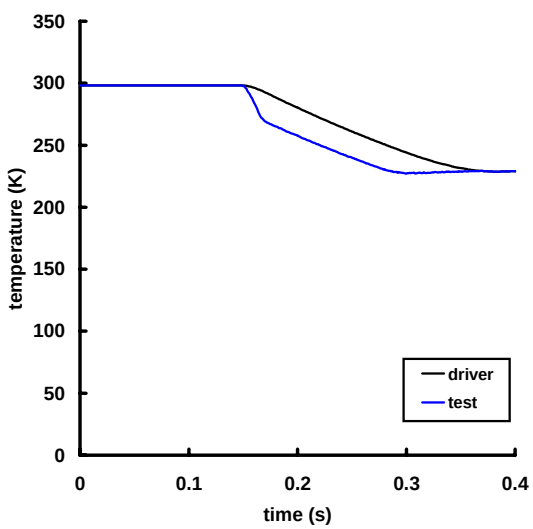

(c) Temperature

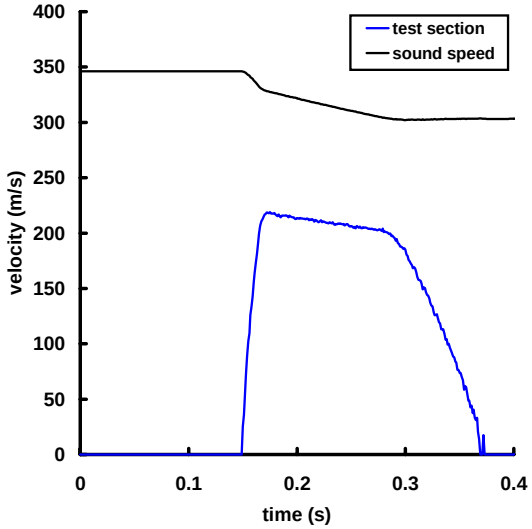

(d) Test section velocity

Figure 66: Shot 012.

D Data from tests with valve installed

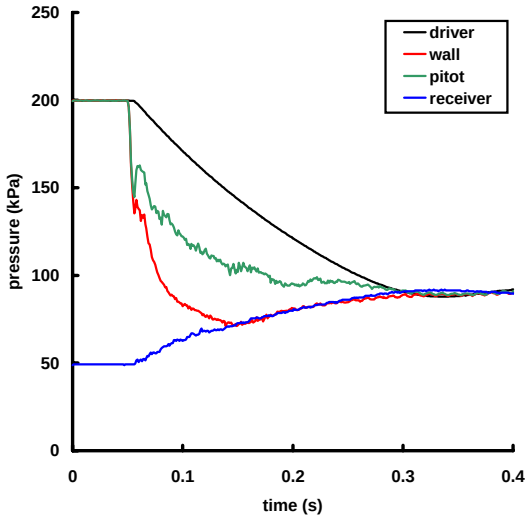

(a) Pressure

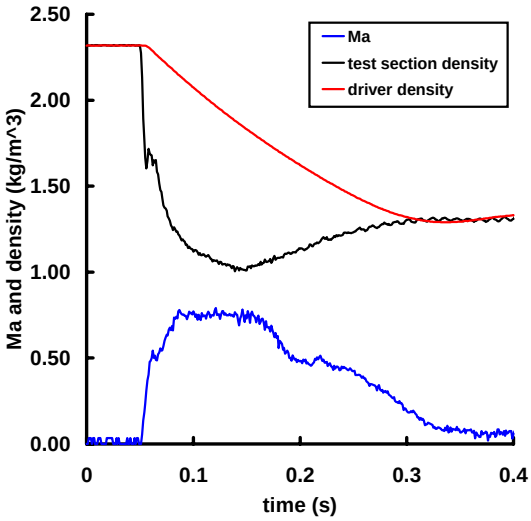

(b) Mach number and density

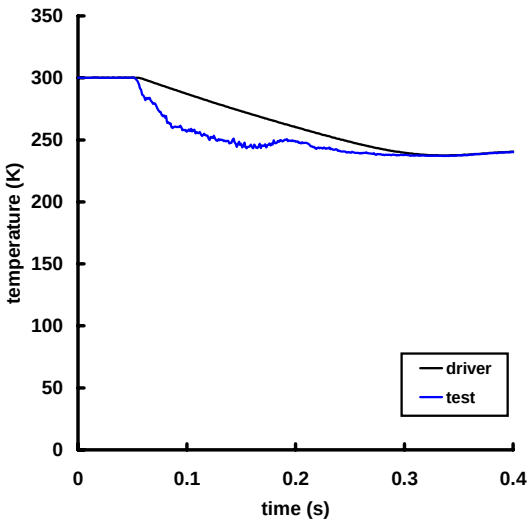

(c) Temperature

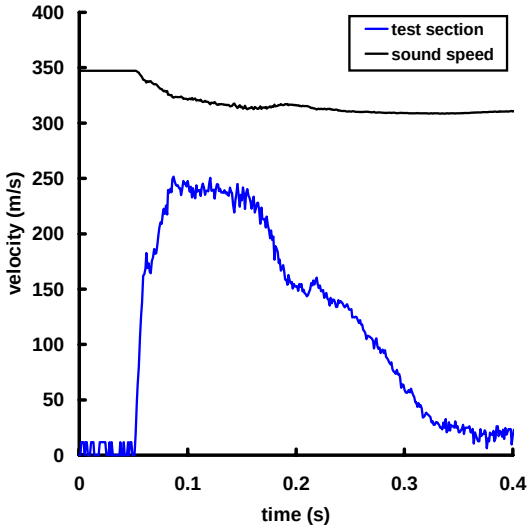

(d) Test section velocity

Figure 67: Shot 013.

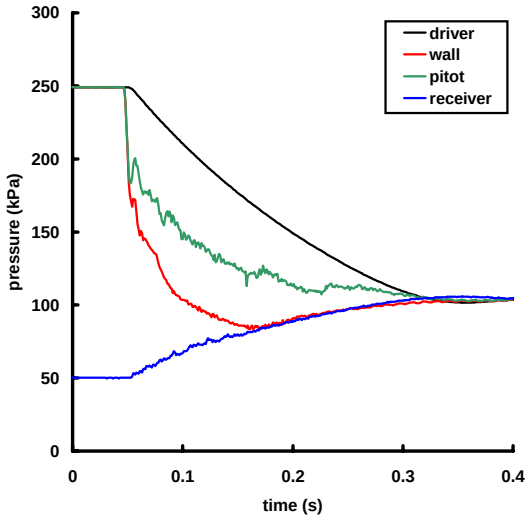

(a) Pressure

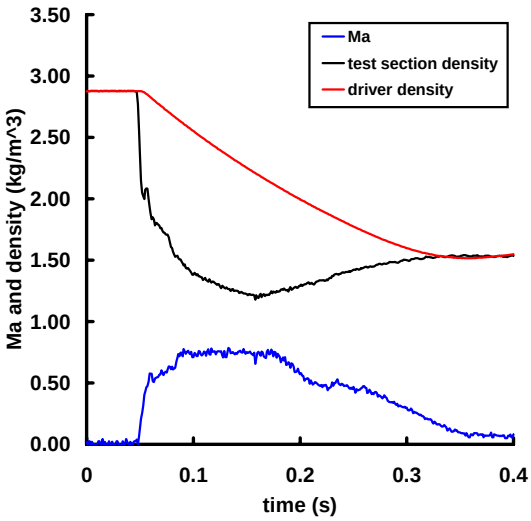

(b) Mach number and density

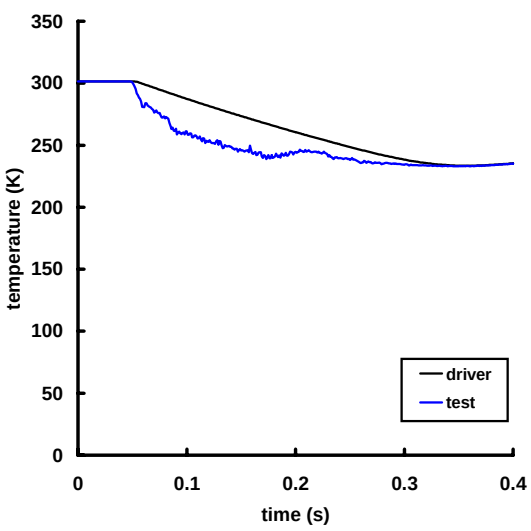

(c) Temperature

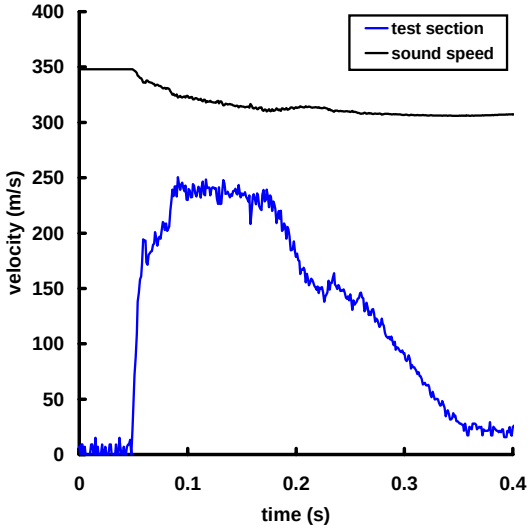

(d) Test section velocity

Figure 68: Shot 014.

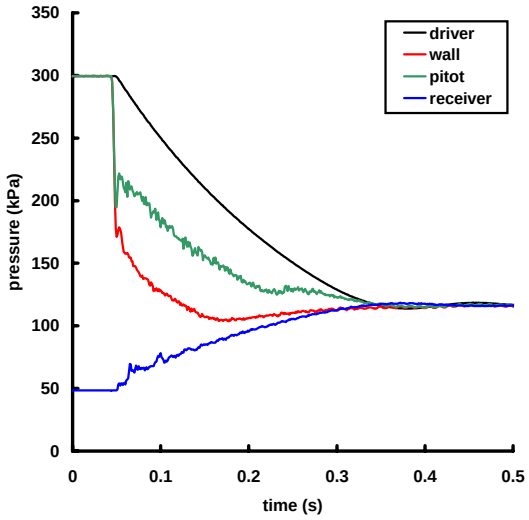

(a) Pressure

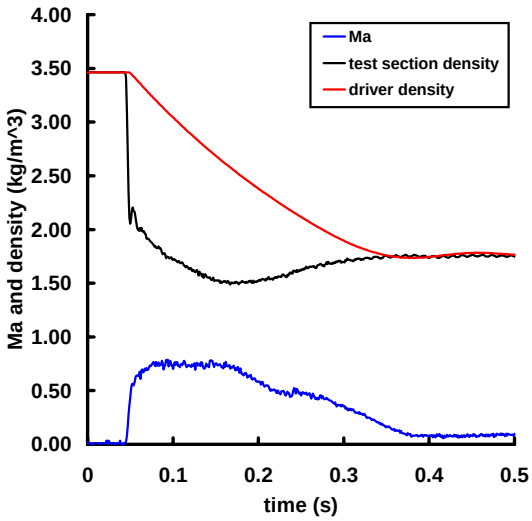

(b) Mach number and density

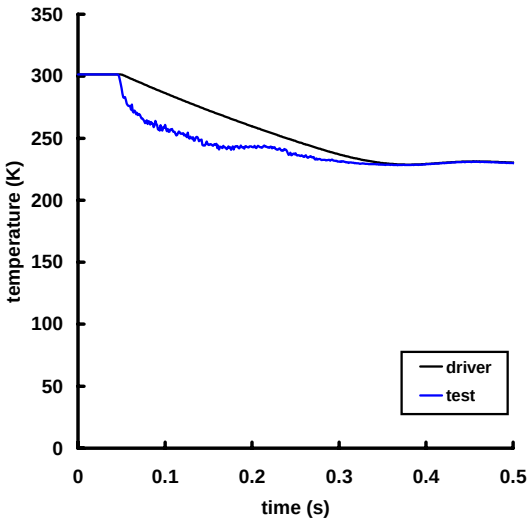

(c) Temperature

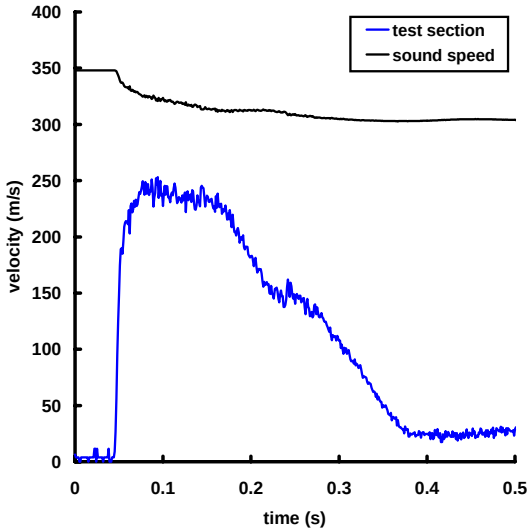

(d) Test section velocity

Figure 69: Shot 015.

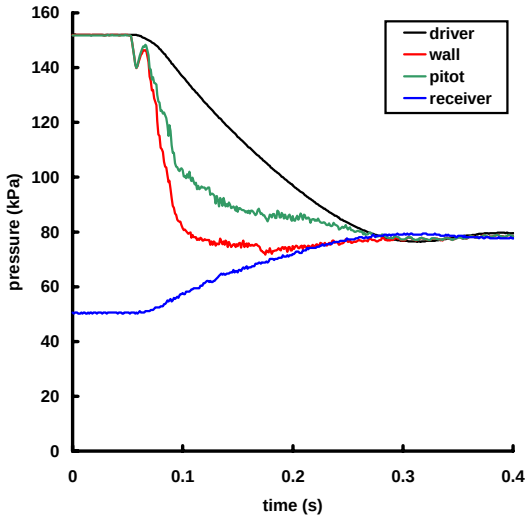

(a) Pressure

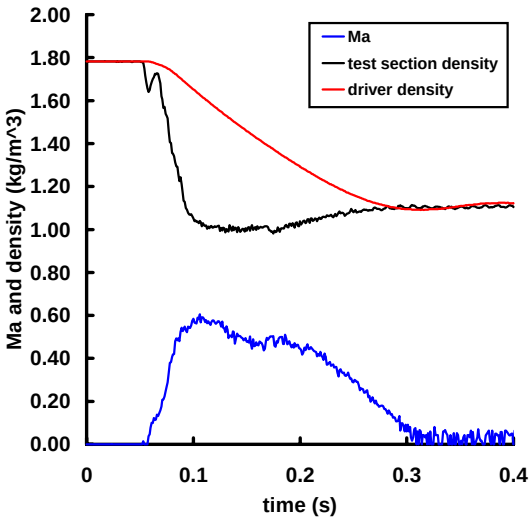

(b) Mach number and density

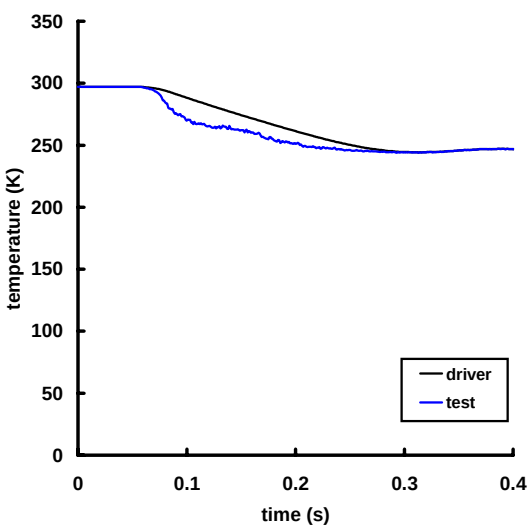

(c) Temperature

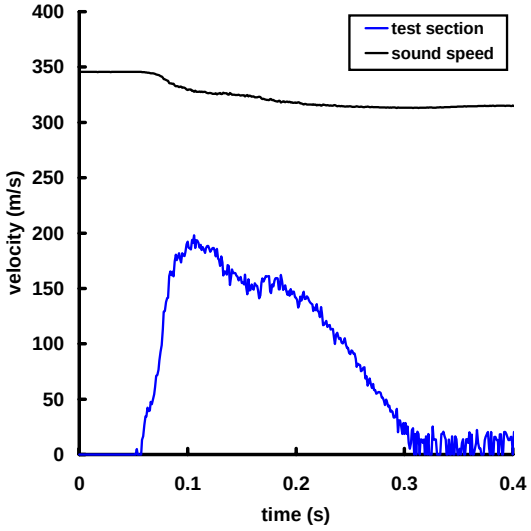

(d) Test section velocity

Figure 70: Shot 016.

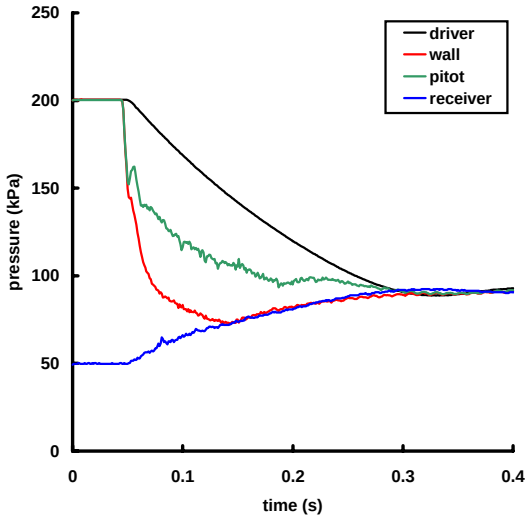

(a) Pressure

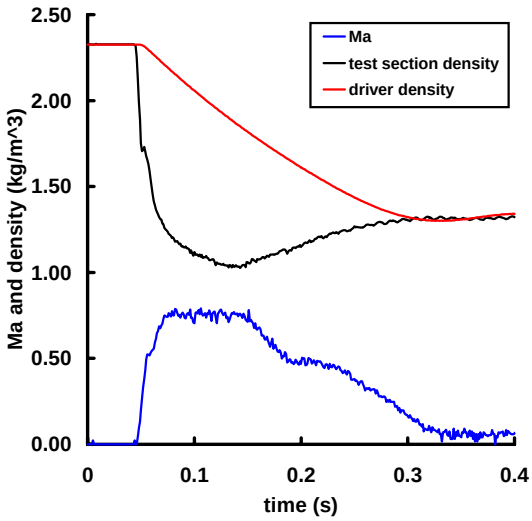

(b) Mach number and density

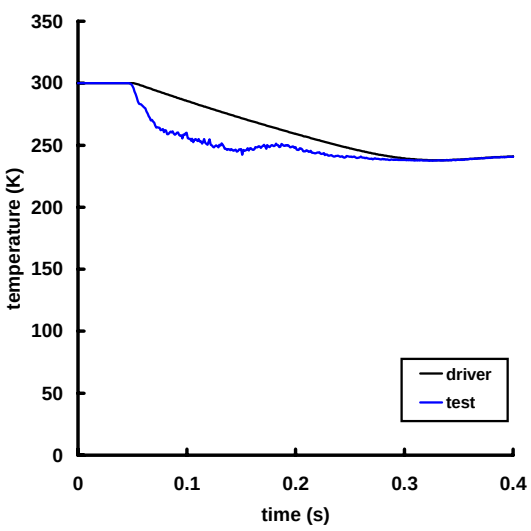

(c) Temperature

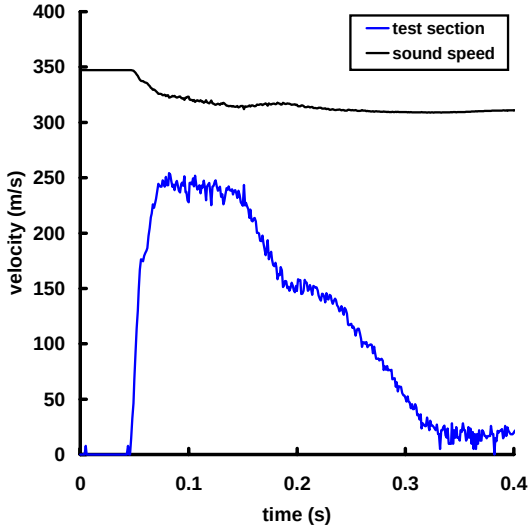

(d) Test section velocity

Figure 71: Shot 017.

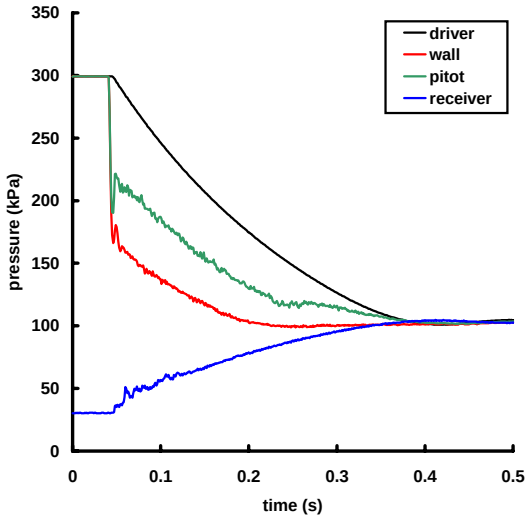

(a) Pressure

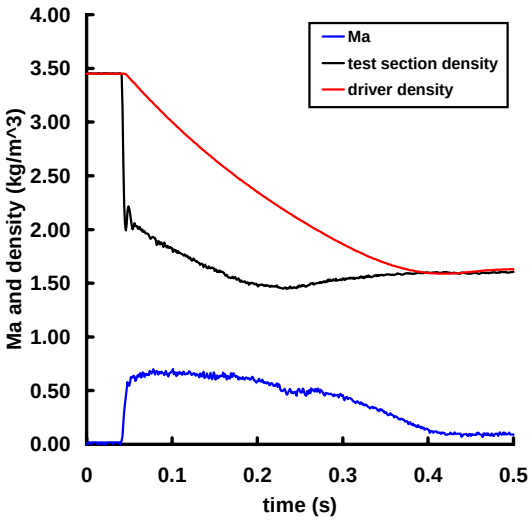

(b) Mach number and density

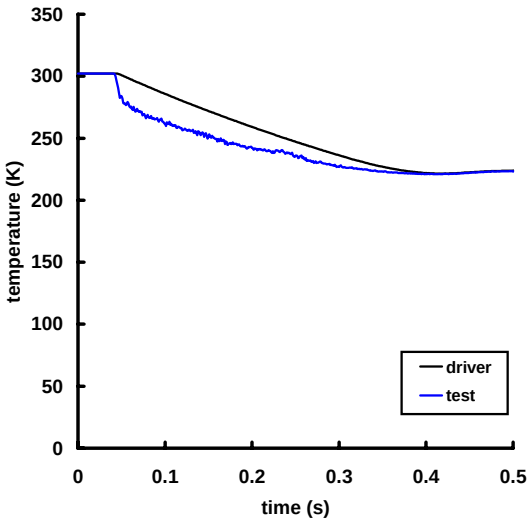

(c) Temperature

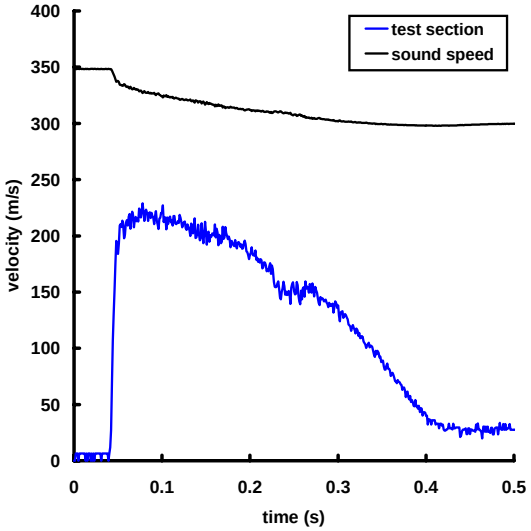

(d) Test section velocity

Figure 72: Shot 018.

E Data from tests with valve actuation

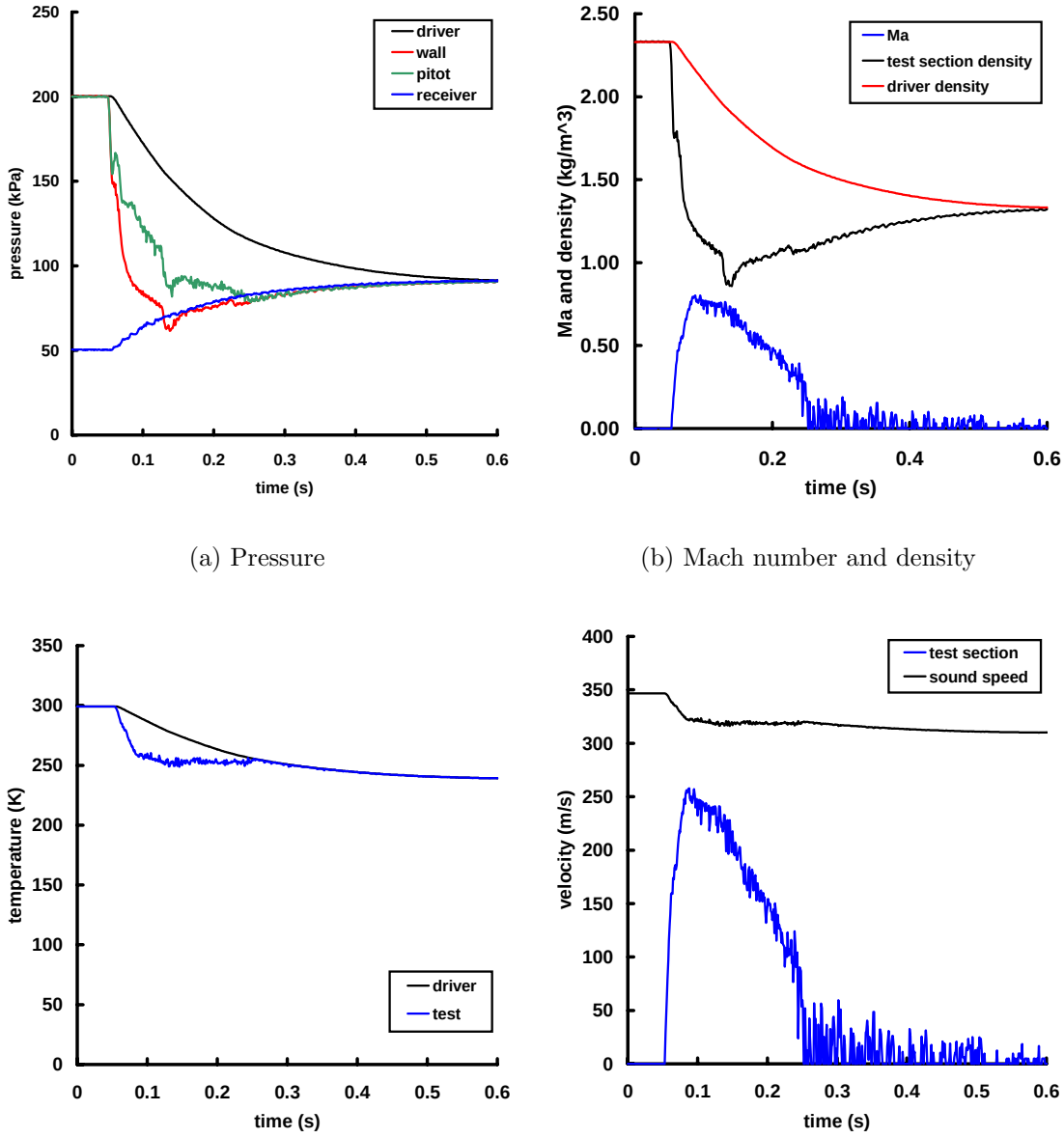

(a) Pressure

(b) Mach number and density

(c) Temperature

(d) Test section velocity

Figure 73: Shot 019.

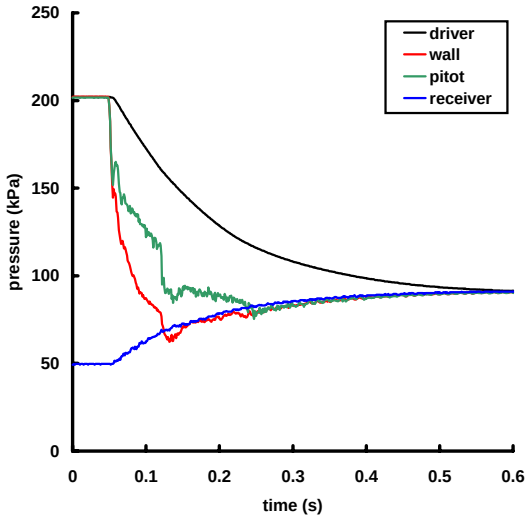

(a) Pressure

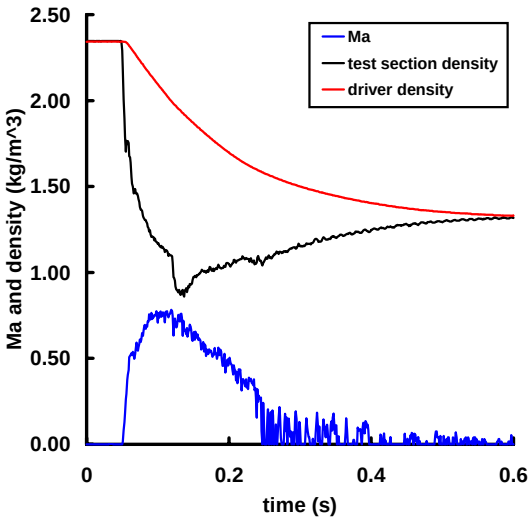

(b) Mach number and density

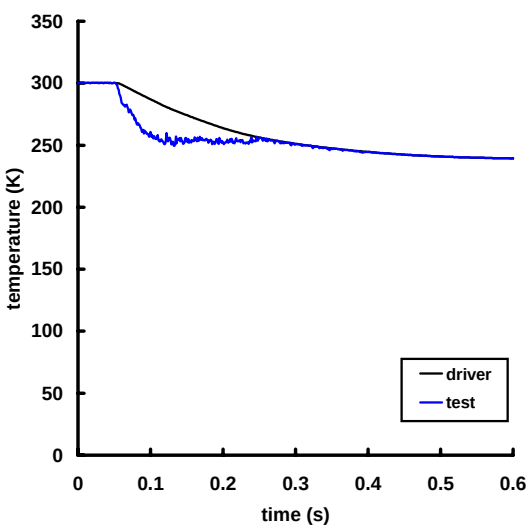

(c) Temperature

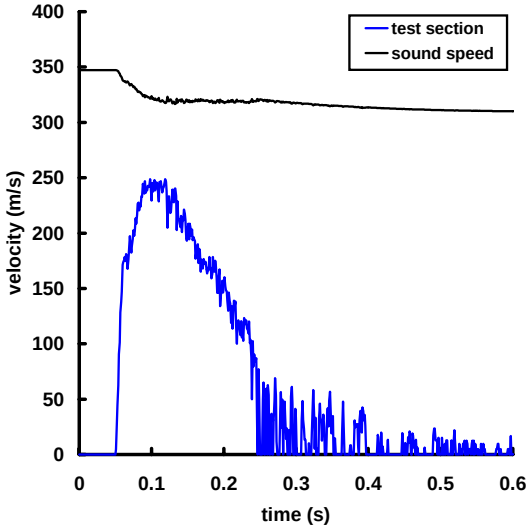

(d) Test section velocity

Figure 74: Shot 020.

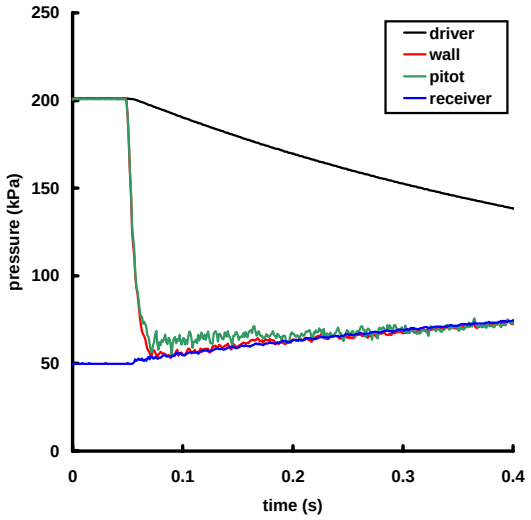

(a) Pressure

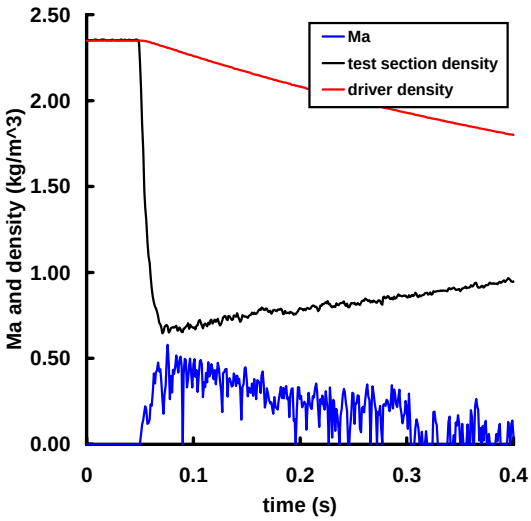

(b) Mach number and density

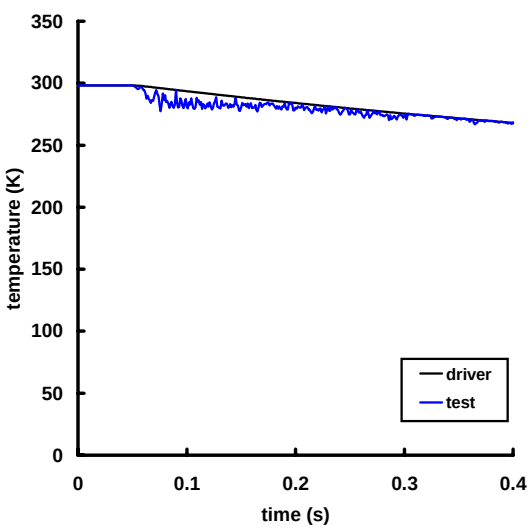

(c) Temperature

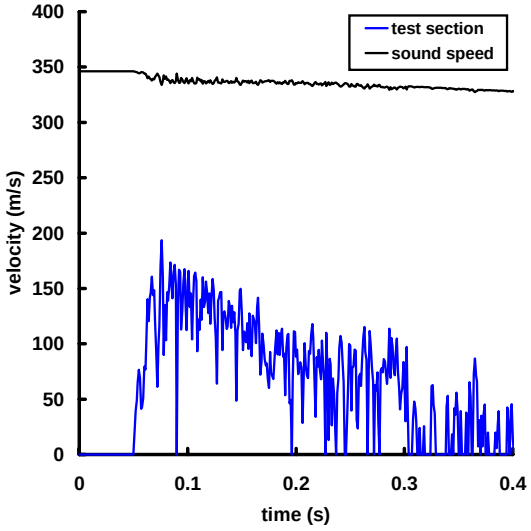

(d) Test section velocity

Figure 75: Shot 021.

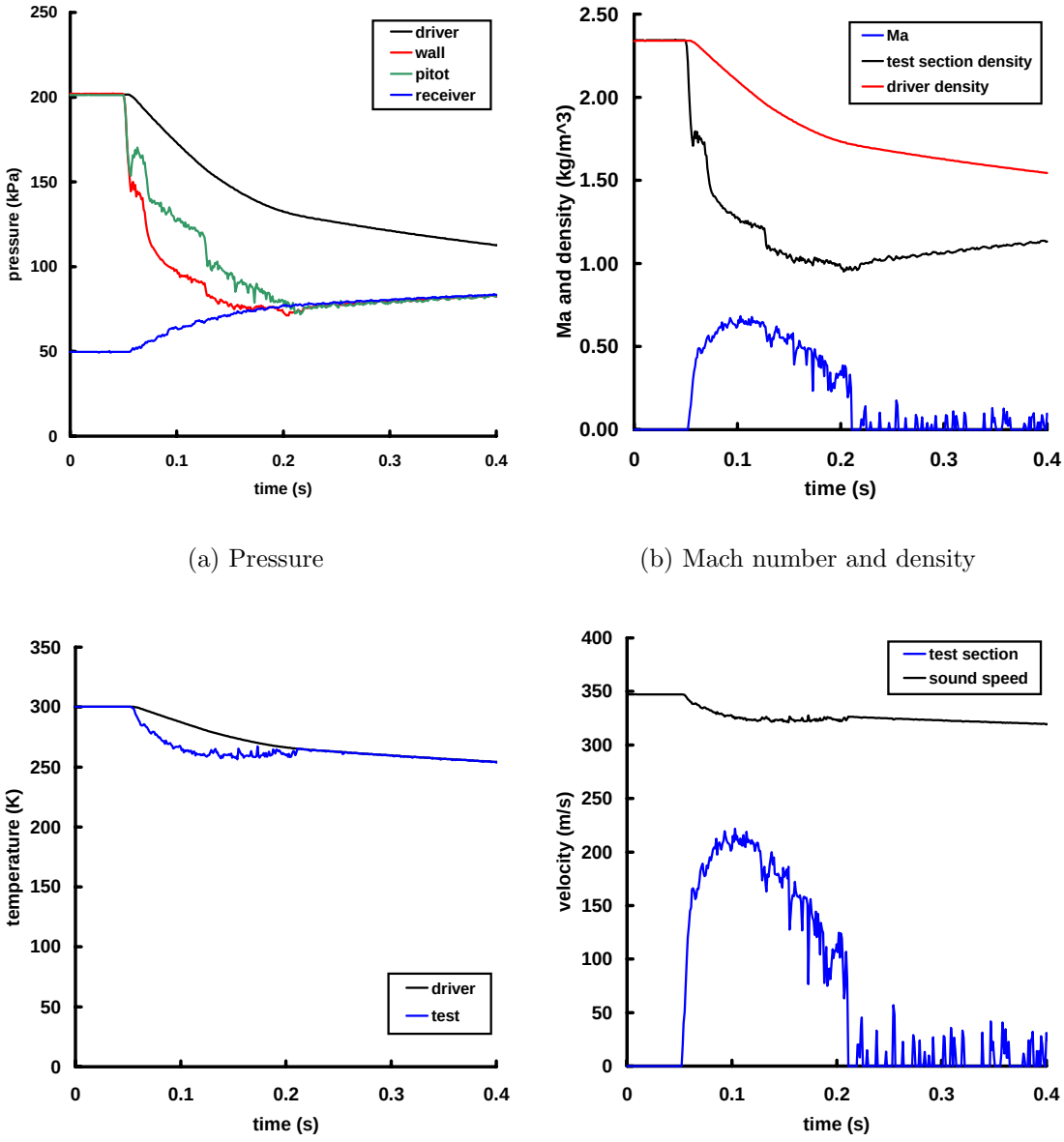

(a) Pressure

(b) Mach number and density

(c) Temperature

(d) Test section velocity

Figure 76: Shot 022.

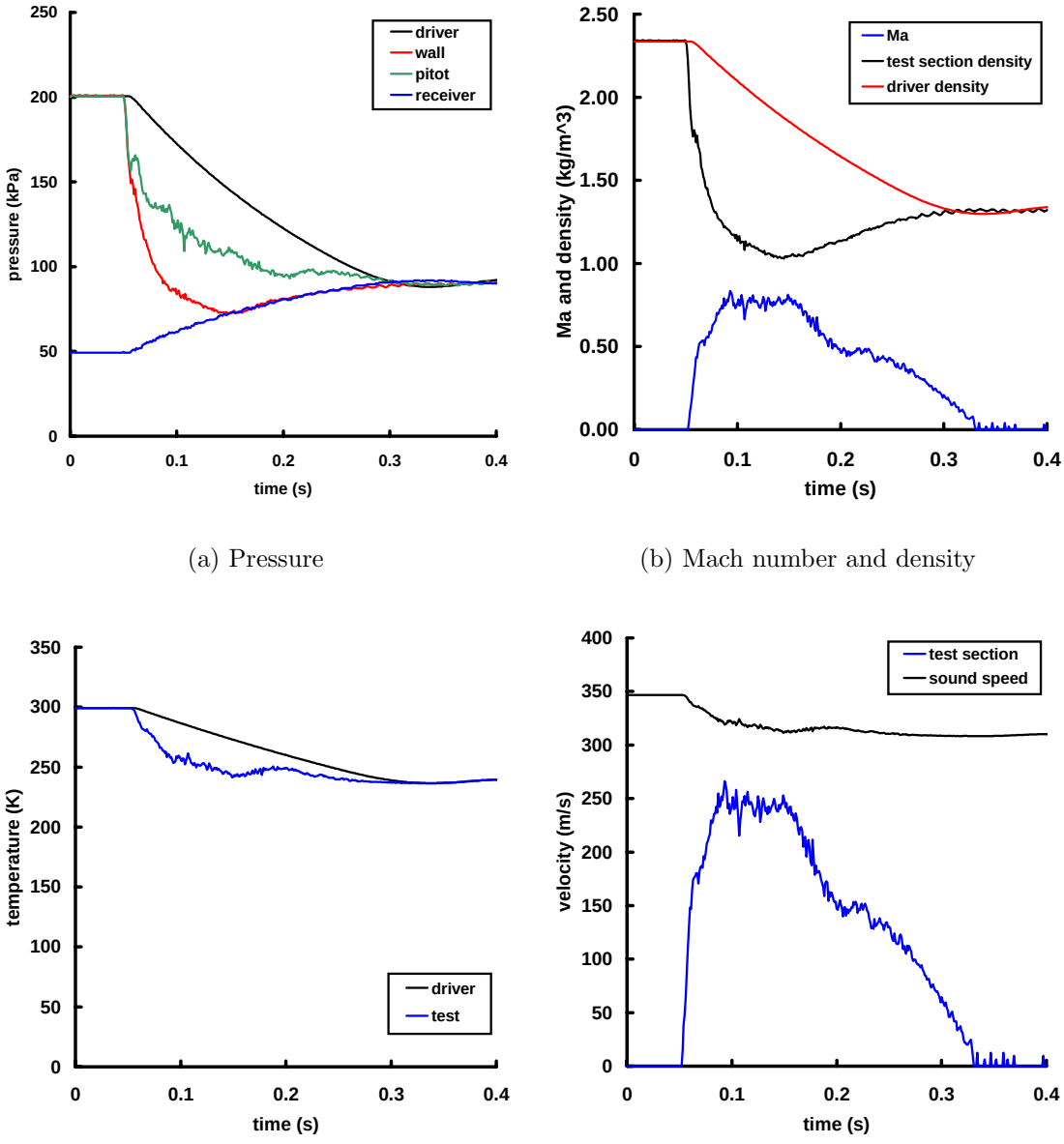

(a) Pressure

(b) Mach number and density

(c) Temperature

(d) Test section velocity

Figure 77: Shot 023.

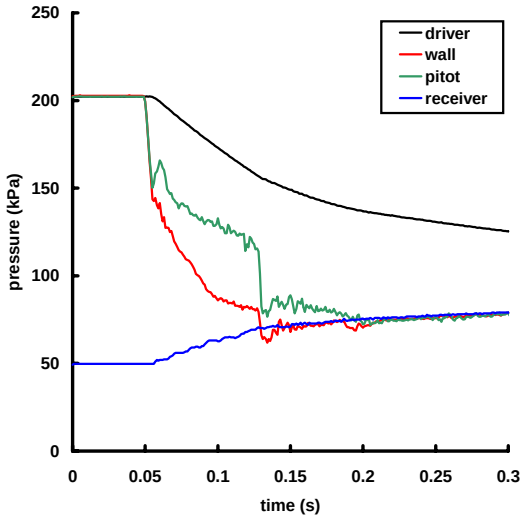

(a) Pressure

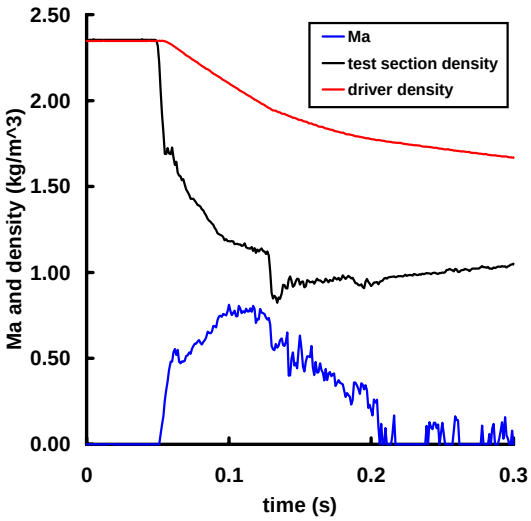

(b) Mach number and density

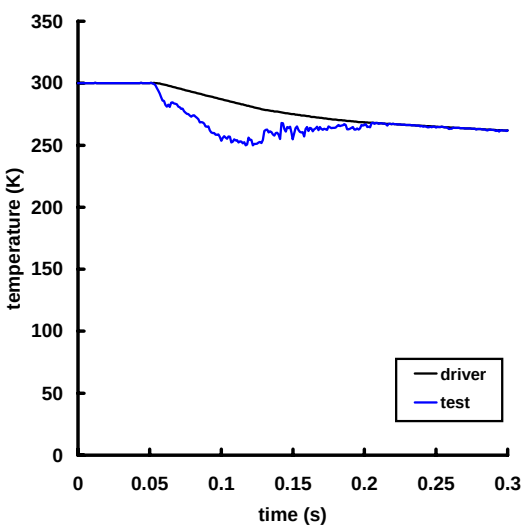

(c) Temperature

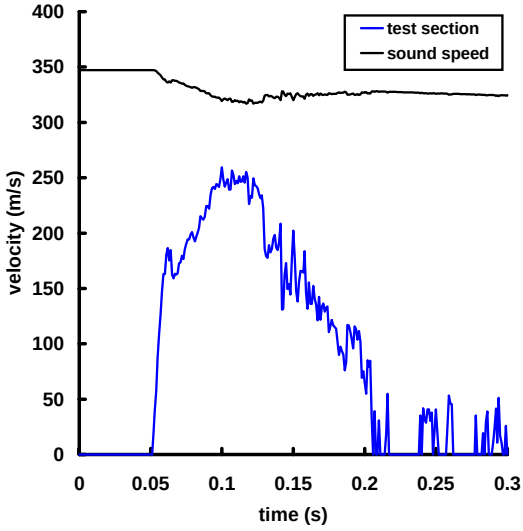

(d) Test section velocity

Figure 78: Shot 024.

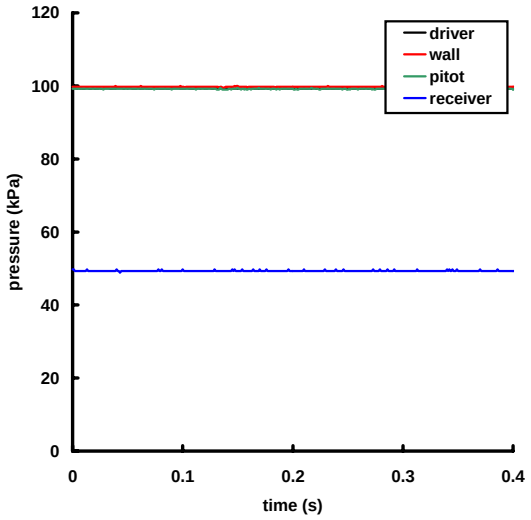

(a) Pressure

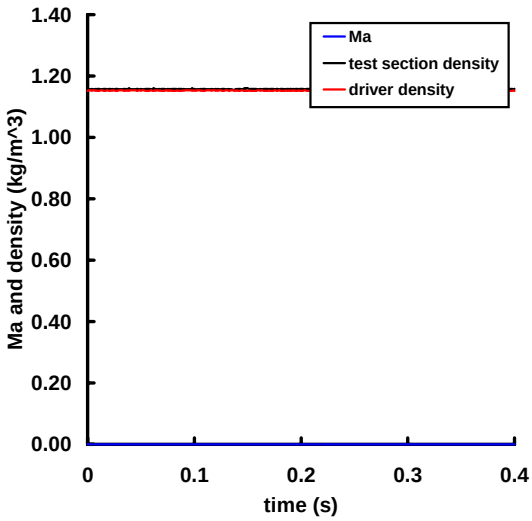

(b) Mach number and density

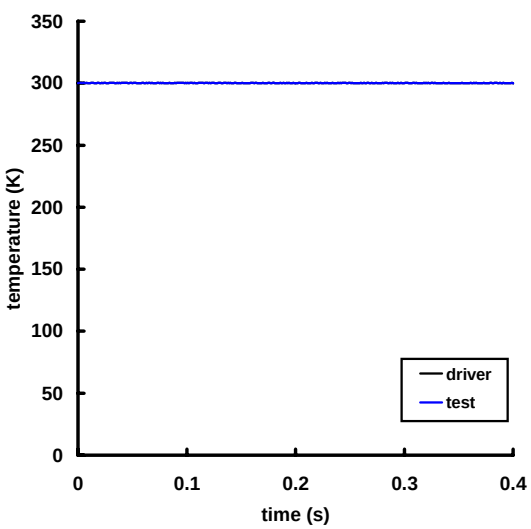

(c) Temperature

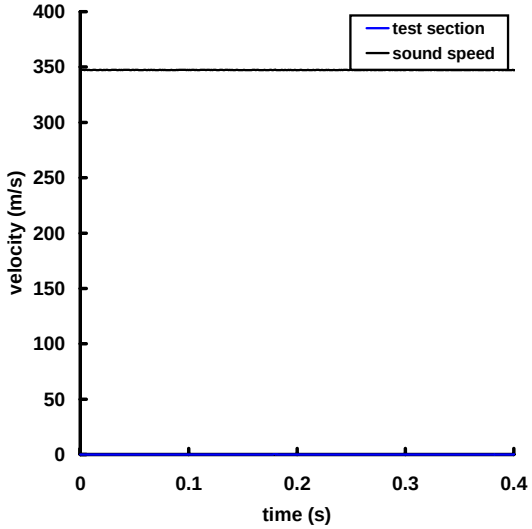

(d) Test section velocity

Figure 79: Shot 025.

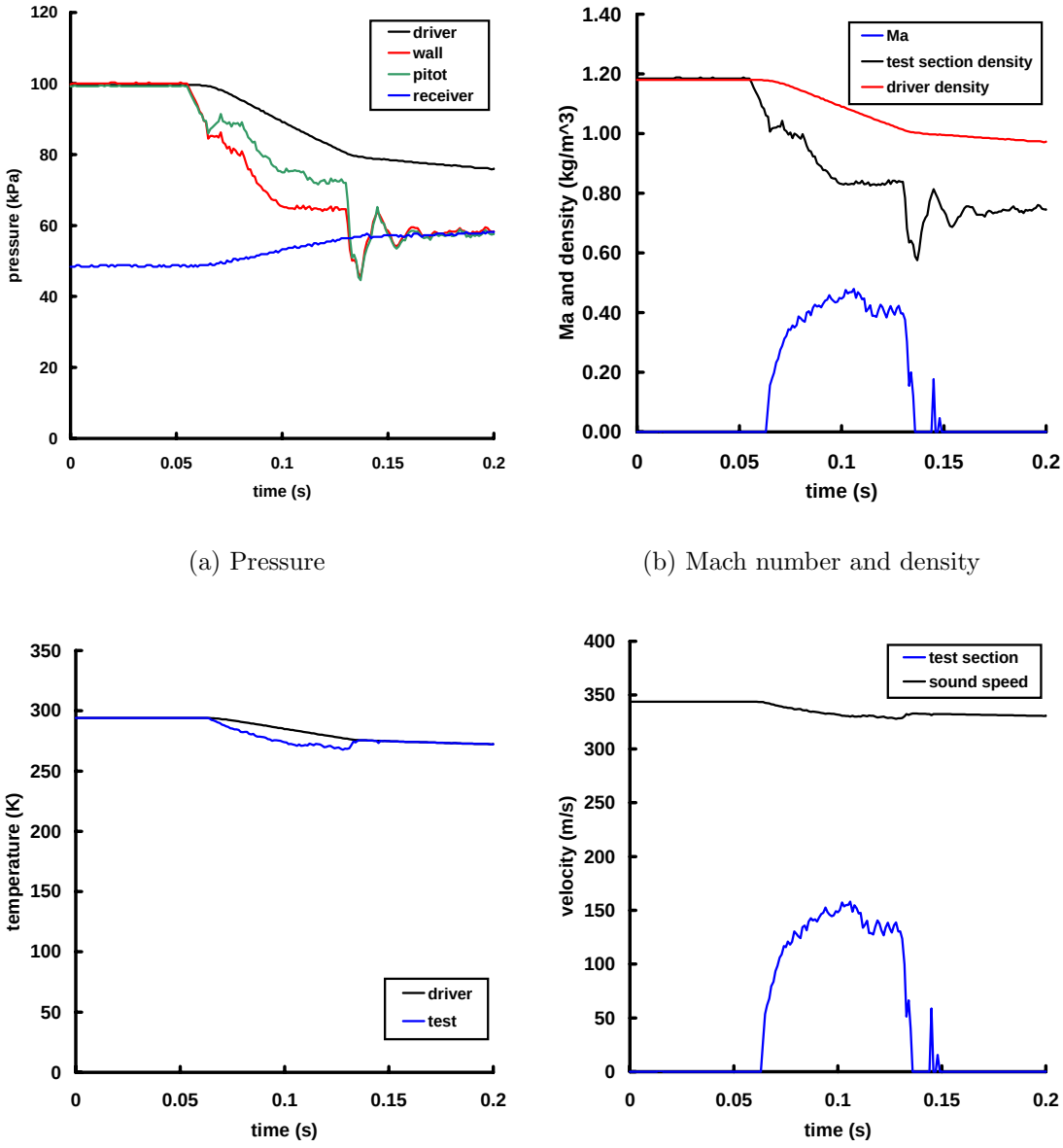

(a) Pressure

(b) Mach number and density

(c) Temperature

(d) Test section velocity

Figure 80: Shot 026.

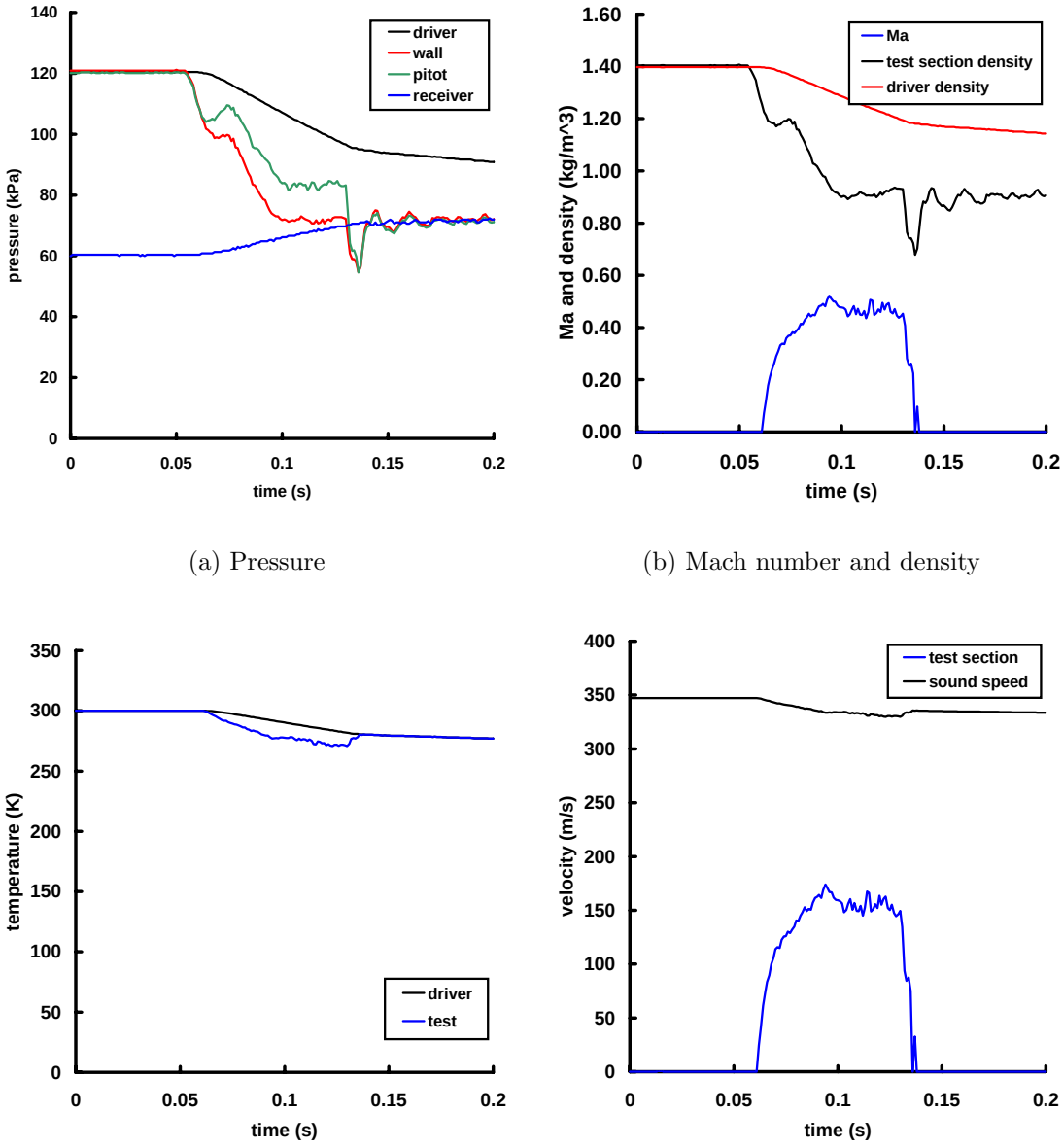

(a) Pressure

(b) Mach number and density

(c) Temperature

(d) Test section velocity

Figure 81: Shot 027.

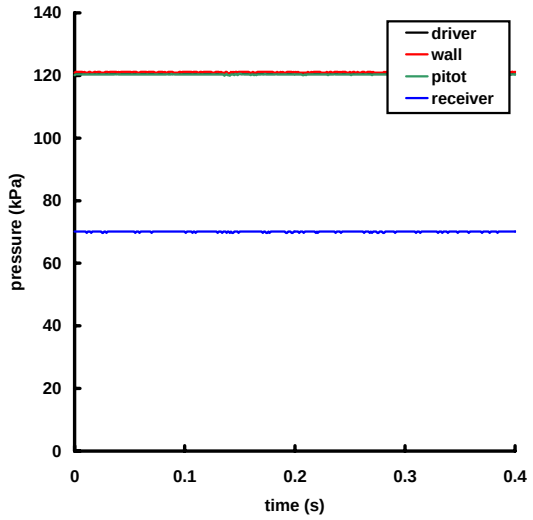

(a) Pressure

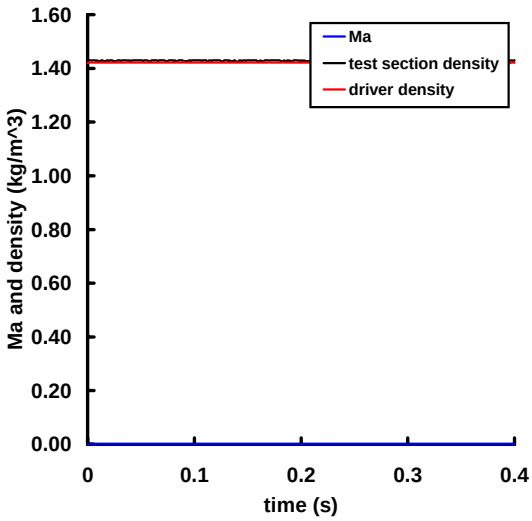

(b) Mach number and density

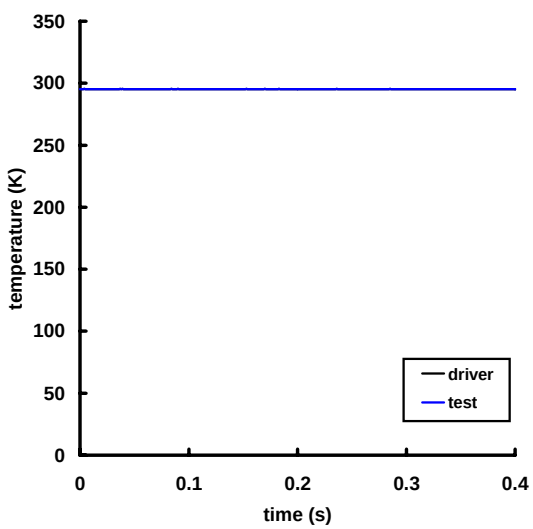

(c) Temperature

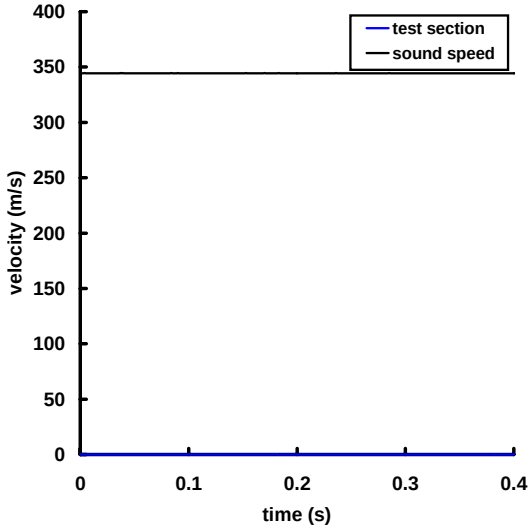

(d) Test section velocity

Figure 82: Shot 028.

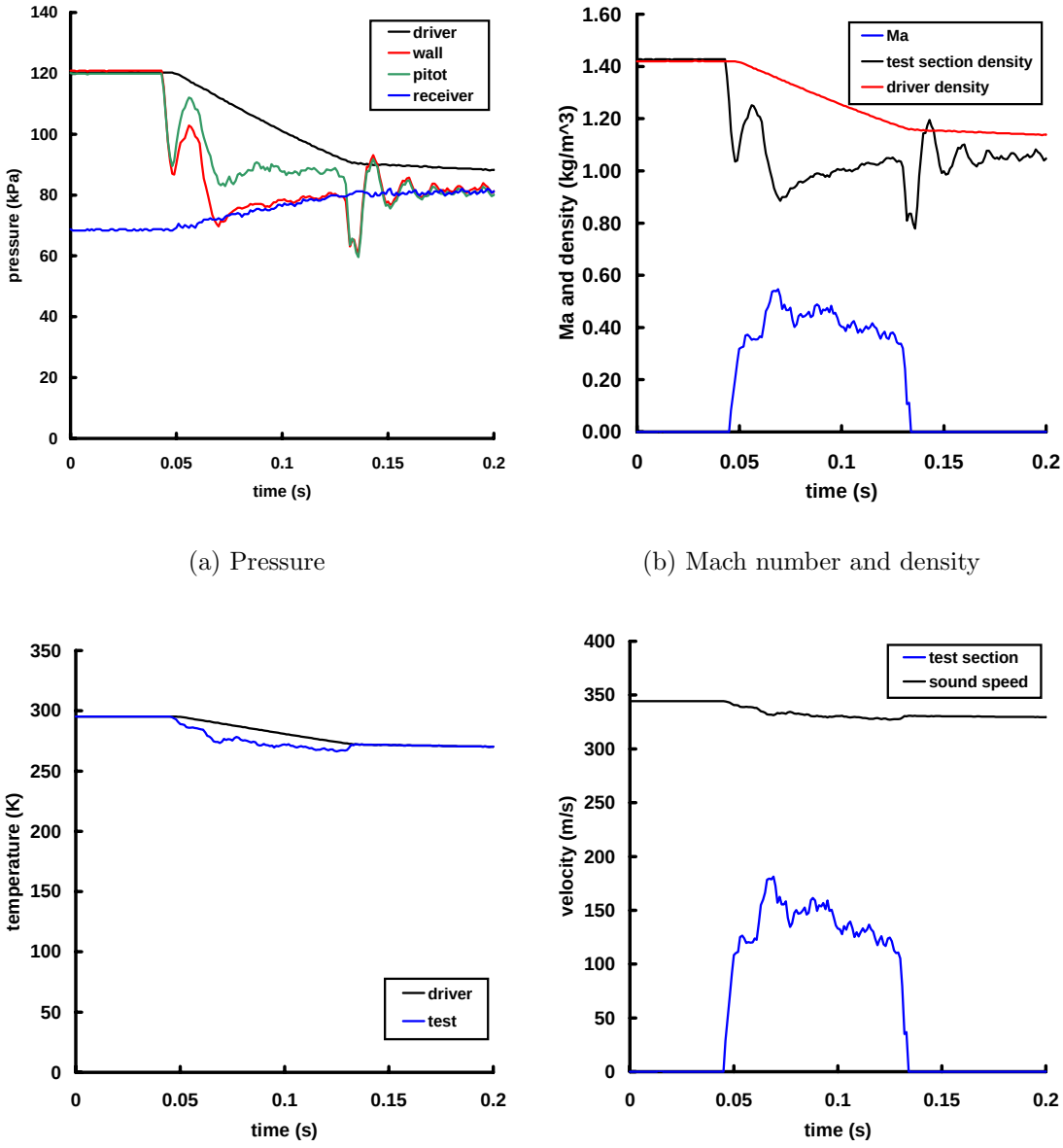

(a) Pressure

(b) Mach number and density

(c) Temperature

(d) Test section velocity

Figure 83: Shot 029.

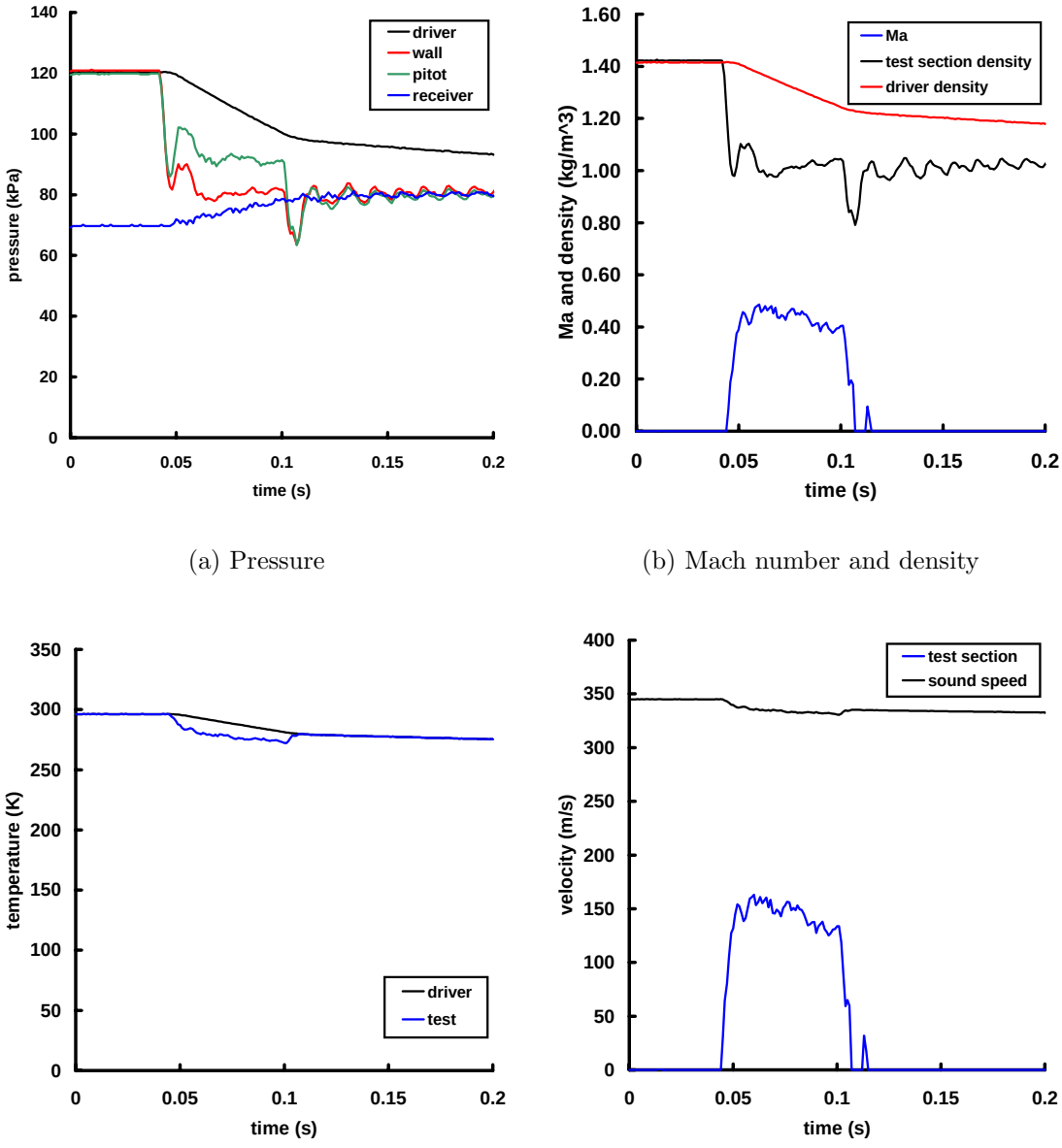

(a) Pressure

(b) Mach number and density

(c) Temperature

(d) Test section velocity

Figure 84: Shot 030.

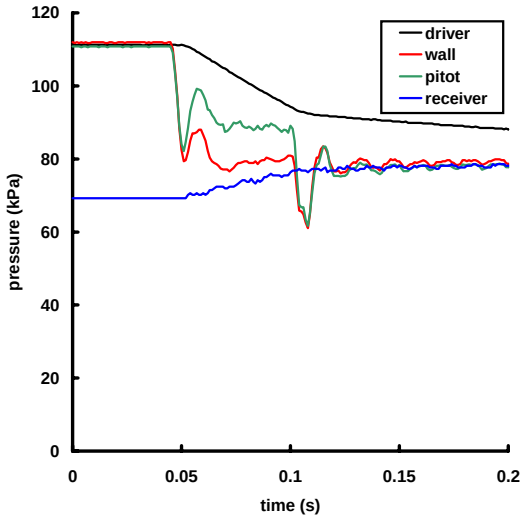

(a) Pressure

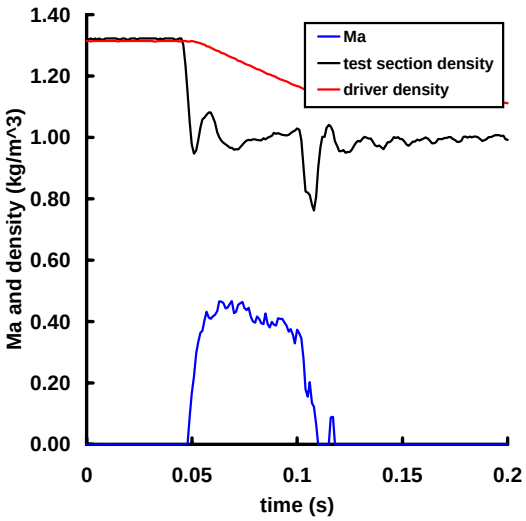

(b) Mach number and density

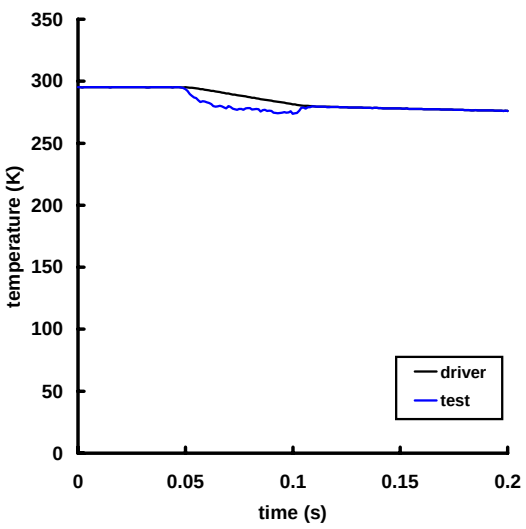

(c) Temperature

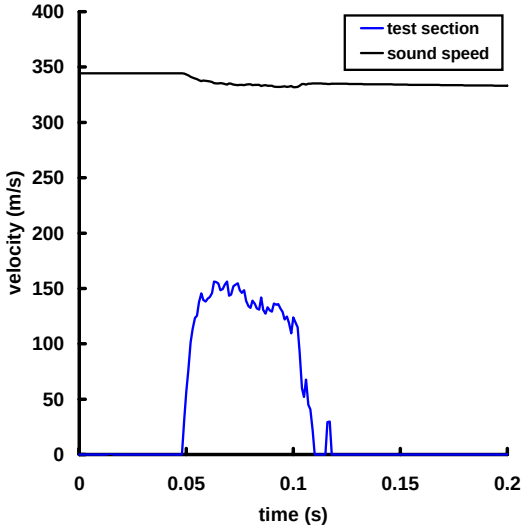

(d) Test section velocity

Figure 85: Shot 031.

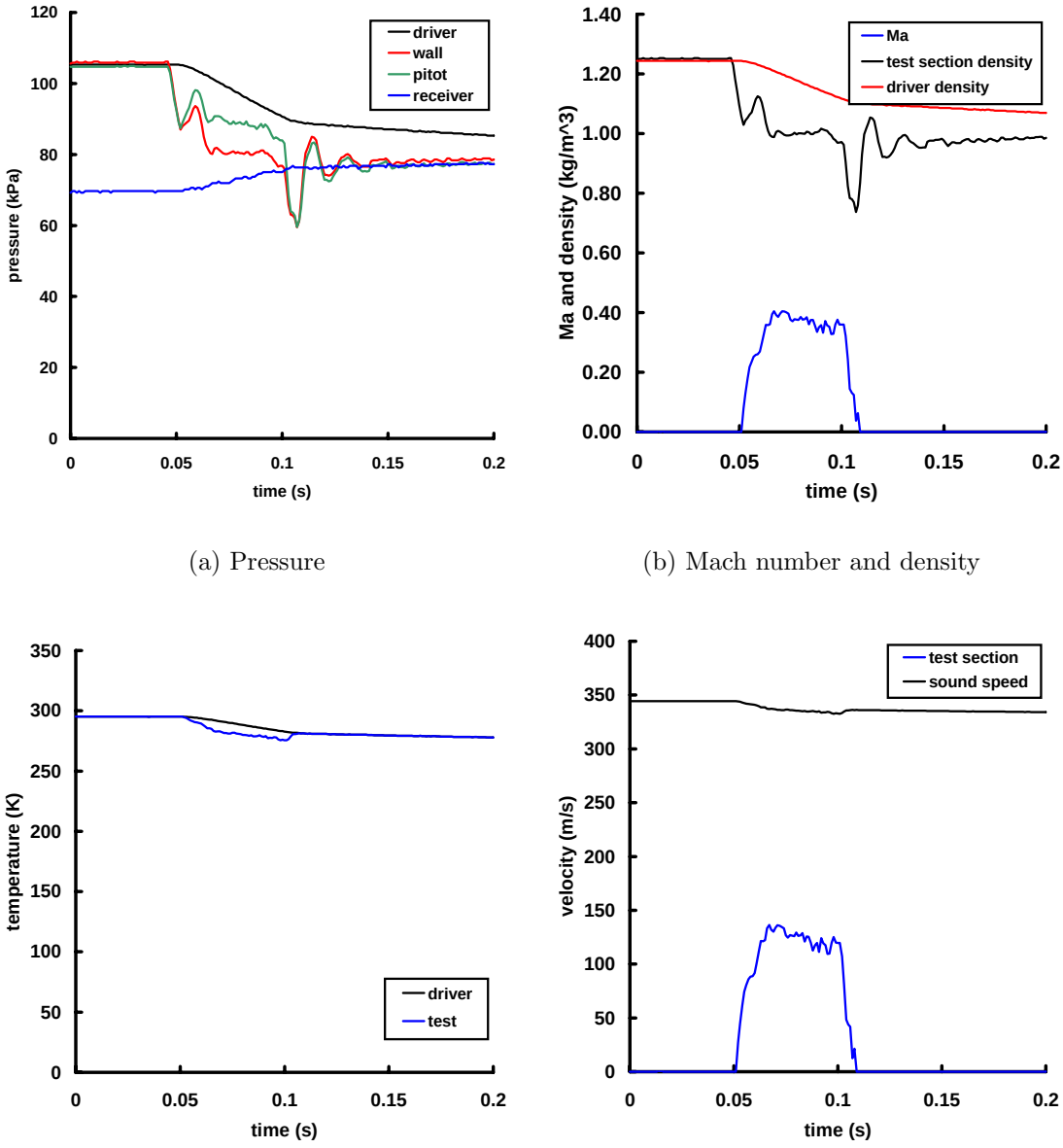

(a) Pressure

(b) Mach number and density

(c) Temperature

(d) Test section velocity

Figure 86: Shot 032.

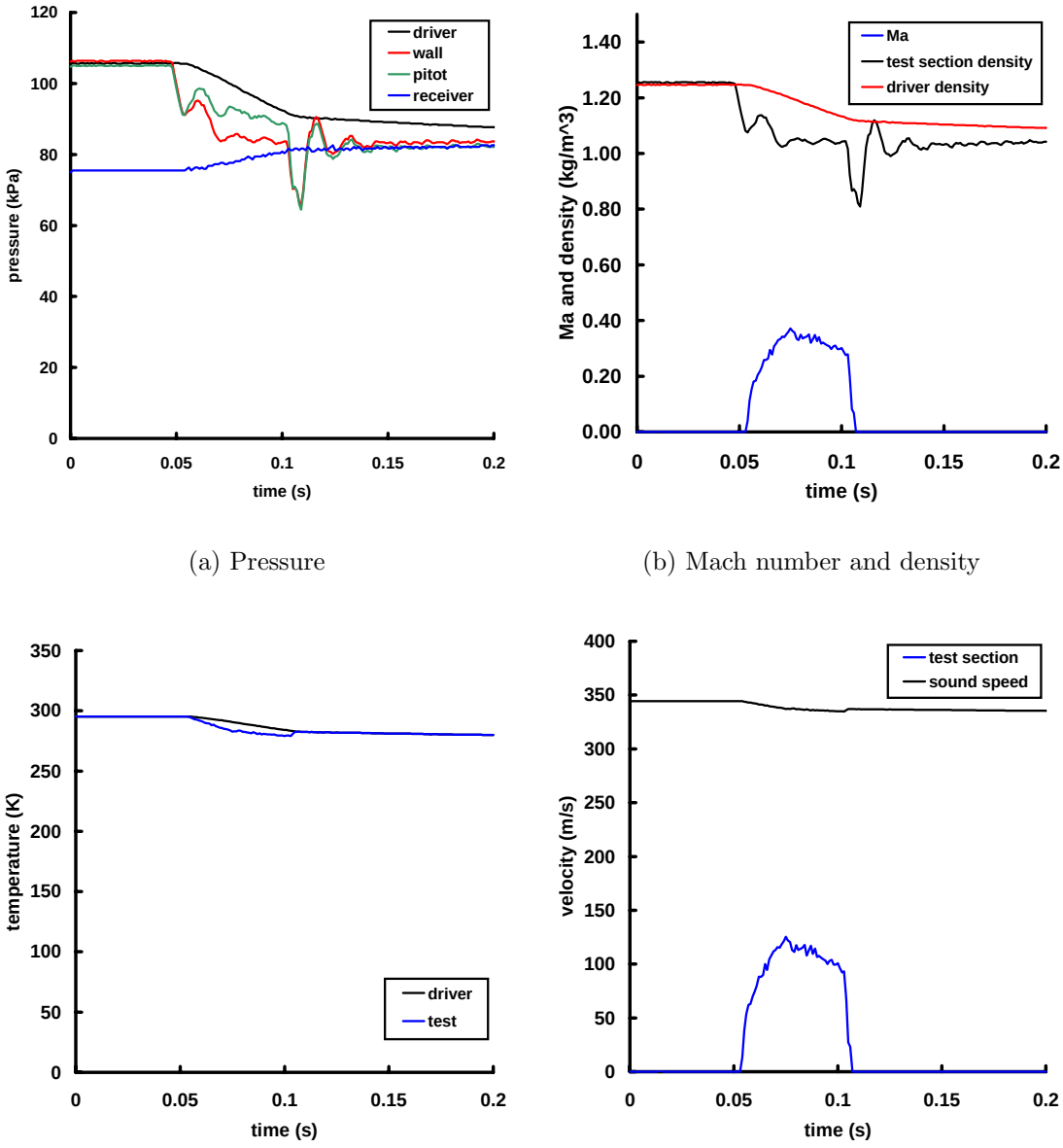

(a) Pressure

(b) Mach number and density

(c) Temperature

(d) Test section velocity

Figure 87: Shot 033.

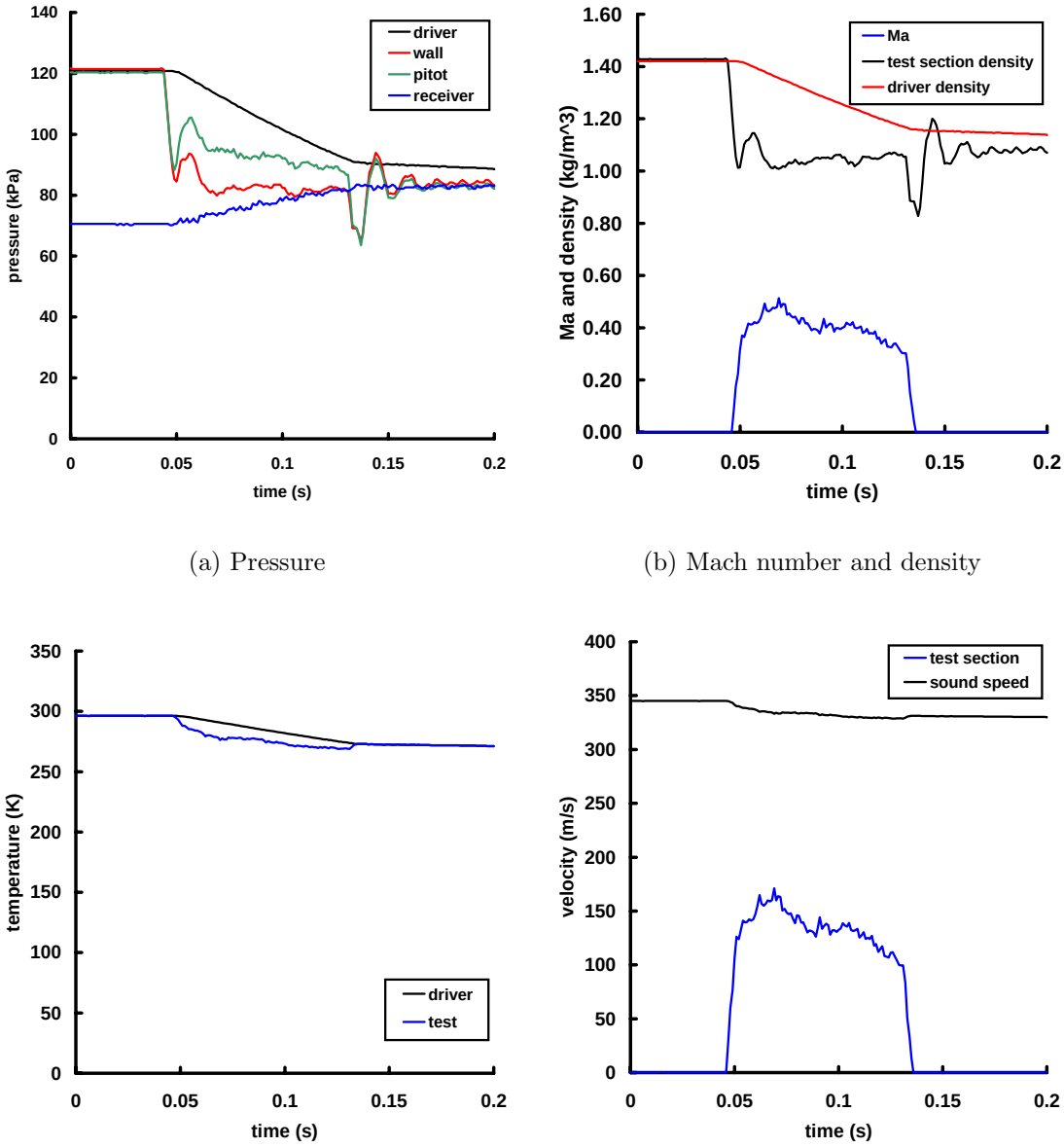

(a) Pressure

(b) Mach number and density

(c) Temperature

(d) Test section velocity

Figure 88: Shot 034.

F AMRITA simulations

Simulations of the scaled valve body start-up:

Simulation number	Pressure ratio	Diaphragm location	Filename
1	10	downstream	pr10xd320.mpg
2	10	upstream (no boat tail)	abrupt_pr10xd300.mpg
3	5	upstream	pr5xd320.mpg
4	10	upstream	pr10xd100.mpg
5	5	upstream	pr5xd150_lmax0.mpg
6	5	upstream	pr5xd150_lmax1.mpg

Simulations of reservoir, valve body and test section:

Simulation number	Pressure ratio	Diaphragm location	Filename
7	10	downstream	shock_tube.mpg.mpg

Simulations to examine design issues:

Simulation number	Pressure ratio	Diapgragm location	Filename
8	5	downstream (shock tube)	pr5xd320lmax1walls.mpg
9	3	downstream (blowdown)	pr3xd320resevoir.mpg
10	3	upstream (blowdown)	pr3xd150resevoir.mpg
11	3	upstream (blowdown)	pr3xd150lmax1resevoir.mpg